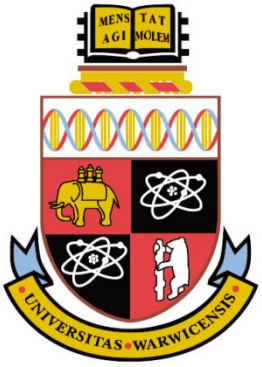

High Resolution Electrochemical Imaging for Energy Conversion and Storage Applications

by

Barak D. B. Aaronson

Thesis

Submitted to the University of Warwick for the degree of

Doctor of Philosophy

Department of Chemistry

September 2015

To Elena, Rita, Emily and Martin

Contents

List of Figures

List of Tables

Abbreviations

AC	Alternating current
AFM	Atomic force microscopy
DAQ	Data acquisition
DC	Direct current
DSSC	Dye sensitized solar cell
ESI-MS	Electrospray ionization-mass spectrometry
ET	Electron transfer
FE-SEM	Field emission-scanning electron microscope
FPGA	Field-programmable gate array
HOPG	Highly oriented pyrolytic graphite
ITIES	Interface between two immiscible electrolyte solutions
MS	Mass spectrometry
P3HT	Poly(3-hexylthiophene)
PET	Polyethylene terephthalate
PTFE	Polytetrafluoroethylene
QRCEs	Quasi-reference /counter electrodes
SECCM	Scanning electrochemical cell microscopy
SECM	Scanning electrochemical microscopy
SICM	Scanning ion conductance microscopy
SMCM	Scanning micropipette contact method
SPM	Scanning probe microscopy
SWNTs	Single-walled carbon nanotubes
WE	Working electrode

List of symbols

E	Potential
$E^{0'}$	Formal potential
F	Faraday constant
i	Current
i_{ac}	Alternating component of barrel current in SECCM
i_{dc}	Direct barrel current in SECCM
i_{Surf}	Surface current in SECCM
j	Current density
j^0	Current exchange density
R	Resistance
V_1	Potential in SECCM used for altering the surface potential
V_2	Bias potential between QRCEs in SECCM
V_{Surf}	Surface potential in SECCM
η	Overpotential
λ	Wavelength

Acknowledgements

First and foremost I would like to thank Elena Piffero for supporting me throughout this long process and reminding me what the important things in life are. Research is a lot about traveling the unknown roads which may not always lead to the initial location sought. Thank you for walking with me all the way here. Thank you for always cherishing how we shape our future together and for loving me and the children unconditionally. Finally, I owe my gratitude to my parents and brothers who have always been there.

As for the scientific journey, I would like to thank Prof. Patrick Unwin for giving me the opportunity to work on an exciting research project at an exciting time of development and allowing me to get it all wrong before showing me the way up again. Your guidance through the adventures of research was immensely constructive. Always encouraging and sharing your enthusiasm towards electrochemistry (as well as towards running and music), you are a true source of inspiration. I would also like to thank Prof. Julie Macpherson for the continuous encouragement and support throughout my Master's and PhD projects. Your love for sharing knowledge, teaching and asking questions are those that brought me to the group in the first place and kept resonating ever since. Finally, I would like to thank you both for always recruiting excellent and friendly postdocs!

As mentioned above, I have had the privilege of learning from talented postdoctoral researchers throughout my PhD and I would like to thank them for their time and efforts and above all for their patience. I would like to thank in particular

those who worked close with me at various stages of my PhD. First, Dr. Stanley Lai who: introduced me to the world of electrocatalysis, taught me all I know about platinum, went through the hurdles of writing my first paper and perhaps has led me to taking my first independent research decisions. Stanley has also introduced me to Stroopwafels and taught me how to correctly pronounce 'Gaoda' cheese and 'Grolsch' beer. Secondly, I would like to thank Dr. Joshua Byers who mentored me during the second half of the adventure (and subsequently might have suffered the most). Josh has taught me a great deal about conjugated polymers, organic solar cells and trained me not to jump into conclusions but yet dare to speculate and challenge classical approaches. Thank you for: trying to learn LabVIEW together, the Costcutter runs, satsuma bets and sharing thoughts about parenthood and life in academia.

Extended gratitude goes to the pioneers in the electrochemistry and interfaces group working on SECCM, who taught me a great deal about the technique: Dr. Neil Ebejer, Dr. Michael Snowden, Dr. Aleix Güell, and Dr. Kim McKelvey. Their hands-on approach, general insight, teaching and discussions have transformed my training in SECCM to much more than an imaging technique.

Much of my understanding of electrochemistry and adoption of good research practices have stemmed from discussions in the office and from observations in the labs. For this I would like to extend my gratitude: Dr. Massimo Peruffo, Dr. Laura Hutton, Dr. Eleni Bizou, Dr. Maxim Joseph, Dr. Robert Lazenby, Dr. Yangrae Kim, Dr. Dmitry Momotenko, Dr. Glen O'Neil (also for discussions on home-brewing) and Mr. Anatolii Cuharuc. Special thanks go to Ms. Changhui Chen,

and Mr. Binoy Paulose Nadappuram, close companions in learning during the years of postgraduate research. I would like to thank all current and past group members for sharing their science and friendship.

To the people behind the scenes, a great deal of gratitude is owed. To the expert design of custom electronics by Dr. Alex Colburn, without which, none of the sensitive current measurements could have been realized. Appreciation goes also to Mr. Lee Butcher and Mr. Marcus Grant for providing mechanical parts for the experimental setups. A special thank you goes to Mr. Rod Wesson in the electronics workshop for the coupling of LED illumination to the SECCM setup and always being enthusiastic about my projects and ideas.

In Chapter 4 I'd like to thank Dr. Maxim Joseph for lasering and sample preparation. In chapters 5 and 6, I'd like to thank Ms. Sophie Kinnear for LabVIEW modifications to the scanning programs, Dr. Helena Stec from Prof. Ross Hatton's research group at the University of Warwick for providing the transparent Au electrodes, and Dr. Michael Staniforth and Mr. Jamie D. Young from Prof. Vas Stavros' research group for help in light intensity measurements. I'd like to thank Jesús Garoz-Ruiz for sharing his knowledge on Raman spectroscopy in Chapter 6.

This PhD project was supported by the European Research Council through Advanced Investigator Grant ERC-2009-AdG 247143; "QUANTIF".

Declaration

This thesis is submitted to the University of Warwick in support of my application for the degree of Doctor of Philosophy. It has been composed by myself and has not been submitted in any previous application for any degree.

The work presented (including data generated and data analysis) was carried out by the author except in the cases outlined below:

1. Platinum single crystal measurements of $Fe^{2+/3+}$ in sulfate and perchlorate media in Chapter 3 (Figures 3.6 and 3.8) were performed by Li Hongjiao in Prof. Marc Koper's group in Leiden, Netherlands. Analysis was performed by the author.
2. Raman spectra analysis (data filtering) in Chapter 6 (Figure 6.6) was performed by Jesús Garoz-Ruiz in Alvaro Colina's group in Burgos, Spain. Spectra were recorded by the author and J. Garoz-Ruiz.

Parts of this thesis have been published as detailed below:

Chapters 1 and 2:

Aaronson, B. D. B.; Güell, A. G.; McKelvey, K.; Momotenko, D.; Unwin, P. R., Scanning Electrochemical Cell Microscopy: Mapping, Measuring, and Modifying Surfaces and Interfaces at the Nanoscale. In *Nanoelectrochemistry*, Mirkin, M. V.; Amemiya, S., Eds. *CRC Press*: **2015**; pp 655-694.

In the work for this chapter I have been a leading contributor.

Chapter 3:

Aaronson, B. D. B.; Chen, C.-H.; Li, H.; Koper, M. T. M.; Lai, S. C. S.; Unwin, P. R. Pseudo-Single-Crystal Electrochemistry on Polycrystalline Electrodes: Visualizing Activity at Grains and Grain Boundaries on Platinum for the Fe^{2+}/Fe^{3+} Redox Reaction *J. Am. Chem. Soc.* **2013**, *135*, 3873-3880.

In the work for this chapter I have equally contributed to both the experimental acquisition and data analysis. Namely, SECCM experiments, EBSD acquisition and data analysis. Part of this work has also been submitted as part of Ms. Chen, Chang-Hui's thesis for the doctoral degree in Chemistry, University of Warwick, 2015.

Chapter 4:

Aaronson, B. D. B.; Lai, S. C. S.; Unwin, P. R. Spatially Resolved Electrochemistry in Ionic Liquids: Surface Structure Effects on Triiodide Reduction at Platinum Electrodes *Langmuir* **2014**, *30*, 1915-1919.

Chapter 5:

Aaronson, B. D. B.; Byers, J. C.; Colburn, A. W.; McKelvey, K.; Unwin, P. R., Scanning Electrochemical Cell Microscopy Platform for Ultrasensitive Photoelectrochemical Imaging *Anal. Chem.* **2015,** *87*, 4129–4133.

Chapter 6:

Aaronson, B. D. B.; Garoz-Ruiz, J.; Byers, J. C.; Colina, A.; Unwin, P. R., Electrodeposition and Screening of Photoelectrochemical Activity in Conjugated Polymers Using Scanning Electrochemical Cell Microscopy *Langmuir*, **2015**, *31* (46), 12814–12822

In the work for this chapter I have equally contributed to the experimental acquisition and data analysis. Namely, SECCM experiments, AFM imaging and analysis, and Raman spectra acquisition.

Abstract

The work presented herein involves the development of the scanning electrochemical cell microscopy (SECCM) platform for visualizing electrochemical and (photo)electrochemical activity of processes at electrode surfaces relevant to energy applications. The use of complementary microscopy characterization techniques such as: field emission-scanning electron microscopy (FE-SEM), electron backscatter diffraction (EBSD), atomic force microscopy (AFM) and Raman microscopy provides a correlation between the localized (photo)electrochemical activity (obtained by SECCM) and physical properties of the investigated surfaces. SECCM studies of a polycrystalline platinum surface highlight the significant variations in electrochemical activity that can be measured at electrode surfaces due to variations in localized crystallographic orientation and the presence of grain boundaries. An ostensibly simple redox couple ($Fe^{2+/3+}$) in two different acidic media on a polycrystalline platinum foil is utilized as a model system and the localized crystallographic orientation of the surface is determined by EBSD analysis. The approach is then extended to room temperature ionic liquids (RTILs) to study the reduction of triiodide (I_3^-) to iodide (I^-) on polycrystalline platinum for the application of dye sensitized solar cells (DSSCs) as a counter electrode. The coupling of illumination with high sensitivity current followers and external lock-in amplifiers to the SECCM setup is described and the resulting platform is demonstrated to allow investigation of (photo)electrochemical systems. Two examples are provided: imaging photo-anodes in DSSCs and electrodeposition and characterization of conjugated polymers on a transparent electrode for organic photovoltaic devices. Finally, photo-SECCM is used for determining structure-activity relationships for (photo)electrocatalysts of conjugated organic polymers by coupling the technique with AFM and Raman spectroscopy, suggesting the technique as a potential high throughput screening platform. The approach is exemplified by investigating poly(3-hexylthiophene) and provides not only a correlation of film morphology and photo-activity but also extracts important information on film growth and aging.

Chapter 1 Introduction

Abstract

This thesis is concerned with the application of scanning probe microscopy (SPM), and in particular, scanning electrochemical cell microscopy (SECCM) to the field of (photo)electrocatalysis for energy conversion and storage. In this chapter, discussion is limited to electrochemical SPMs and a review of the topic is given followed by a comprehensive description of the SECCM setup and working principles. In the subsequent chapters, materials and systems with interest to energy and storage applications are investigated and are thus introduced later in the thesis. The following introductory sections are adapted from a book chapter in: *Nanoelectrochemistry*, CRC Press: 2015; pp 655-694.

1.1 Scanning probe microscopy and scanning droplet probes

The acquisition of spatially resolved functional and structural information on surfaces and interfaces is a major theme in contemporary microscopy, with applications spanning materials science and technology, biology, medicine and nanotechnology generally. However, access to local chemical information (especially concerning dynamics at condensed phase interfaces) from mainstream microscopy techniques is often challenging, and structure/function relationships remain obscured. To expand the capabilities of microscopy, significant efforts have been invested in the development of SPM techniques[1] that facilitate direct measurements of various types of processes at a wide range of interfaces. The purpose of this introduction chapter is to highlight scanning droplet-based

techniques, with a particular focus on SECCM.[2] This is a recently developed methodology within the family of more established SPMs, but one which has already demonstrated considerable versatility for probing and visualizing interfacial reactivity, opening up new opportunities for understanding electrochemical processes, and as a tool for the modification and patterning of surfaces.

When considering electrochemical imaging,[3-5] the most prominent technique is scanning electrochemical microscopy (SECM),[6-9] which has been used to investigate (electro)chemical properties and reactions at a variety of interfaces. The translation of SECM into diverse fields (biology,[10-13] energy research[14,15] and materials science[16,17]) has been facilitated by the development of different operation modes, the wide range of tips (probes) that can be utilized and a well-established theory and models for quantitative and qualitative data analysis.[3,18-21] However, there are some limitations of SECM experiments, particularly the fact that the tip electrode response (and spatial resolution) depend in quite a complex way on the probe-to-substrate separation and reactivity. This arises because the SECM probe is a remote sensor of reactivity, detecting products or intermediates of the surface process or competing with the surface for a particular reagent. The tip-substrate distance thus needs to be known precisely and, particularly for nanoscale measurements, there is a need for additional instrumentation for reliable tip positioning. Although various positioning control mechanisms have been explored, including the detection of shear forces,[22-25] coupling SECM with scanning ion conductance microscopy (SICM),[26-30] impedance measurements,[31,32] the combination of SECM with atomic force microscopy (AFM),[33-36] the use of tip position modulation[37-39] and intermittent contact techniques,[40-42] none of these methods has emerged as definitive, and while each has its merits, there are also some issues related to tip design and reliability.[3] Another

important consideration for the functional characterization of interfaces with SECM arises from the requirement to immerse the entire sample into electrolyte solution and typically maintain a reaction at the tip and substrate throughout the duration of an image, which may require a period of upwards of an hour, with implications for the stability of the tip and sample, especially from fouling or contamination. This problem can be circumvented to some extent through the use of multi-electrode SECM probes for parallel imaging,[43-48] which speed up the process and allow access to wider areas of a sample.

SECCM[2,49] overcomes some of the aforementioned issues and allows the direct measurement of charge transfer and other processes at a variety of electrodes, and interfaces generally, in many cases at the nanoscale. The intrinsic principle of scanning droplet cell methods is the confinement of electrochemical measurements in a small area of the surface allowing direct, localized spatially resolved surface investigations of (semi)conductive electrode substrates (and, for SECCM, insulating surfaces where there are ion fluxes). A small mobile droplet is typically created as a liquid meniscus between a (scanned) probe and the specimen surface, which serves as a working electrode. The working electrode size is defined by the wetted area of the surface, while integrated counter-reference electrodes inside the probe, filled with electrolyte, result in a dynamic electrochemistry cell setup. In practice, this experimental arrangement is particularly advantageous because of the possibility of examining only small areas of the substrate. It is especially beneficial for the investigation of delicate samples, the characterization of dry surfaces, and the avoidance of complexity in sample preparation (encapsulation). Furthermore, only small amounts of electrolyte solution are needed. This approach yields relatively low

background signals on the working electrode, enabling direct and sensitive measurements.

The conventional setup for a scanning droplet cell microscope typically utilizes a pipette or a capillary with a small opening (usually with a tip diameter of the order of 1 μm to 1000 μm), mounted on a microscope stage for positioning of the probe over the sample.[50-56] In most cases, the capillary has a small silicon or rubber seal at the tip to prevent solvent evaporation and to provide a working electrode area of well-defined dimensions (Figure 1.1a and 1.1b). The implementation of this type of scanning droplet cell design has been demonstrated with single point (static) measurements as well as in a scanning mode for corrosion research, e.g. in local pit initiation on stainless steel,[50] local surface modification through direct lithographic writing of surface oxides[51] and for the characterization of individual grains and grain boundaries on alloys.[52-54,56] Staemmler et al.[55] attempted to bring the capabilities of this technique to the nanoscale through the electrochemical surface modification of gold and silicon substrates. Nanolithographic patterning with an electrochemical scanning capillary microscope was demonstrated through the elecrodeposition of thin copper lines and dots using a pipette with a 150 nm opening and shear-force positional feedback control.[55]

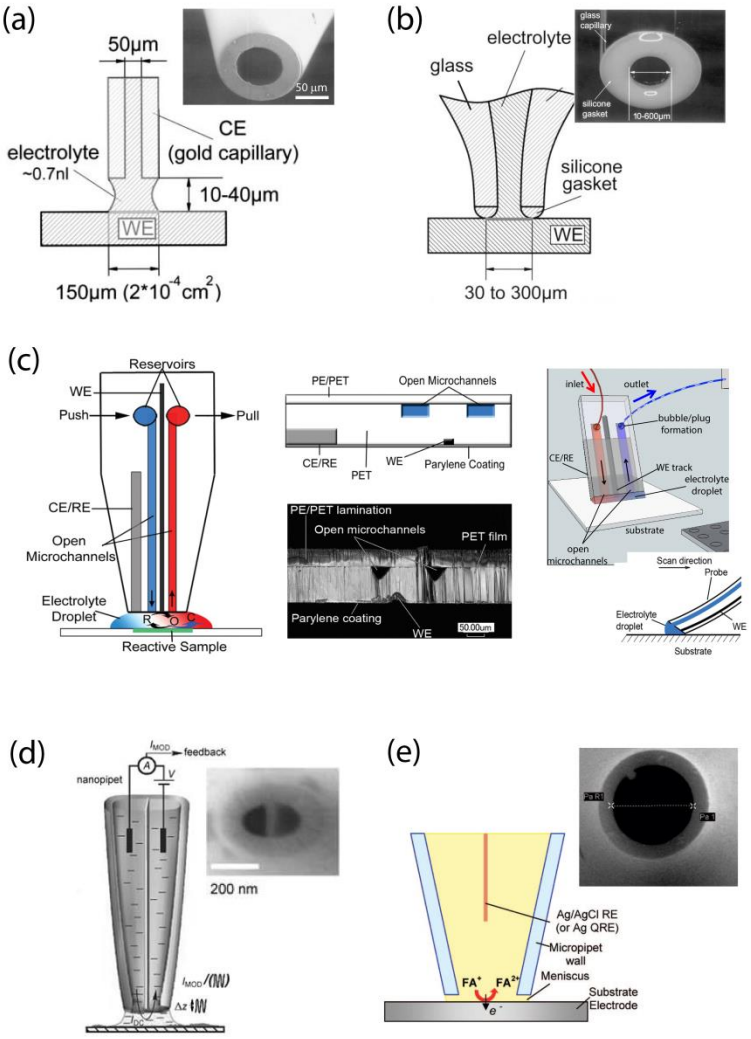

Figure 1.1 Examples of droplet confinement. (a) Micron-sized openings at glass pipettes employed to confine measurements at a working electrode (WE) to the microscale (adapted from ref 57), (b) incorporating a gasket to avoid evaporation and delimit an area of interrogation (adapted from ref 52). (c) Flexible multi-channel push-pull probes, with integrated electrodes and connected to microfluidic systems, as applied to non-conductive surfaces (adapted from ref 58 and ref 59). (d) Confined measurements at the sub-micron level, employing double barrel (adapted from ref 60) and (e) single barrel glass pipettes (adapted from ref 61).

A flow-through cell design has also been introduced to the scanning droplet cell concept, where a constant electrolyte flow passes over the wetted surface area.[62] This approach has been used for photoelectrochemical analysis of semiconductors and solar cell materials,[63] but the versatility of such a strategy is the possibility of complementing to electrochemical microscopy and point measurements through integration with other techniques for the downstream analysis of products of (electro)chemical reactions. Electrochemical studies of the anodic dissolution of Zn alloys,[64-66] as well as Cu[65,67] and Fe,[68] were combined with spectroscopic and mass-spectrometric (MS) techniques for on-line detection, demonstrating the efficacy of this approach for integrated chemical-electrochemical surface analysis.

Push-pull[58] and fountain pen[69] soft SECM probes have also been introduced for the analysis of dry surfaces (Figure 1.1c). These microfluidic SECM probes were developed following the concept of soft probes for topography-tolerant and high-throughput SECM investigations of samples with extended surface area.[44-47,69] Probes fabricated from soft polymeric materials (e.g. polyethylene terephtalate, PET) have allowed SECM experiments in contact mode, providing close to constant probe-to-substrate separation, without the need for additional positional feedback and also providing a versatile platform for integration with microfluidic systems. Coupling the resolving power of SECM with highly sensitive MS techniques within microfluidic push-pull probes has opened up the possibility of simultaneous electrochemical imaging and MS analysis, as illustrated by studies of latent fingerprint samples and on-line (electron spray ionization-mass spectrometry) ESI-MS and SECM characterization of immobilized enzyme reactivity.[59]

Although the techniques described above are capable of local electrochemical measurements, they typically operate at a scale of tens of microns or larger. The ability to readily pull glass or quartz pipettes with tip diameters in the range of several nanometers to hundreds of nanometers has led to a breakthrough in electrochemical imaging resolution, coupled with extremely simple, fast and cheap probe preparation protocols that have high success rates. SICM, which was introduced in late 1980s, has been proven to be a powerful high-resolution non-contact pipette-based technique for the visualization of substrate topography.[70] The positioning of a mobile nanopipette is achieved through the detection of ion currents arising from the migration of ionic species between two biased quasi-reference /counter electrodes (QRCEs) – one located within a sharp pipette filled with electrolyte solution and another one in the bulk of a bathing solution. The feedback mechanism relies on the moderation of the ion flow between the QRCEs (governed by a distance-dependent resistance of the electrolyte solution around the tip opening)[71] when the nanopipette is brought into the vicinity of a substrate surface. The vertical position of the probe can be controlled using either the direct (ion conductance) current (DC) magnitude or the amplitude of the alternating current (AC) component of a modulated ion current generated by a physical oscillation of the probe around its vertical (z) position.[72,73] The latter provides a more sensitive and stable mechanism for the control of tip-substrate separation distance as the ion current can be detected using phase-sensitive techniques and the AC ion current is also less susceptible to bulk changes in the solution conductivity. The evident advantages and capabilities of the SICM technique have been successfully demonstrated in nanobioscience for the imaging of living cells,[74-77] cell membrane structure down to the protein level,[78] studies of ion fluxes across biological and

artificial membranes,[28,79,80] the patch-clamp technique in electrophysiology[75,79] and the modification of surfaces with biomaterials using a dual channel pipette (Figure 1.1d).[60,81-83] At the same time, as highlighted above, SICM has recently been used in combination with other methods, such as SECM, as an independent method for maintaining constant probe-to-substrate distance.[26-30]

It has also been shown recently that pulled nanopipettes can also be employed as multipurpose tools for concurrent topographical and electrochemical reactivity imaging in a novel electron transfer/ion transfer mode of SECM.[84] The tip of a silanized nanopipette was filled with an organic electrolyte solution (immiscible with the external aqueous solution) to make a nanoscale liquid/liquid interface. Controlling the bias across this boundary allowed ion transfer to be driven, enabling tracking of the substrate topography, similar to SICM, as well as the localized reactivity, similar to SECM, depending on the nanopipette bias. For example, with a positively polarized nanopipette, the transfer of PF_6^- anions from aqueous solution into the nanopipette was used to track the probe-to-substrate distance. The organic phase within the nanopipette could also contain a neutral redox probe (for instance, a ferrocene derivative) that would diffuse away from the nanopipette opening regardless of the bias and could undergo electrochemical transformation into its ionic form (ferrocenium derivative) at reactive sites on the specimen surface. The ion transfer current into a negatively biased pipette was then used to record local reactive properties of the surface. This sequential sensing of topography and reactivity with a single probe (pipette orifice) is a good example of the exploitation of the mass transport properties of an interface between two immiscible electrolyte solutions (ITIES) supported at the tip of a nanopipette.[85,86]

In order to bring the high-resolution capacity of pulled pipettes into scanning droplet cell methodology for the analysis of dry substrates, a scanning micropipette contact method (SMCM) was recently developed (Figure 1.1e).[61] The probe was a single barrel pipette with dimensions down to a few hundred nanometers, filled with electrolyte solution containing redox-active species and a QRCE. SMCM has been successfully demonstrated for the electrochemical interrogation of redox activity at highly oriented pyrolytic graphite (HOPG) and investigations of heterogeneities in the electroactivity of aluminium alloys using point-by-point measurements. Typically the pipette was operated in a hopping mode, whereby the electrode substrate was approached, then paused upon the contact of the meniscus with the substrate (detected as a current flow). The steady-state current value or a current-voltage curve was recorded before the pipette was retracted back from the substrate for further repositioning over different locations at the substrate. The implementation of the hopping mode enabled images of reactivity to be built up across the substrate of interest. Furthermore, the simplified probe design avoided the need for a rubber gasket/seal at the pipette tip, yet allowed precise control of the contact meniscus and the area of the working electrode with high reproducibility. Similar techniques, but with pipettes that are tens of microns in size, have been implemented for voltammetric studies at single-walled carbon nanotubes (SWNTs) and metal nanowires[87] and for the analysis of the parameters controlling the electrodeposition of metal nanoparticles on SWNTs.[88]

1.2 Scanning electrochemical cell microscopy (SECCM)

SECCM represents a new generation of scanning droplet cells, making use of a double-barrel theta-pipette to create a probe (Figure 1.2a) that functions as both a conductivity cell between QRCEs in the two nanochannels of the probe and an amperometric/voltammetric cell with a (semi)conducting working electrode surface with which the meniscus of the nanopipette makes contact. The technique provides exquisite control of a droplet with a surface (controllable on the ms timescale or shorter) and opens up the possibility of controlling and measuring electrochemical fluxes at interfaces, while simultaneously exploring ionic mass-transport between the pipette barrels and measuring substrate topography.[2]

1.2.1 SECCM experimental setup

A labelled diagram of a typical sample scanning instrument used for SECCM is shown in Figure 1.2c and 1.2d. The sample (2 in Figure 1.2c) is mounted in a sample holder (3 in Figure 1.2c) that is frequently made from a thin piece of polytetrafluoroethylene (PTFE) or other lightweight material. The sample holder can also contain a moat, which is filled with electrolyte solution to create a humidity cell. The sample holder is, in turn, mounted on *x*, *y* piezoelectric positioners (5 in Figure 1.2c) for lateral movement of the sample. The SECCM probe (1 in Figure 1.2c) is mounted on a *z* piezoelectric positioner (6 in Figure 1.2c) that allows movement of the pipette towards or away from the sample surface. This positioner is mounted, in turn, on a manual *x*, *y*, *z* stage to enable coarse positioning of the pipette probe (7 in Figure 1.2c). The pipette is held in position, on a tip holder, using a 'v' shaped groove and PTFE screw (4 in Figure 1.2c).

The piezoelectric positioners are controlled through amplifiers/servos (10 in Figure 1.2d). A bipotentiostat (custom built, 12 in Figure 1.2d), is used to measure electrochemical signals at the probe. The probe is oscillated normal to the surface using the oscillating signal that is generated by the lock-in amplifier, and the resulting oscillating current signal is extracted at the same frequency using a lock-in amplifier (11 in Figure 1.2d). A field-programmable gate array (FPGA) card (13 in Figure 1.2d) mounted directly into the motherboard of the personal computer (PC) is used to collect all the data and control the instrument. The use of an FPGA card allows complex calculations, such as data filtering and probe position control logic, to be completed quickly. However, a standard DAQ card can also be used. LabVIEW is used (14 in Figure 1.2d) to control the FPGA card on the PC.

Electrical, acoustic and vibrational isolation are essential for high resolution current measurements and positional control. All instruments are mounted on vibration isolation tables (8 in Figure 1.2d), within a Faraday cage (custom made) with acoustic foam to reduce vibrations (9 in Figure 1.2d). Cameras or an optical microscope (not shown) can be used to aid positioning of the probe.

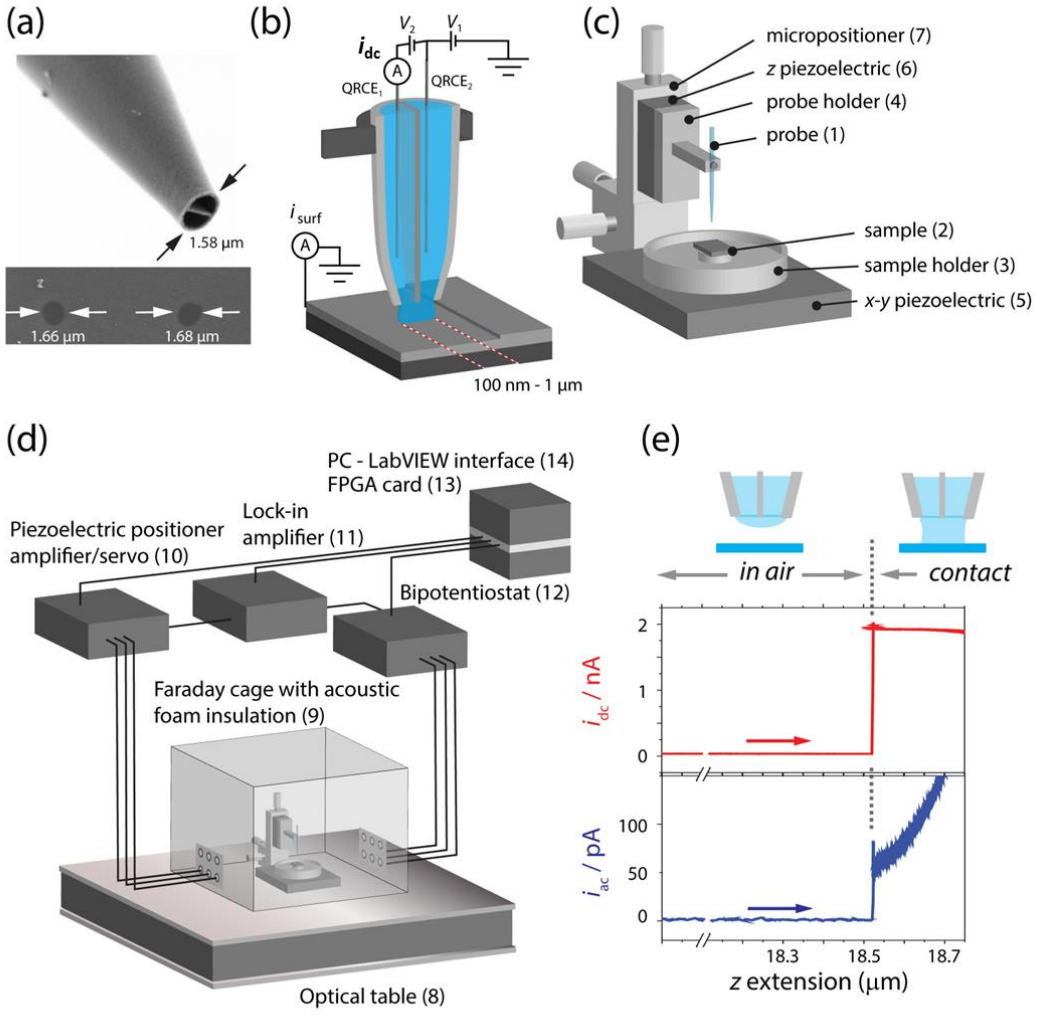

Figure 1.2 Scanning electrochemical cell microscopy (SECCM) (a) SEM image of a typical double barrel probe. Shown below are example footprints resulting from meniscus contact with a substrate (TEM grid), demonstrating a consistency in size that is commensurate with the probe dimensions. Schematics of the setup of a typical SECCM platform: (b) electrochemical cell configuration; (c) probe, positioners and sample holders; (d) overview of full setup. (e) Ion conductance current between the barrels of the pipette (i_{dc}) as a function of tip-substrate position (z piezoelectric positioner extension) showing the i_{dc} and i_{ac} (current) responses.

1.2.2 Working principle of SECCM

The liquid meniscus that forms at the end of a SECCM probe is brought into contact with a sample and localized (electrochemical) measurements are carried out. Importantly, the response only depends on the area of the surface that is in contact with the liquid meniscus.

The localized electrochemical measurements can be the electrochemical current that is measured through the surface,[49] and/or the conductance current (i_{dc}) between the QRCEs of the SECCM probe.[89] The liquid meniscus can also be used to modify the surface, which can be assessed afterwards using complementary techniques such as AFM or FE-SEM.

A feedback response is needed to control the distance between the end of the SECCM probe and the surface (i.e. to control the meniscus thickness), to prevent the pipette from crashing into the surface and to maintain a constant distance between the end of the probe and the surface during imaging. This is achieved by monitoring the ion current between the QRCEs in the barrels of the SECCM probe. As discussed below, the ion current depends on the size and shape of the liquid meniscus.

Practically, as in SICM,[5] a distance-modulated protocol is used to maintain a very stable feedback response. The probe position is modulated perpendicular to the surface, and once the liquid meniscus is in contact with the surface this produces an AC component at the same frequency as the probe oscillation due to the changes in the probe-surface distance. The AC component is extracted using a lock-in amplifier, and the magnitude is used as a feedback signal (see above). Oscillation frequencies between 70 Hz and 400 Hz are typically used, with an oscillation amplitude between 20 nm and 300 nm (usually ca. 10 - 15 % of the meniscus height or, similarly, the

probe diameter). The response of the SECCM probe as it is approached towards a surface illustrates the high precision with which meniscus contact can be controlled and maintained with the surface. Using the data in Figure 1.2e as an example, when the liquid meniscus is in air the ionic current is constant at a stable finite value. This is relatively low, indicating a very thin meniscus at the end of the pipette. The AC component is non-existent, as is shown in Figure 1.2e, because the modulation does not appreciably alter the meniscus dimensions when the probe is in air (or other atmosphere). When the liquid meniscus makes contact with the surface, the meniscus size (and shape) changes and this can easily be observed as a sudden increase in the ionic current (i_{dc}) and also the oscillation current amplitude (i_{ac}). This 'jump to contact' with the surface is a very obvious signal and indicates that the liquid meniscus has made contact with the surface (without contact from the pipette). The contact area of the liquid meniscus is typically the size of the end of the probe (as is shown in Figure 1.2a). However, the chemistry of the surface can have an impact on the contact area, with very hydrophobic surfaces tending to repel aqueous droplets or very hydrophilic surfaces causing leaking of aqueous electrolyte solution over the surface. In general, however, a wide range of surfaces can be investigated with aqueous solutions, as outlined in this contribution, and it may be possible to expand the range of surfaces and solvents by controlling the pressure of the liquid in the pipette.

Once the meniscus is in contact with the surface, the magnitude of the DC and AC depend on the distance between the end of the probe and the surface. As the meniscus is squeezed (the probe is moved closer to the surface), the dimensions of the conductance cell decrease and so the resistance increases (decreasing i_{dc}) as in SICM.[5,49] The AC value (i_{ac}), however, essentially measures the derivative of i_{dc} with

respect to the distance and so this value increases with decreasing distance and is particularly sensitive to the tip-substrate separation as shown in Figure 1.2e.

1.2.3 Point measurements

The SECCM meniscus probe can be brought into contact with the surface of interest at a number of discrete points. Since only a tiny fraction of the surface is in contact with the liquid meniscus at any time, this allows many repeat measurements to be made over a surface, which can provide large data sets for robust statistical analysis. Typically, the SECCM probe is approached towards a surface until the 'jump to contact' signal is observed (see above), at which point the movement of the probe is halted. The probe is then held stationary, with the liquid meniscus in contact with the surface, for a user-defined period of time. The electrochemical current at a (semi)conducting surface or the change in conductance current between the barrels is measured during the period that the probe is held stationary on the surface. Measurements are made as a function of time, and the potential of the surface can be changed in a user-defined manner to provide voltammetric control (by adjustments of V_1 in Figure 1.2b).

1.2.4 Lateral scanning and imaging

Two dimensional maps of the surface of interest can be constructed by moving the SECCM probe meniscus laterally over the surface, following the topography and collecting the spatially resolved response. The probe is first approached towards the surface until the liquid meniscus makes contact with it, as

described above. The probe is then moved laterally across the surface and a feedback loop is used to maintain a user-defined oscillating ion current magnitude, which corresponds to a constant probe-surface distance. Two different methods to maintain a constant set point have been reported, a distance-based method[49,90,91] and a time-based method.[92,93] In the distance-based method, the height of the probe is adjusted based on the lateral distance the probe has moved (i.e. the probe is moved laterally a set distance, the movement is paused, the oscillation amplitude is measured, and the height is adjusted to maintain the set point). In the time-based method, the probe is moved laterally at a constant speed and the height of the probe updated after a set period of time has passed. This allows the probe to be moved constantly, and so reduces the time required to generate a map.

Maps of the surface properties are typically constructed from a series of parallel lines scans, although other scan patterns can be employed.[94,95] In a number of reports, the SECCM probe is moved forward and then back over the same line, before being moved laterally to the start of the next line.[92,96] Data are collected during both the forward and reverse movements and therefore two maps (a forward and a reverse map) of the surface properties can be constructed from every scan. This allows the consistency of the data to be checked (with the electrode surface at the same potential during both scans), or protocols can be used where a different potential is applied during the forward and reverse scans.

During a scan, the ionic current, magnitude (and phase) of the oscillating ionic current, substrate current and the position are recorded. This allows 4 (or 5) maps for each direction (forward and reverse) to be generated. This wealth of information can then be used to identify variations in surface activity and local topography. The ionic current map reveals changes in the conductance between the

QRCEs, and is typically relatively featureless. However, changes in the shape or size of the liquid meniscus can affect the ion current signal, and so this map can be used to determine if the meniscus is stable during the scan. Additionally, if the surface process of interest leads to changes in the ionic composition of the electrolyte (interfacial ion flux processes or electrochemical reactions leading to a change in the ionic strength) this can be observed in this map.[49]

The magnitude of the oscillating ion current is used as a feedback signal and so ideally maps of this signal should be featureless. However, the feedback circuit has a finite response time and therefore maps of this signal can reveal the edges of topographical features (in the same way as the error signal in AFM).[97] The laterally resolved map of the *z* position of the probe reveals the apparent topography of the sample. The maps of the surface current (for (semi)conducting substrates) identify the local surface activity. The analysis and interpretation of the surface current is dependent on the experiment, but using appropriate finite-element modelling (FEM) modelling techniques, the surface current response can be analyzed quantitatively and used to extract surface kinetic information.

1.2.5 Surface modification

SECCM has been typically used to map the local electrochemical response, but can also be used to modify a surface. Active species can be dissolved or suspended in the electrolyte solution and the contact between the liquid meniscus and the surface used to deliver the active species to a specific location on the surface.[93-95,98] The SECCM probe can be used to generate spots on a surface by approaching the probe to discrete points on the surface[93,94] or generate patterns by moving the probe laterally across the surface while using a feedback loop to follow the topography of

the surface and maintain the contact between the liquid meniscus and the surface.[94,95,98] Applications of these methods are discussed herein.

1.3 Aims of thesis

The aims of this thesis are to further develop the SECCM platform for visualizing electrochemical and (photo)electrochemical activity at the submicron to nanoscale in order to gain a deeper understanding of structure-activity relationships in electrode materials used in energy storage and conversion devices. Using a multimicroscopy approach, the SECCM is used to visualize and quantify electrochemical activity at a confined electrochemical cell as described in this introductory chapter. A variety of microscopy characterization techniques such as: FE-SEM, electron backscatter diffraction (EBSD), AFM and Raman spectroscopy are then used to correlate the localized activity to physical properties of the investigated surfaces.

In Chapter 3, SECCM studies of a polycrystalline platinum surface highlight the significant variations in electrochemical activity that can be measured at an electrode surface due to variations in localized crystallographic orientation and the presence of grain boundaries. This sets the motivation and justification to study the electrochemical activity of electrodes at the submicron to nanoscale using SECCM. An ostensibly simple redox couple ($Fe^{2+/3+}$) in two different acidic media on a polycrystalline platinum foil is utilized as a model system and the localized crystallographic orientation of the surface is determined by EBSD analysis.

In Chapter 4, the investigation of localized electrochemical activity at polycrystalline platinum electrodes is extended to room temperature ionic liquids (RTILs) to study the reduction of triiodide (I_3^-) to iodide (I^-) for the application of DSSCs as a counter electrode.

In Chapter 5, the SECCM platform is extended to the investigation of (photo)electrochemical systems. The coupling of illumination with high sensitivity current followers and external lock-in amplifiers to the SECCM setup is described and the resulting platform is demonstrated with two examples: imaging photo-anodes in DSSCs and electrodepsoition and characterization of conjugated polymers on a transparent electrode for organic photovoltaic devices.

Finally, in Chapter 6, a correlation study of (photo)electrochemical activity and film morphology (thickness and order) for a model electro-deposited organic polymer is presented using the platform described in chapter 5. Film thickness and order were obtained by AFM and Raman spectroscopy, respectively.

1.4 References

(1) *Applied Scanning Probe Methods VII : Biomimetics and Industrial Applications*; Bhushan; Bharat; Fuchs, Eds.; Springer: Berlin, 2007; Vol. VII.

(2) Ebejer, N.; Güell, A. G.; Lai, S. C. S.; McKelvey, K.; Snowden, M. E.; Unwin, P. R. *Annu. Rev. Anal. Chem.* **2013**, *6*, 329.

(3) Kranz, C. *Analyst* **2014**, *139*, 336.

(4) Bandarenka, A. S.; Ventosa, E.; Maljusch, A.; Masa, J.; Schuhmann, W. *Analyst* **2014**.

(5) Chen, C.-C.; Zhou, Y.; Baker, L. A. *Annu. Rev. Anal. Chem.* **2012**, *5*, 207.

(6) Engstrom, R. C.; Weber, M.; Wunder, D. J.; Burgess, R.; Winquist, S. *Anal. Chem.* **1986**, *58*, 844.

(7) Bard, A. J.; Fan, F. R. F.; Kwak, J.; Lev, O. *Anal. Chem.* **1989**, *61*, 132.

(8) Bard, A. J.; Fan, F. R. F.; Pierce, D. T.; Unwin, P. R.; Wipf, D. O.; Zhou, F. *Science* **1991**, *254*, 68.

(9) Amemiya, S.; Bard, A. J.; Fan, F.-R. F.; Mirkin, M. V.; Unwin, P. R. *Annu. Rev. Anal. Chem.* **2008**, *1*, 95.

(10) Beaulieu, I.; Kuss, S.; Mauzeroll, J.; Geissler, M. *Anal. Chem.* **2011**, *83*, 1485.

(11) Amemiya, S.; Guo, J.; Xiong, H.; Gross, D. A. *Anal. Bioanal. Chem.* **2006**, *386*, 458.

(12) Schulte, A.; Nebel, M.; Schuhmann, W. *Annu. Rev. Anal. Chem.* **2010**, *3*, 299.

(13) Edwards, M. A.; Martin, S.; Whitworth, A. L.; Macpherson, J. V.; Unwin, P. R. *Physiological Measurement* **2006**, *27*, R63.

(14) Bertoncello, P. *Energy Environ. Sci.* **2010**, *3*, 1620.

(15) Lai, S. C. S.; Macpherson, J. V.; Unwin, P. R. *MRS Bulletin* **2012**, *37*, 668.

(16) Amemiya, S. In *Characterization of Materials*; John Wiley & Sons, Inc.: 2002.

(17) Szunerits, S.; Pust, S. E.; Wittstock, G. *Anal. Bioanal. Chem.* **2007**, *389*, 1103.

(18) Bard, A. J.; Mirkin, M. V. *Scanning Electrochemical Microscopy*; 2nd ed.; CRC Press: Boca Raton, Fla., 2012.

(19) Wittstock, G.; Burchardt, M.; Pust, S. E.; Shen, Y.; Zhao, C. *Angew. Chem., Int. Ed.* **2007**, *46*, 1584.

(20) Mirkin, M. V.; Nogala, W.; Velmurugan, J.; Wang, Y. *Phys. Chem. Chem. Phys.* **2011**, *13*, 21196.

(21) Guo, S. X.; Unwin, P. R.; Whitworth, A. L.; Zhang, T. *Prog. React. Kinet. Mech.* **2004**, *29*, 125.

(22) Nebel, M.; Eckhard, K.; Erichsen, T.; Schulte, A.; Schuhmann, W. *Anal. Chem.* **2010**, *82*, 7842.

(23) Takahashi, Y.; Shiku, H.; Murata, T.; Yasukawa, T.; Matsue, T. *Anal. Chem.* **2009**, *81*, 9674.

(24) Yamada, H.; Ogata, M.; Koike, T. *Langmuir* **2006**, *22*, 7923.

(25) Etienne, M.; Layoussifi, B.; Giornelli, T.; Jacquet, D. *Electrochem. Commun.* **2012**, *15*, 70.

(26) Takahashi, Y.; Shevchuk, A. I.; Novak, P.; Murakami, Y.; Shiku, H.; Korchev, Y. E.; Matsue, T. *J. Am. Chem. Soc.* **2010**, *132*, 10118.

(27) Comstock, D. J.; Elam, J. W.; Pellin, M. J.; Hersam, M. C. *Anal. Chem.* **2010**, *82*, 1270.

(28) Morris, C. A.; Chen, C. C.; Baker, L. A. *Analyst* **2012**, *137*, 2933.

(29) Paulose Nadappuram, B.; McKelvey, K.; Al-Botros, R.; Colburn, A. W.; Unwin, P. R. *Anal. Chem.* **2013**, *85*, 8070.

(30) Takahashi, Y.; Shevchuk, A. I.; Novak, P.; Zhang, Y.; Ebejer, N.; Macpherson, J. V.; Unwin, P. R.; Pollard, A. J.; Roy, D.; Clifford, C. A.; Shiku, H.; Matsue, T.; Klenerman, D.; Korchev, Y. E. *Angew. Chem., Int. Ed.* **2011**, *50*, 9638.

(31) Kurulugama, R. T.; Wipf, D. O.; Takacs, S. A.; Pongmayteegul, S.; Garris, P. A.; Baur, J. E. *Anal. Chem.* **2005**, *77*, 1111.

(32) Alpuche-Aviles, M. A.; Wipf, D. O. *Anal. Chem.* **2001**, *73*, 4873.

(33) Macpherson, J. V.; Unwin, P. R.; Hillier, A. C.; Bard, A. J. *J. Am. Chem. Soc.* **1996**, *118*, 6445.

(34) Kranz, C.; Friedbacher, G.; Mizaikoff, B. *Anal. Chem.* **2001**, *73*, 2491.

(35) Salomo, M.; Pust, S. E.; Wittstock, G.; Oesterschulze, E. *Microelectron. Eng.* **2010**, *87*, 1537.

(36) Macpherson, J. V.; Unwin, P. R. *Anal. Chem.* **1999**, *72*, 276.

(37) Wipf, D. O.; Bard, A. J. *Anal. Chem.* **1992**, *64*, 1362.

(38) Wipf, D. O.; Bard, A. J.; Tallman, D. E. *Anal. Chem.* **1993**, *65*, 1373.

(39) Edwards, M. A.; Whitworth, A. L.; Unwin, P. R. *Anal. Chem.* **2011**, *83*, 1977.

(40) McKelvey, K.; Edwards, M. A.; Unwin, P. R. *Anal. Chem.* **2010**, *82*, 6334.

(41) McKelvey, K.; Snowden, M. E.; Peruffo, M.; Unwin, P. R. *Anal. Chem.* **2011**, *83*, 6447.

(42) Lazenby, R. A.; McKelvey, K.; Unwin, P. R. *Anal. Chem.* **2013**, *85*, 2937.

(43) Cortés-Salazar, F.; Momotenko, D.; Lesch, A.; Wittstock, G.; Girault, H. H. *Anal. Chem.* **2010**, *82*, 10037.

(44) Cortes-Salazar, F.; Momotenko, D.; Girault, H. H.; Lesch, A.; Wittstock, G. *Anal. Chem.* **2011**, *83*, 1493.

(45) Lesch, A.; Momotenko, D.; Cortes-Salazar, F.; Wirth, I.; Tefashe, U. M.; Meiners, F.; Vaske, B.; Girault, H. H.; Wittstock, G. *J. Electroanal. Chem.* **2012**, *666*, 52.

(46) Lesch, A.; Vaske, B.; Meiners, F.; Momotenko, D.; Cortes-Salazar, F.; Girault, H. H.; Wittstock, G. *Angew. Chem., Int. Ed.* **2012**, *51*, 10413.

(47) Lesch, A.; Momotenko, D.; Cortés-Salazar, F.; Roelfs, F.; Girault, H. H.; Wittstock, G. *Electrochim. Acta* **2013**, *110*, 30.

(48) Lesch, A.; Chen, P.-C.; Roelfs, F.; Dosche, C.; Momotenko, D.; Cortés-Salazar, F.; Girault, H. H.; Wittstock, G. *Anal. Chem.* **2013**, *86*, 713.

(49) Ebejer, N.; Schnippering, M.; Colburn, A. W.; Edwards, M. A.; Unwin, P. R. *Anal. Chem.* **2010**, *82*, 9141.

(50) Böhni, H.; Suter, T.; Schreyer, A. *Electrochim. Acta* **1995**, *40*, 1361.

(51) Mardare, A. I.; Wieck, A. D.; Hassel, A. W. *Electrochim. Acta* **2007**, *52*, 7865.

(52) Lohrengel, M. M.; Moehring, A.; Pilaski, M. *Electrochim. Acta* **2001**, *47*, 137.

(53) Lill, K. A.; Hassel, A. W.; Frommeyer, G.; Stratmann, M. *Electrochim. Acta* **2005**, *51*, 978.

(54) Hassel, A. W.; Seo, M. *Electrochim. Acta* **1999**, *44*, 3769.

(55) Staemmler, L.; Suter, T.; Bohni, H. *J. Electrochem. Soc.* **2004**, *151*, G734.

(56) Woldemedhin, M. T.; Raabe, D.; Hassel, A. W. *Phys. Status Solidi A* **2011**, *208*, 1246.

(57) Suter, T.; Böhni, H. *Electrochim. Acta* **1997**, *42*, 3275.

(58) Momotenko, D.; Cortes-Salazar, F.; Lesch, A.; Wittstock, G.; Girault, H. H. *Anal. Chem.* **2011**, *83*, 5275.

(59) Momotenko, D.; Qiao, L.; Cortes-Salazar, F.; Lesch, A.; Wittstock, G.; Girault, H. H. *Anal. Chem.* **2012**, *84*, 6630.

(60) Rodolfa, K. T.; Bruckbauer, A.; Zhou, D. J.; Korchev, Y. E.; Klenerman, D. *Angew. Chem., Int. Ed.* **2005**, *44*, 6854.

(61) Williams, C. G.; Edwards, M. A.; Colley, A. L.; Macpherson, J. V.; Unwin, P. R. *Anal. Chem.* **2009**, *81*, 2486.

(62) Vogel, A.; Schultze, J. W. *Electrochim. Acta* **1999**, *44*, 3751.

(63) Kollender, J. P.; Mardare, A. I.; Hassel, A. W. *ChemPhysChem* **2013**, *14*, 560.

(64) Klemm, S. O.; Schauer, J.-C.; Schuhmacher, B.; Hassel, A. W. *Electrochim. Acta* **2011**, *56*, 9627.

(65) Klemm, S. O.; Schauer, J.-C.; Schuhmacher, B.; Hassel, A. W. *Electrochim. Acta* **2011**, *56*, 4315.

(66) Klemm, S.; Pust, S.; Hassel, A.; Hüpkes, J.; Mayrhofer, K. J. *J. Solid State Electrochem.* **2012**, *16*, 283.

(67) Klemm, S. O.; Topalov, A. A.; Laska, C. A.; Mayrhofer, K. J. J. *Electrochem. Commun.* **2011**, *13*, 1533.

(68) Lohrengel, M. M.; Rosenkranz, C.; Klüppel, I.; Moehring, A.; Bettermann, H.; Bossche, B. V. d.; Deconinck, J. *Electrochim. Acta* **2004**, *49*, 2863.

(69) Cortes-Salazar, F.; Lesch, A.; Momotenko, D.; Busnel, J. M.; Wittstock, G.; Girault, H. H. *Anal. Methods* **2010**, *2*, 817.

(70) Hansma, P. K.; Drake, B.; Marti, O.; Gould, S. A.; Prater, C. B. *Science* **1989**, *243*, 641.

(71) Edwards, M. A.; Williams, C. G.; Whitworth, A. L.; Unwin, P. R. *Anal. Chem.* **2009**, *81*, 4482.

(72) Shevchuk, A. I.; Gorelik, J.; Harding, S. E.; Lab, M. J.; Klenerman, D.; Korchev, Y. E. *Biophys. J.* **2001**, *81*, 1759.

(73) Pastre, D.; Iwamoto, H.; Liu, J.; Szabo, G.; Shao, Z. *Ultramicroscopy* **2001**, *90*, 13.

(74) Novak, P.; Li, C.; Shevchuk, A. I.; Stepanyan, R.; Caldwell, M.; Hughes, S.; Smart, T. G.; Gorelik, J.; Ostanin, V. P.; Lab, M. J.; Moss, G. W. J.; Frolenkov, G. I.; Klenerman, D.; Korchev, Y. E. *Nat. Methods* **2009**, *6*, 279.

(75) Sanchez, D.; Arand, U.; Gorelik, J.; Benham, C. D.; Bountra, C.; Lab, M.; Klenerman, D.; Birch, R.; Arland, P.; Korchev, Y. *J. Neurosci. Meth.* **2007**, *159*, 26.

(76) Gorelik, J.; Zhang, Y. J.; Shevchuk, A. I.; Frolenkov, G. I.; Sanchez, D.; Lab, M. J.; Vodyanoy, I.; Edwards, C. R. W.; Klenerman, D.; Korchev, Y. E. *Mol. Cell. Endocrinol.* **2004**, *217*, 101.

(77) Happel, P.; Hoffmann, G.; Mann, S. A.; Dietzel, I. D. *J. Microsc-Oxford* **2003**, *212*, 144.

(78) Shevchuk, A. I.; Frolenkov, G. I.; Sanchez, D.; James, P. S.; Freedman, N.; Lab, M. J.; Jones, R.; Klenerman, D.; Korchev, Y. E. *Angew. Chem., Int. Ed.* **2006**, *45*, 2212.

(79) Korchev, Y. E.; Negulyaev, Y. A.; Edwards, C. R.; Vodyanoy, I.; Lab, M. J. *Nat. Cell Biol.* **2000**, *2*, 616.

(80) Proksch, R.; Lal, R.; Hansma, P. K.; Morse, D.; Stucky, G. *Biophys. J.* **1996**, *71*, 2155.

(81) Bruckbauer, A.; Ying, L. M.; Rothery, A. M.; Zhou, D. J.; Shevchuk, A. I.; Abell, C.; Korchev, Y. E.; Klenerman, D. *J. Am. Chem. Soc.* **2002**, *124*, 8810.

(82) Bruckbauer, A.; Zhou, D.; Kang, D. J.; Korchev, Y. E.; Abell, C.; Klenerman, D. *J. Am. Chem. Soc.* **2004**, *126*, 6508.

(83) Bruckbauer, A.; Zhou, D.; Ying, L.; Korchev, Y. E.; Abell, C.; Klenerman, D. *J. Am. Chem. Soc.* **2003**, *125*, 9834.

(84) Wang, Y.; Kececi, K.; Velmurugan, J.; Mirkin, M. V. *Chem. Sci.* **2013**, *4*, 3606.

(85) Zhan, D. P.; Li, X.; Zhan, W.; Fan, F. R. F.; Bard, A. J. *Anal. Chem.* **2007**, *79*, 5225.

(86) Yatziv, Y.; Turyan, I.; Mandler, D. *J. Am. Chem. Soc.* **2002**, *124*, 5618.

(87) Dudin, P. V.; Snowden, M. E.; Macpherson, J. V.; Unwin, P. R. *ACS Nano* **2011**, *5*, 10017.

(88) Day, T. M.; Unwin, P. R.; Macpherson, J. V. *Nano Lett.* **2007**, *7*, 51.

(89) Kinnear, S. L.; McKelvey, K.; Snowden, M. E.; Peruffo, M.; Colburn, A. W.; Unwin, P. R. *Langmuir* **2013**.

(90) Lai, S. C. S.; Dudin, P. V.; Macpherson, J. V.; Unwin, P. R. *J. Am. Chem. Soc.* **2011**, *133*, 10744.

(91) Aaronson, B. D. B.; Chen, C.-H.; Li, H.; Koper, M. T. M.; Lai, S. C. S.; Unwin, P. R. *J. Am. Chem. Soc.* **2013**, *135*, 3873.

(92) Güell, A. G.; Meadows, K. E.; Dudin, P. V.; Ebejer, N.; Macpherson, J. V.; Unwin, P. R. *Nano Lett.* **2013**, *14*, 220.

(93) Kirkman, P. M.; Güell, A. G.; Cuharuc, A. S.; Unwin, P. R. *J. Am. Chem. Soc.* **2013**.

(94) McKelvey, K.; O'Connell, M. A.; Unwin, P. R. *Chem. Commun.* **2013**.

(95) Patel, A. N.; McKelvey, K.; Unwin, P. R. *J. Am. Chem. Soc.* **2012**, *134*, 20246.

(96) Güell, A. G.; Ebejer, N.; Snowden, M. E.; McKelvey, K.; Macpherson, J. V.; Unwin, P. R. *Proc. Natl. Acad. Sci. U. S. A.* **2012**, *109*, 11487.

(97) Putman, C. A.; van der Werf, K. O.; de Grooth, B. G.; van Hulst, N. F.; Greve, J.; Hansma, P. K. In *Scanning Probe Microscopies* Los Angeles, CA 1992; Vol. 1639, p 198.

(98) Patel, A. N.; Tan, S.-y.; Unwin, P. R. *Chem. Commun.* **2013**, *49*, 8776.

Chapter 2 Experimental

2.1 Reagents and solutions

Table 2.1 List of chemicals, chemical purity and suppliers used in this work.

Chemical/ Material	Grade/Purity	Supplier
(3- aminopropyl)trimethoxysilane	≥ 97 % purity	Sigma Aldrich
(3-mercaptopropyl)trimethoxysilane	≥ 95 % purity	Sigma Aldrich
3-hexylthiophene (3HT)	≥99 % purity	Sigma Aldrich
Acetone	Laboratory reagent	Fischer Chemicals
Acetonitrile	≥ 99.0 % purity	Fluka
Ag wire	0.255 mm 3N	MaTeck
Butyl-3-methylimidazolium tetrafluoroborate [BMIm][BF_4]	≥ 97.0 % purity, (HPLC grade)	Sigma-Aldrich
cis-diisothiocyanato-bis(2,2'-bipyridyl-4,4'-dicarboxylato) ruthenium(II) bis(tetrabutylammonium) (N719)	≥98 % purity	Solaronix
Dichlorodimethylsilane	≥ 99 % purity	Acros
Ethanol	Laboratory reagent	Fischer Chemicals
$Fe(ClO_4)_2{\cdot}xH_2O$	98 % purity	Sigma-Aldrich
$FeSO_4{\cdot}7H_2O$	≥ 99.0 % purity	Sigma-Aldrich
H_2SO_4	99.999 % purity	Sigma-Aldrich
$HClO_4$	≤ 0.001 % chloride	Acros
I_2	98 % purity	Fischer Chemicals
Pd wire	> 99.95 %	MaTeck
Polycrystalline Pt foil	purity > 99.95 %, 0.0125 mm thickness	Advent Research Materials
Tetrabutylammonium iodide (TBAI)	98 % purity	Acros Organics
TiO_2 nanoparticles (P25, Degussa)	(mean particle size 30 nm) ≥ 97% purity	Degussa

2.2 SECCM

A description of the general experimental setup and working principles of SECCM are described in section 1.2. In this section, specifications of the components used in the work herein, are given. In addition, SECCM tip fabrication and the employment of an environmental cell are presented.

2.2.1 SECCM hardware setup

Unless otherwise stated, all SECCM experiments presented in this thesis were performed on the same home-built working station utilizing a 750 k samples/sec FPGA card (PCIe 7852R, National Instruments), controlled through a LabVIEW 11.0 interface (National Instruments, USA).[1-3] A home built bipotentiostat was used to control the bias voltage (V_2 in Figure 1.2b) between the QRCEs. V_1 was accessed through the LabVIEW interface and fed through the home-built potentiostat. The SECCM tip was mounted on a piezo-electric positioning block (NanoCube, Physik Instrumente, UK) with a range of 100 µm in each direction (*x*, *y* and *z*) to control the movement of the tip in the horizontal plane (*xy* coordinates) of the surface of interest, as well as the height (*z* coordinate). In the cases positional (vertical) feedback was maintained through the alternating current (i_{ac}) component in i_{dc}, a small modulation to the tip height (*z* coordinate), with a magnitude corresponding to ~ 10 % of the tip diameter was employed using a lock-in amplifier (SR810, Stanford Research Systems, USA). For the frequencies used in a particular scan see the appropriate experimental section in each chapter.

2.2.2 Tip fabrication SECCM

SECCM probes were fabricated from borosilicate theta pipettes, pulled to a sharp point in a laser puller with a P-2000 from Sutter Instruments (Figure 2.1). The size of the probe can be controlled by adjusting the pulling parameters, with probes between 100 nm and tens of microns across at the tip end fabricated easily and quickly. The pulling parameters differ between laser pullers, but for a typical 500 nm borosilicate probe on a P-2000 laser puller the parameters are: line 1: heat = 600, filament = 4, velocity = 30, delay = 150. pull = 20; line 2: heat = 500, filament = 4, velocity = 30, delay = 150. pull = 60; line 3 heat = 500, filament = 3, velocity = 30, delay = 135. pull = 60.

Upon pulling of the capillary, two SECCM probes are produced (Figure 2.1b) with the shape of each tip being the mirror image of the other. One tip is used for SECCM imaging (filled with electrolyte as described below) and the other, which is closely identical, is used for shape and size characterization by FE-SEM.

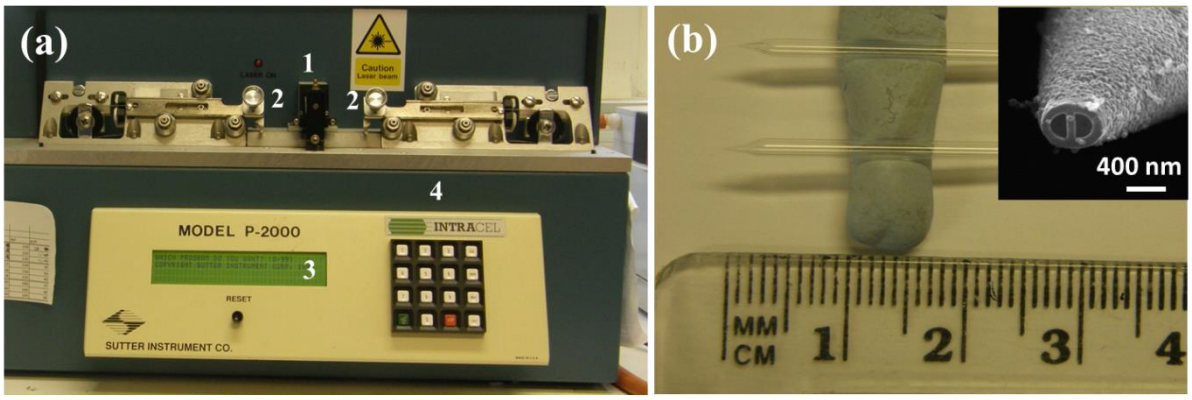

Figure 2.1 SECCM tip fabrication. (a) P2000, Sutter Instruments, laser puller: laser mirror case (1), capillary clamps (2), parameter display unit (3) and control panel (4).

(b) Photograph of the resulting tips of a pulled capillary. Inset shows a typical field emission-scanning electron micrograph (FE-SEM) of a SECCM probe.

To help confine an aqueous meniscus, the outside walls of the pipette were silanized using dimethyldichlorosilane [$Si(CH_3)_2Cl_2$].[1] This was achieved by inserting the pipette in $Si(CH_3)_2Cl_2$ while flowing argon gas at an elevated pressure through the pipette (typically between 2 to 8 bar) to avoid the silanization of the internal part of the pipette. The tip was immersed in $Si(CH_3)_2Cl_2$ for a duration of one minute followed by leaving the tip to dry in air, while argon was still flowed through for another two minutes. Silanization of the tips was not required when RTILs were used as electrolytes.

Both barrels of the sharp theta pipettes were filled with electrolyte solution using a microfil syringe inserted through the un-pulled end of the capillary. In the cases RTIL electrolytes were employed, a heat gun was used to assist the filling of the tip by gently heating the capillary to lower the viscosity of the RTIL. The electrolyte solution naturally forms a small liquid meniscus over the end of the pipette, connecting the two barrels.[1,4] QRCEs were then inserted into each barrel, and a conductance cell was formed between the QRCEs and across the liquid meniscus. The QRCEs used in this thesis were: Pd-H_2[5,6] (chapter 3) and Ag (chapters 4, 5 and 6).

2.2.3 Environmental cell

In the cases environmental control was needed (Chapters 4, 5 and 6) the sample and scanning probe were placed in a dry environmental cell containing silica

gel (Figure 2.2). Dried nitrogen gas (passed through a glass vessel containing alumina base) was flowed into one side of the environmental chamber and out through an exit at the opposite wall. This procedure assisted in the removal of dissolved oxygen in the meniscus, as well as ensuring dryness of the droplet at the end of the SECCM tip.[7] All imaging was performed with a continuous nitrogen flow after de-aeration for at least an hour.

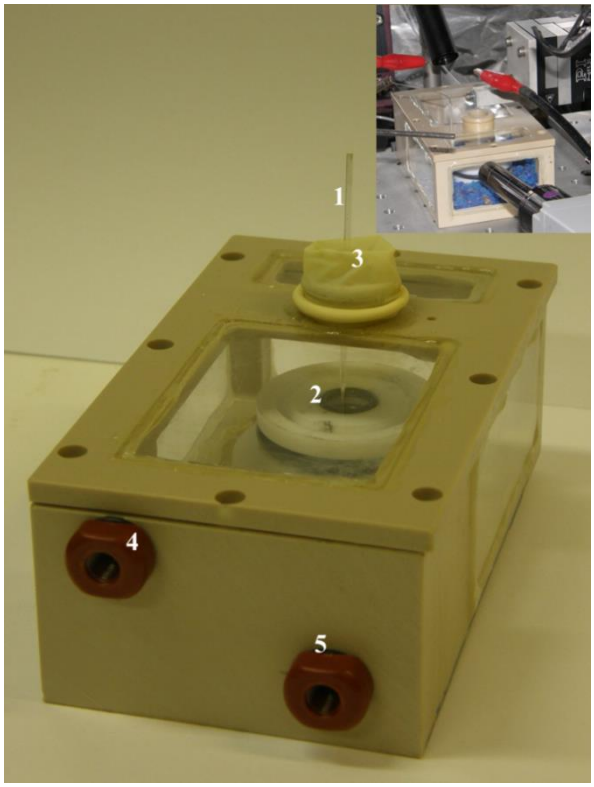

Figure 2.2 Environmental cell. SECCM tip (1). Sample holder for transparent electrodes (2). Finger cot for flexible movement of SECCM probe (3). N_2 gas outlet (4) and inlet (5). Inset shows the environmental cell with silica gel incorporated in the SECCM setup.

2.3 Electron backscatter diffraction (EBSD)

EBSD is a SEM based technique which utilizes the interaction between surface atoms and electrons from the electron beam to identify the crystallographic orientations of surfaces. The diffraction patterns of the primary electrons from the surface are a unique characteristic of the crystallographic orientation and the nature of the material.[8] A schematic setup of EBSD is shown in Figure 2.3 In brief, an electron beam is directed to a 70° tilted sample and the diffraction pattern (Kikuchi bands) of the primary electrons is visualized and recorded on a phosphorous detection screen. The pattern is then fitted to a reference pattern obtained from a database of calibrated diffraction patterns for the substrate of interest. The electron beam is scanned across the surface and an analysis programme then reconstructs an orientation map.

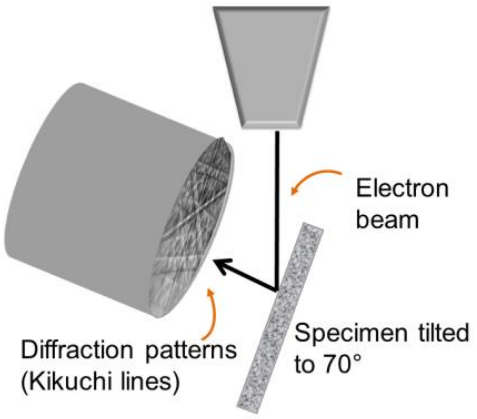

Figure 2.3 Electron backscatter diffraction (EBSD) schematic.

The EBSD images of platinum substrates (in Chapters 3 and 4) were recorded on a Zeiss SUPRA 55 variable-pressure field emission scanning electron microscope (FE-SEM) at 20 kV on a 70° tilted sample with an EDAX TSL EBSD system, after the SECCM scans. The samples were rinsed with deionized water before insertion into the vacuum chamber of the EBSD.

2.4 Preparation of transparent Au substrates

Transparent Au electrodes on glass were prepared using the original method.[9] In brief, microscope glass slides (1.2 mm thick, Thermo scientific, UK) were cut to a dimension of approx. 1 cm^2 and rinsed thoroughly with de-ionized water and iso-propanol followed by washing with hot acetone vapour. The glass samples were then treated with UV/O_3 for 15 minutes and immediately after, transferred to a desiccator in which they were exposed to the vapour of a 1:1 (v/v) mixture of (3-

aminopropyl)trimethoxysilane at 150 mbar for 4 hours. Au was then evaporated on the substrates at a rate of 0.1 nm s^{-1} to form a 40 nm thick homogeneous layer.

2.5 References

(1) Ebejer, N.; Schnippering, M.; Colburn, A. W.; Edwards, M. A.; Unwin, P. R. *Anal. Chem.* **2010**, *82*, 9141.

(2) Ebejer, N.; Güell, A. G.; Lai, S. C. S.; McKelvey, K.; Snowden, M. E.; Unwin, P. R. *Annu. Rev. Anal. Chem.* **2013**, *6*, 329.

(3) Snowden, M. E.; Güell, A. G.; Lai, S. C. S.; McKelvey, K.; Ebejer, N.; O'Connell, M. A.; Colburn, A. W.; Unwin, P. R. *Anal. Chem.* **2012**, *84*, 2483.

(4) Liu, B.; Shao, Y.; Mirkin, M. V. *Anal. Chem.* **1999**, *72*, 510.

(5) Lai, S. C. S.; Dudin, P. V.; Macpherson, J. V.; Unwin, P. R. *J. Am. Chem. Soc.* **2011**, *133*, 10744.

(6) Aaronson, B. D. B.; Chen, C.-H.; Li, H.; Koper, M. T. M.; Lai, S. C. S.; Unwin, P. R. *J. Am. Chem. Soc.* **2013**, *135*, 3873.

(7) Zhao, C.; Bond, A. M.; Compton, R. G.; O'Mahony, A. M.; Rogers, E. I. *Anal. Chem.* **2010**, *82*, 3856.

(8) König, U.; Davepon, B. *Electrochim. Acta* **2001**, *47*, 149.

(9) Stec, H. M.; Hatton, R. A. *Adv. Energy Mater*.**2013**, *3*, 193.

Chapter 3 Pseudo-Single-Crystal Electrochemistry on Polycrystalline Electrodes: Visualizing Activity at Grains and Grain Boundaries on Platinum for the Fe^{2+}/Fe^{3+} Redox Reaction

Abstract

The influence of electrode surface structure on electrochemical reaction rates and mechanisms is a major theme in electrochemical research, especially as electrodes with inherent structural heterogeneities are used ubiquitously. Yet, probing local electrochemistry and surface structure at complex surfaces is challenging. In this chapter, high spatial resolution SECCM complemented with electron backscatter diffraction (EBSD) is demonstrated as a means of performing 'pseudo-single-crystal' electrochemical measurements at individual grains of a polycrystalline platinum electrode, while also allowing grain boundaries to be probed. Using the $Fe^{2+/3+}$ couple as an illustrative case, a strong correlation is found between local surface structure and electrochemical activity. Variations in electrochemical activity for individual high index grains, visualized in a weakly adsorbing perchlorate medium, show that there is higher activity on grains with a significant (101) orientation contribution, compared to those with (001) and (111) contribution, consistent with findings on single-crystal electrodes. Interestingly, for Fe^{2+} oxidation in a sulfate medium a different pattern of activity emerges. SECCM reveals only minor variations in activity between individual grains, again consistent with single-crystal studies, but much enhanced activity at grain boundaries. This suggests that these sites may contribute significantly to the overall electrochemical behavior measured on the macroscale.

3.1 Introduction

Identifying correlations between the electrochemical activity and morphology (in particular, the crystallographic orientation) of electrode surfaces is of major fundamental importance towards achieving a better understanding of heterogeneous electron transfer (ET) processes. Moreover, the rational development of electrocatalysts,[1,2] for a variety of applications, from energy conversion and storage[3-7] to electrosynthesis[8,9] and electrochemical sensors,[10] requires knowledge of electrode structure-activity relationships. A major area of interest is the structure-dependent reactivity of platinum and other platinum-group metals, which have proven to be among the most efficient electrocatalysts for a wide variety of reactions.[11,12]

A common approach to investigating the relationship between surface structure and electrochemical activity is to employ well-defined single-crystal electrodes.[3,13,14] However, while valuable information can be obtained, such studies are challenging, as well as expensive and time-consuming, as each electrode needs to be carefully prepared, characterized and handled so that only a single surface orientation is assured. Furthermore, the effect of boundaries between different crystallographic grains cannot be probed on such surfaces, even though they may play a significant (or possibly even dominant) role in surface reactivity.[15,16] These challenges could be circumvented if one could directly probe the local structure of a polycrystalline sample, for example with EBSD,[17] and correlate this with localized electrochemical measurements.[17,18]

An interesting approach for performing localized electrochemistry on a

polycrystalline surface is to prepare an array of individually addressable micrometer scale electrodes through lithographic processing.[17] However, due to the irregular shape and size of crystalline grains, the employment of lithographic techniques to expose specific grains is technically very demanding. Furthermore, lithographic processing is rather involved and can leave residual contaminations which may impact the reactivity of the electrode.[19,20] Another approach is to limit the contacted area of the working electrode by employing droplet based techniques.[18,21-23] However, methods of this type have tended to be restricted to static point-by-point measurements (usually on a large scale), and the mapping of an area of an electrode has proved to be time consuming and difficult technically. As mentioned in chapter 1, an attractive feature of SECCM is that each location on the electrode is only exposed to the electrolyte solution briefly, minimizing electrode fouling[21] and other undesired processes. In contrast to SECM,[24,25] which is also powerful for visualizing heterogeneous electrode substrates,[26-29] SECCM measures the electrochemical processes of interest directly, in a manner that is similar to conventional dynamic electrochemistry, and readily achieves higher spatial resolution.

In this chapter, we study the one-electron oxidation of Fe^{2+} to Fe^{3+} in aqueous media on a polycrystalline platinum surface with SECCM, and correlate the local activity with the corresponding microscale crystallographic orientation of the surface determined by EBSD. Although the surface condition in this method is different from that in a macroscale measurement (as will be discussed shortly), the findings are compared to studies performed on mm-sized single-crystal electrodes, to assess the validity of this approach. The $Fe^{2+/3+}$ redox couple is especially interesting, as it is an ostensibly simple one-electron process, although showing strong kinetic limitations and often considered to be a model inner-sphere process based on

macroscopic measurements on polycrystalline metal electrodes.[30] In recent work on polycrystalline boron doped diamond, we have found electron transfer for this redox couple to be very strongly surface sensitive.[21] Similar findings have been reported for other carbon electrode materials[31,32] as well as metal electrodes.[33] However, the origin of the structure-sensitivity is unclear and has been a topic of debate, with explanations ranging from differences in surface coordination of the $Fe^{2+/3+}$ species,[34] variations in the local density of electronic states of the electrode,[33] changes in double layer structure with the surface structure,[35-37] different crystallographic facets of an electrode having different potential of zero charge[35,36] and/or effects due to surface sensitive anion adsorption.[38,39] Fe^{2+} oxidation on platinum is further complicated by the fact that it takes place at potentials at which oxidation of the platinum surface also occurs.[40] Platinum surface oxidation consists of a number of steps whose significance are timescale and potential dependent.[40,41] Initially, surface oxidation occurs through the fast formation of Pt-OH.[42] Further oxidation to form PtO and PtO_2 occurs slowly over the course of seconds to tens of seconds. Therefore, the electrochemical response can also be influenced by the timescale of the measurement.[40,43] Based on recent work,[21,26,44-50] SECCM provides a powerful method to investigate whether structural effects hold for the oxidation of Fe^{2+} on polycrystalline platinum.

We demonstrate that SECCM coupled with EBSD is a powerful approach to perform 'pseudo-single-crystal' experiments on a polycrystalline (platinum) substrate. In particular, owing to the short contact time of SECCM, we show that we can obtain information on surface reactivity before (irreversible) surface oxidation sets in, allowing us to probe the structure-activity relationship for Fe^{2+} oxidation at significant overpotentials. Notably, we identify distinct patterns of spatial ET activity

and anion effects, which provide a new view of heterogeneous redox reactions at polycrystalline platinum. This evidently has significant implications for kinetic and mechanistic studies at polycrystalline electrodes, generally, which are usually studied by macroscopic techniques, such as cyclic voltammetry, without the ability to assess whether reactions can be considered to be uniform across a substrate.

3.2 Experimental

3.2.1 Solutions

All electrolyte solutions were prepared freshly from high purity water (Milli-Q, Millipore, 18.2 MΩ cm resistivity at 25 °C) and were used as received (see Table 2.1 in section 2.1 for list of chemicals, purity and suppliers).

3.2.2 SECCM setup

The SECCM setup for the work herein is shown schematically in Figure 3.1. The tapered dual barrel (theta) pipette was pulled to form a sharp tip with an outer diameter of ~ 2.0 μm. The exterior surface of the pulled pipette was silanized (see section 2.2.2). Each barrel was filled with the solution of interest and a Pd-H_2 QRCE was inserted into each barrel. A bias potential, V_2, was applied between the QRCEs: 0.2 V for the $HClO_4$ study and 0.5 V for the H_2SO_4 study. During experiments, the *z*-piezoelectric positioner (perpendicular to the substrate) was oscillated at 70 Hz with 58 nm peak amplitude. This oscillation produced an alternating ion current between the barrels (i_{ac} in Figure 3.1) upon contact of the droplet meniscus at the end of the pipette with the working electrode substrate (platinum foil).[45] The resulting AC magnitude, typically in the range of 150 pA (~ 2 % of the mean conductance

current), was used as a set point (feedback) to maintain a constant tip-to-substrate separation (meniscus thickness). The substrate electrode was connected to a high sensitivity current amplifier and held at ground.

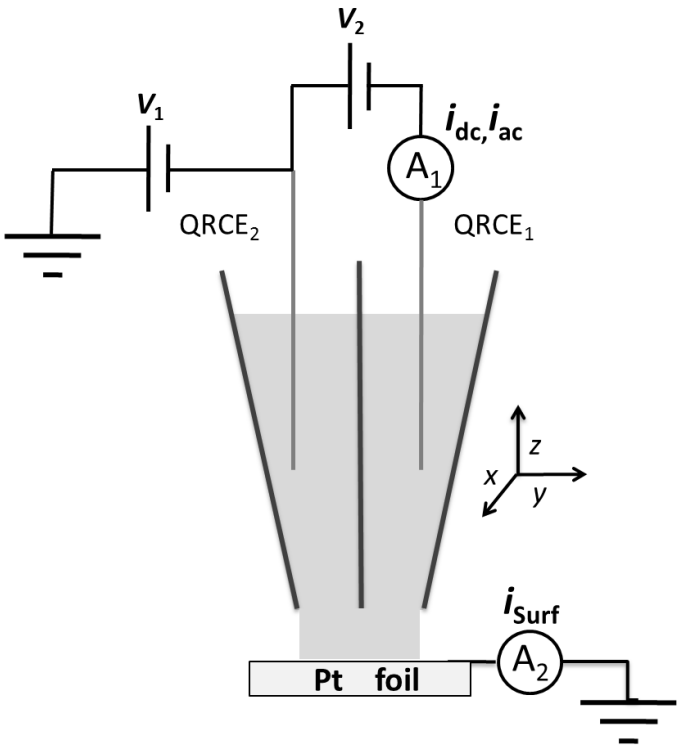

Figure 3.1 Schematic of SECCM setup for platinum foil investigation. A piece of platinum foil (see text) served as the working electrode. Pd-H_2 quasi-reference/counter electrodes (QRCEs) were inserted into each barrel of a pipette, used as an imaging probe. V_1 : potential applied to the $QRCE_2$ (relative to ground) ; V_2 : potential bias applied between $QRCE_1$ and $QRCE_2$; i_{dc}, i_{ac}: direct and alternating current between the QRCEs, respectively ; i_{Surf} : current through the substrate.

3.2.3 Single crystal measurements

Single-crystal measurements were performed on bead-type single-crystal electrodes between 1 mm and 3 mm diameter, prepared according to Clavilier's method.[51] Prior to each experiment, the electrodes were flame annealed and allowed to cool down in a hydrogen/argon mixture (*ca.* 3:1) after which they were transferred to the electrochemical cell under the protection of a droplet of deoxygenated ultra-pure water. A piece of platinum foil and a reversible hydrogen electrode (connected via a Luggin capillary) were employed as counter and reference electrode, respectively. All glassware was cleaned by boiling in a 1:1 mixture of nitric acid and sulfuric acid, followed by repeated boiling in ultra-pure water.

3.2.4 Working electrode

Before SECCM imaging, the Pt foil was cleaned by flame-annealing followed by potential cycling 200 times from 0 V to 1.6 V and ending at 0 V to ensure an oxide-free surface.

3.2.5 Preparation of Pd-H_2 quasi-reference counter electrodes (QRCEs)

The Pd-H_2 REs and QRCEs (E^0 = 50 mV *vs* the reversible hydrogen electrode)[52] were prepared by evolving hydrogen on a palladium wire in a particular supporting electrolyte (either 10 mM H_2SO_4 or 10 mM $HClO_4$) until hydrogen bubbles were clearly visible on the surface of the wire, indicating hydrogen saturation. All potentials in this paper are reported relative to the Pd-H_2 RE or QRCE in the working solution.

3.2.6 SECCM scanning parameters and data acquisition

SECCM images were constructed from parallel line scans with a spacing of 2 μm between each line. A data point (pixel) was recorded every 1.5 μm over a period of 40 ms at a frequency of 25 kHz (corresponding to the average of 1000 measurements). Prior to collecting data at each pixel, a 20 ms waiting time was applied to minimize currents due to double layer charging and the initial surface oxidation process (*vide infra*).

3.2.7 EBSD

For the EBSD setup see section 2.3. In the work herein, EBSD images were constructed from diffraction patterns recorded every 2 μm in both *x* and *y* directions of the 60×60 μm scan.

3.3 Results and discussion

3.3.1 Macroscopic CVs of the Fe^{2+}/Fe^{3+} redox couple on a polycrystalline platinum foil

The one-electron oxidation of Fe^{2+} on a macroscopic scale was studied in both perchlorate and sulfate media on a polycrystalline platinum foil using cyclic voltammetry. Typical cyclic voltammograms (CVs) of 2 mM Fe^{2+} (from $FeClO_4)_2$) in 10 mM $HClO_4$ (pH = 2.06) and of 2 mM Fe^{2+} (from $FeSO_4$) in 10 mM H_2SO_4 (pH = 1.77) are shown in Figure 3.2a. The CVs in only the supporting electrolyte (*i.e.* without the Fe-salt), are shown in Figure 3.2b for comparison. The onset potential for Fe^{2+} oxidation (Figure 3.2a) is nearly 100 mV lower in sulfate than in perchlorate and shows a slightly steeper slope indicating that Fe^{2+} oxidation in perchlorate

medium is slower than that in sulfate. To make sure that this shift in onset potential is not due to a difference in the effective $Fe^{2+/3+}$ redox potential (E^0) in each of the systems, open voltage potentials of equimolar solutions of $Fe^{2+/3+}$ in the corresponding electrolytes were recorded and were found to be the same in both mediums (+0.85 V *vs* Pd-H_2). The observation of a slightly slower reactivity is in agreement with previous work on Fe^{2+} oxidation in both media.[38] Looking closer at the background CVs shown in Figure 3.2b, one can appreciate the differences in the surface oxidation state in the two media in the potential range close to the E^0 for $Fe^{2+/3+}$. The oxidation of platinum in the perchlorate medium starts roughly 100 mV earlier than in the sulfate medium. This has been attributed previously to the strong adsorption of the sulfate ions, inhibiting surface oxidation, compared to the weakly adsorbing perchlorate ions.[39,53] It can be seen that, in both sulfuric acid and perchloric acid, the oxidation of Fe^{2+} largely overlaps with the platinum surface oxidation region. The surface potentials applied in SECCM were chosen from these cyclic voltammograms, ranging from the onset of oxidation to the diffusion limited region.

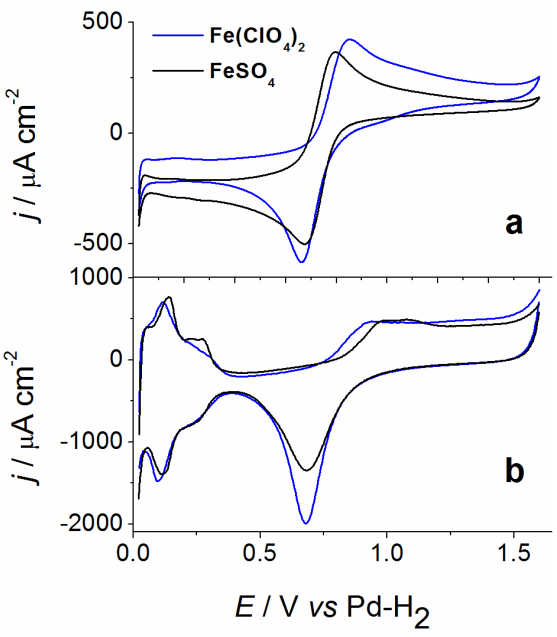

Figure 3.2 Macroscale CVs of the $Fe^{2+/3+}$ redox couple on platinum (a) Cyclic voltammograms of 2 mM $Fe(ClO_4)_2$ in 10 mM $HClO_4$ (blue line) and 2 mM $FeSO_4$ in 10 mM H_2SO_4 (black line) where the scan rate was 50 mVs^{-1} (b) Background voltammograms of 10 mM $HClO_4$ (blue line) and 10 mM H_2SO_4 (black line) where the scan rate was 500 mVs^{-1}

As highlighted in section 3.1, one of the challenges in studying the one-electron Fe^{2+} oxidation on platinum is that the measured current could represent a contribution of both Fe^{2+} oxidation and surface oxide formation processes. Two measures were taken in order to distinguish between Fe^{2+} oxidation and surface oxidation processes in the SECCM setup: (i) allowing a short waiting time, to minimize the current due to double layer charging and Pt-OH formation; and (ii) limiting the time of the measurement at each data point to reduce the influence of slow surface oxidation processes (PtO and PtO_2 formation). To quantify the magnitude of the background current due to oxide formation processes on the same time scale as the SECCM measurements for Fe^{2+} oxidation, we recorded an

electrochemical image of the platinum foil at a potential in only the oxide region in blank electrolyte (without Fe^{2+}) and found it to be negligible.

3.3.2 SECCM background images in sulfuric acid electrolyte

As the oxide formation on platinum show similar behaviors in both sulfate and perchlorate electrolytes (CVs in Figures 3.2b), we investigated this progress on the time scale of the SECCM measurements in sulfate medium only. An SECCM image was recorded in 10 mM H_2SO_4 at 1.1 V, with a bias potential (V_2) of 0.2 V applied between the QRCEs and is shown in Figure 3.3.

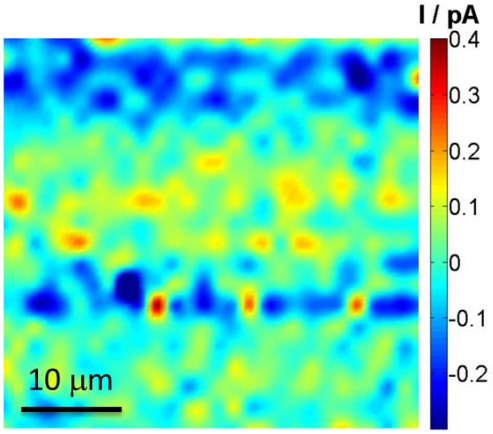

Figure 3.3 SECCM background image of polycrystalline platinum in 10 mM H_2SO_4 at 1.1 V vs Pd–H_2.

From Figure 3.3 it can be seen that the current is essentially zero over the entire area, indicating that the contribution of various surface oxidation processes to the measured currents in the images (as will be shown in the next section) is negligible. Finally, it should be mentioned that this image was recorded with the same current amplifier settings (100 pA/V) as for the Fe^{2+} oxidation images, so the small variations in current (<1 pA) are indicative of the noise level for the study reported in this work.

3.3.3 Fe^{2+} oxidation on platinum in perchloric acid solution

In order to probe the inherent electrochemical activity of polycrystalline platinum towards the oxidation of Fe^{2+}, without the added complexity of a strongly adsorbing anion, we initially employed a perchloric acid solution as electrolyte. Multiple SECCM activity images for the oxidation of 2 mM $Fe(ClO_4)_2$ in 10 mM $HClO_4$ on the polycrystalline platinum were obtained in the same area of the substrate, while holding the working electrode surface at potentials ranging from 0.75 V (close to the onset potential) to 1.4 V (mass transport limited potential) based on the macroscopic CVs in Figure 3.2a.

Two representative SECCM activity images of one area of the platinum surface at 0.8 and 1.0 V are shown in Figure 3.4a and 3.4b, with the corresponding EBSD image of the same area in Figure 3.4c. Five regions, each with different activity, can be identified in the SECCM image, and are labeled in Figure 3.4a (I-V). The relative activity of these regions (based on the surface current magnitude) is as follows: III > IV > V > II ≈ I. In addition, some variation in activity can be observed within individual regions.

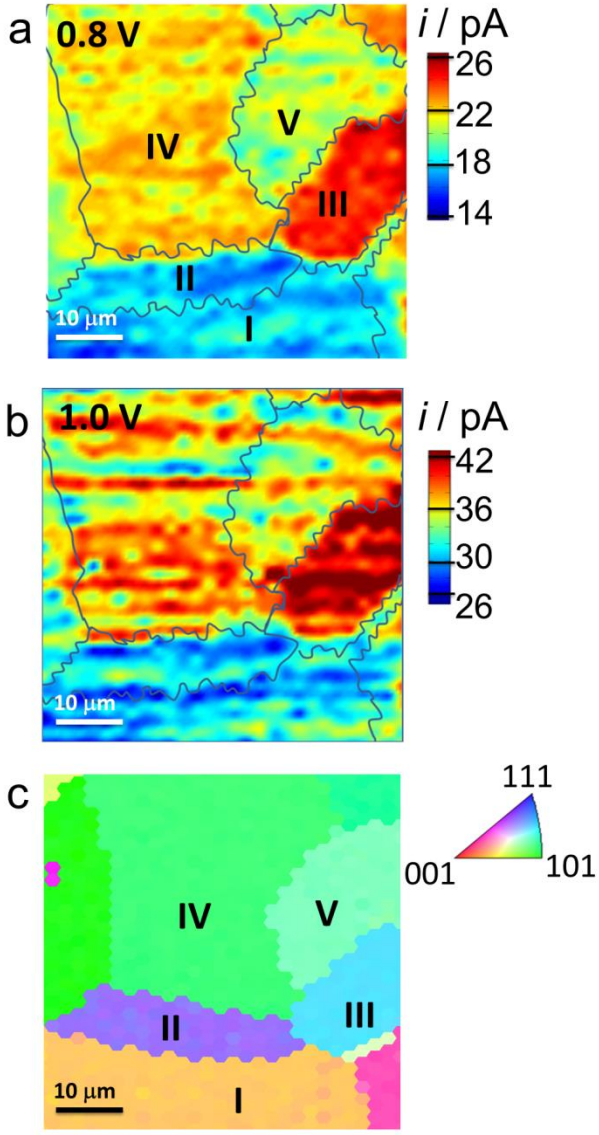

Figure 3.4 SECCM and EBSD images of a polycrystalline platinum electrode for the oxidation of Fe^{2+} in $HClO_4$. (a-b) Representative SECCM images of the oxidation of 2 mM Fe^{2+} to Fe^{3+} in 10 mM $HClO_4$ at 0.8 V and 1.0 V relative to Pd–H_2. The five grains in the scanned regions are labeled "I", "II", "III", "IV" and "V". The boundaries between the grains deduced from EBSD are marked with blue lines to guide the eye. (c) Corresponding EBSD image (tilted roughly 10° in the *xy* plane compared to the SECCM images) with the color coded orientation map of the scanned area.

Comparing the EBSD and SECCM maps, it is evident that the regions of distinctly different electrochemical activity correspond to particular grain structure by EBSD (Table 3.1). Notably, grains which have substantial (101) character (grains III, IV, and V) generally appear more active than grains having more (001) and (111) character (grains I and II).

Table 3.1. Surface orientations of areas marked in Figure 3.4

Grain	Approximate Miller index	Description
I	(13 5 1)	Mixed (001) and (101) character
II	(211)	(001) sites separated by short (111) terraces
III	(221)	(101) sites separated by short (111) terraces
IV	(771)	Mainly (101) character
V	(651)	Mainly (101) character

Upon closer inspection, there are variations in activity for the grains having mainly (101) character (III-V), with the most active grain (grain III) having some (111) character. This structure-dependent relative activity was evident at all investigated potentials and highlights that, on polycrystalline platinum, the Fe^{2+}/Fe^{3+} reaction rate is strongly structure-dependent at the microscopic level.

The impact of structure on electrochemical reaction rate is summarized quantitatively in Figure 3.5a, which shows the average surface current of the designated grain areas marked in Figure 3.4a, extracted from a series of SECCM activity maps, as a function of the electrode potential. From these current-potential (*i*-*E*) plots, it is evident that the surface current for all grains increases with the increasing potential (increasing driving force) as expected, based on macroscopic

CV measurements on polycrystalline platinum (Figure 3.2a), but is evidently grain-dependent. Note, particularly, that the relative activities between different grains are consistent throughout the entire potential range. Grain III, which has (101) sites, exhibits the highest activity at all potentials while grain II, which has (001) sites separated by short (111) terraces, exhibits the lowest activity at all potentials. Grains IV and V show intermediate activity between these two extremes, as highlighted above.

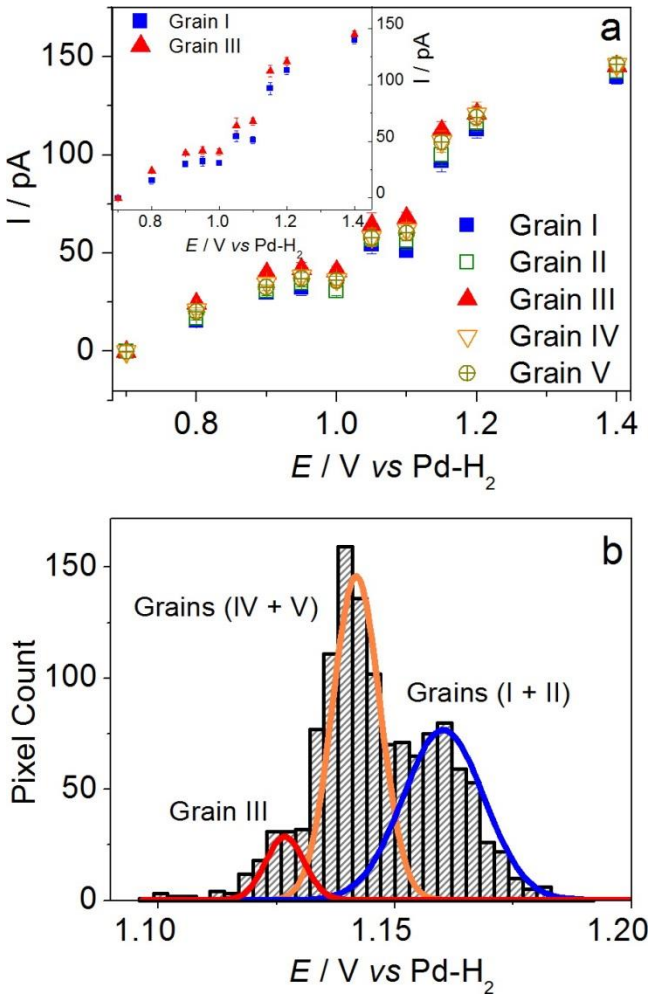

Figure 3.5 (a) *i-E* curves of electrochemical current as a function of applied surface potential for 2 mM $FeClO_4$ in 10 mM $HClO_4$. The current is the average from regions of the SECCM images where grains were identified. Inset shows the *i-E* curves for grain "I" and grain "III" for clarity. (b) Histogram of apparent half-wave potentials from spatially resolved *i-E* data at individual pixels in a series of SECCM images. Corresponding grains are labeled on the image.

Naturally, reactivity trends deduced from SECCM on the microcrystalline grains ought to hold when compared to the relative reactivity of single-crystal electrodes. In order to verify this, we recorded cyclic voltammograms for the oxidation of Fe^{2+} in perchlorate solution on low index platinum basal plane single-

crystal electrodes. Typical voltammograms, for the three basal faces, shown in Figure 3.6, highlight that the Pt(101) surface is most active, with an onset potential for Fe^{2+} oxidation *ca*. 200 mV earlier than on Pt(111) and Pt(001), which show comparable activity. Interestingly, the potential of zero total charge (pztc) for the basal planes of platinum show a similar trend at pH 2, with pztc of 0.18 V vs. Pd-H_2 for Pt (110) and 0.39 V and 0.38 V for Pt (111) and Pt (001), respectively.[54] This correspondence may suggest that the structure-sensitive activity for the oxidation of Fe^{2+} originates from variations of pztc, which strongly affects the double layer.[35,36]

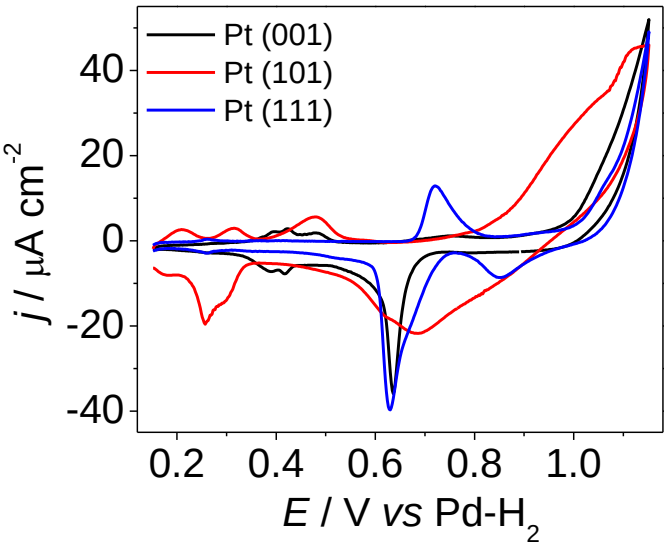

Figure 3.6 Platinum single crystal CVs for the oxidation of Fe^{2+} in $HClO_4$. Cyclic voltammograms of 2 mM $Fe(ClO_4)_2$ in 10 mM $HClO_4$ on Pt(111) electrode (blue line), Pt(001) electrode (black line) and Pt(101) electrode (red line). Scan rate was 10 mVs^{-1}.

Thus, it is evident that the single-crystal findings are qualitatively consistent with the trend in reactivity obtained from SECCM, confirming the validity of the SECCM approach. However, it is important to note that the variation between the electrochemical activities of single-crystal basal planes is much more pronounced than the variations between the different grains on the polycrystalline substrate. This is because grains on the polycrystalline substrate are not true basal-plane orientation, but are high index facets with contributions of all three basal planes. The variation in orientation within a single grain (seen as slight color variations in Figure 3.4c) may also be attributed to the variation of surface current within the individual grains (Figure 3.4a-b). On the other hand, a very positive outcome of the EBSD study coupled with SECCM is that high index facets can readily be investigated; such faces are extremely difficult to prepare and maintain as macroscopic single crystals.

The variations in reactivity in the SECCM images can further be analyzed quantitatively on a point-by-point basis. For each of the 1271 measurement points in an image, individual *i-E* curves were constructed (*i.e.* 1271 *i-E* curves, each with 10 points), and the half-wave potential corresponding to 75 pA (*ca*. half the mass transport limited current) for each *i-E* curve was extracted. The distribution of these apparent half-wave potentials is shown in Figure 3.5b, and can be deconvoluted into three prominent individual Gaussian distributions, centered around 1.16, 1.14 and 1.13 V. Based on the number of counts in each distribution, as well as the relative activity of the grains, we can assign the distribution centered around 1.16 V to grains I and II, the distribution around 1.14 V to grains IV and V, and the distribution around 1.13 V to grain III. It is worthwhile noting that the variation in apparent halfwave potentials, spans for 0.03 V, which might be considered relatively small,

but is readily detected in the SECCM experiments. Moreover, it is important to point out that this local variation in activity would have an impact on macroscopic CV measurements of heterogeneous ET on polycrystalline platinum. Electrode kinetic measurements on polycrystalline platinum tend to implicitly assume a uniform electrode surface[38,39,55,56] and evidently, at least for the case of Fe^{2+}/Fe^{3+} (and perhaps other reactions), this is not always appropriate.

Finally, to exclude the possibility that the observed variations in surface current between grains can be attributed to varaitions in roughness of the surface at individual grains, atomic force microscopy (AFM) images of the Pt foil were recorded and analysed (section 3.3.5), showing average roughness (R_a) of 5.46 ± 0.5 nm (1 σ) with little variation between individual grains.

3.3.4 Fe^{2+} oxidation in sulfate medium

To investigate the possible role of anion adsorption, we examined Fe^{2+} oxidation on polycrystalline platinum in sulfuric acid, as this is a medium in which sulfate anions absorb specifically.[57] It has been suggested previously that sulfate, or other specifically adsorbed anions (such as Cl^- and Br^-), can facilitate Fe^{2+} oxidation by acting as a bridge for electron transfer, or by modifying the electrical double layer.[58] Given that sulfate adsorption on platinum surfaces is facet sensitive,[59,60] one might expect that the activity for Fe^{2+} oxidation could be affected accordingly.

Eight SECCM electrochemical activity maps for the oxidation of 1 mM Fe^{2+} in 10 mM H_2SO_4 were obtained by holding the surface at potentials ranging from 0.75 V to 1.3 V, based on macroscopic CVs (Figure 3.2a). Figures 3.7a and 3.7b show two representative SECCM activity maps at 0.8 and 1.0 V. The corresponding EBSD map for the area imaged with SECCM is shown in Figure 3.7c. From the

EBSD map, it can be seen that most of the grains within the area investigated have a significant contribution of (101) orientation with a fraction of grains with a main contribution from (001) orientation. Although the imaged area does not include all basal planes, some striking features are exhibited. By comparing the EBSD and SECCM maps, it is clearly evident that a correlation exists between structure and activity in sulfuric acid, but it is that the activity of the surface is strongly dominated by grain boundaries, with the grains themselves also having some lower activity. This pattern of activity is in stark contrast with the results in the non-adsorbing perchlorate medium where no enhanced activity was detectable at the boundaries between the crystalline grains.

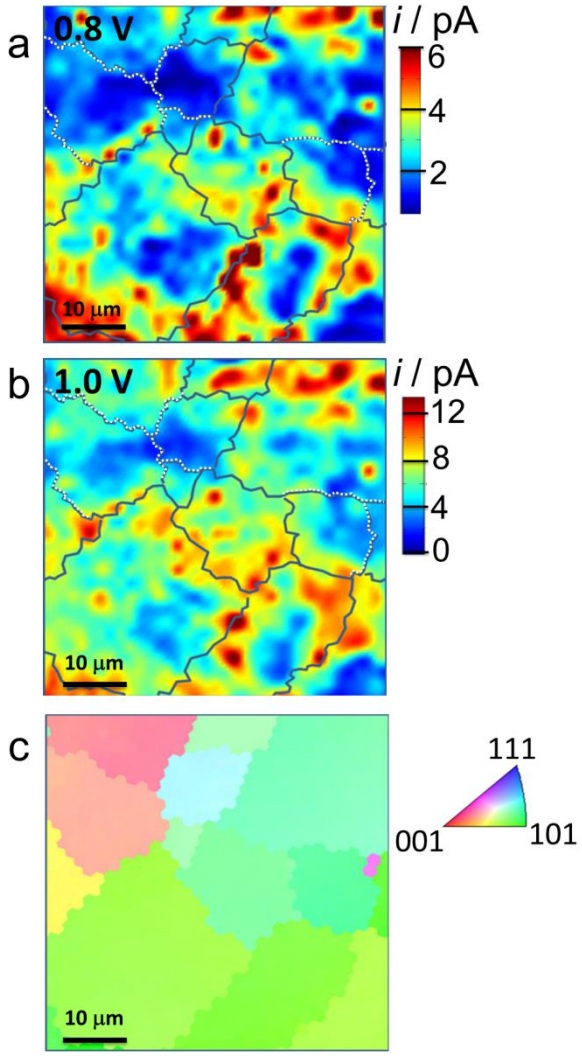

Figure 3.7 SECCM and EBSD images of a polycrystalline platinum electrode for the oxidation of Fe^{2+} in H_2SO_4 (a-b) SECCM images of the oxidation of 1 mM Fe^{2+} to Fe^{3+} in 10 mM H_2SO_4 at 0.8 V and 1.0 V relative to Pd–H_2. Grain boundaries (from EBSD) are marked with either black lines (boundaries at which an enhanced current was observed) or white dotted lines (with no enhanced current) to guide the eye. (c) Corresponding EBSD image and surface orientation of the same area.

Analysis of the AFM images of a polycrystalline Pt foil (section 3.3.5) yields an estimated boundary width of ~ 50 – 100 nm which accounts for roughly 3% of the area encompassed under the 2 μm diameter SECCM probe, yet the variation in currents between grains and grain boundaries are readily detected. This may suggest that the grain boundaries are at least 7 fold more active than the areas within the grain (to achieve an increase of 20 % current) or, alternatively, that the changes in the crystallographic orientation in the proximity of the grain boundary affect the coordination of adsorbed ions due to a break-down of long-range order.

Closer inspection of the maps in Figure 3.7 further highlights that while some grain boundaries exhibit a strongly enhanced activity, this is not generally true of all grain boundaries. Indeed, grain boundaries deduced from the EBSD map, and marked with white dotted lines on the SECCM maps, do not display enhanced activity in any of the eight images at the wide range of potentials covered. These electrochemically 'invisible' boundaries encompass grains closer to the (001) orientation while the more active grain boundaries are those that encompass grains close to the (101) orientation, indicating that there may be an effect of the character of the grain boundary itself.

Cyclic voltammograms of the $Fe^{2+/3+}$ redox reaction in sulfate medium on basal plane single-crystal electrodes (Figure 3.8) show minimal differences in activity between basal planes in the potential region for the oxidation of Fe^{2+}, which is in agreement with our SECCM findings for the areas within the grains, which show more or less similar activities. The differences in peak currents for the single-crystal measurements may be attributed to the variations in oxide formation on different facets which inhibit the oxidation of Fe^{2+}.[40] The important point here, however, is that single-crystal measurements cannot reveal any electrochemical information on

the grain boundaries, emphasizing a key advantage of SECCM for probing the electrochemical response of complex materials at high resolution, in this case the boundaries between crystalline grains.

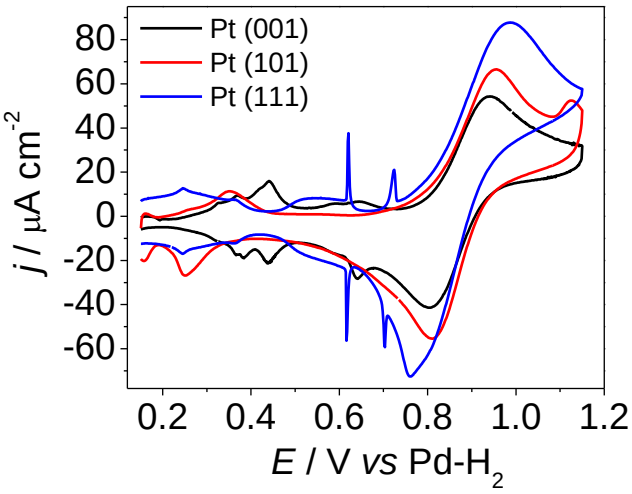

Figure 3.8 Platinum single crystal CVs for the oxidation of Fe^{2+} in H_2SO_4. Cyclic voltammograms of 2 mM $FeSO_4$ in 10 mM H_2SO_4 on : Pt(111) electrode (blue line), Pt(001) electrode (black line) and Pt(101) electrode (red line) vs Pd-H_2. Scan rate was 10 mV s^{-1}.

The differences between the activity of grains and grain boundaries can be seen in the *i-E* plots in Figure 3.9, constructed for these different areas from analysis of images at various potentials. As in the case of perchlorate, the trend of surface current increase with the increase of the potential (driving force) is clearly seen for both grain boundary areas and areas within grains, but grain boundary areas show higher activity at all potentials. These findings highlight clearly that certain grain boundaries exhibit a strongly enhanced activity towards Fe^{2+} oxidation. There are several possible reasons for this. First, following the anion-bridging hypothesis, it may be that the boundaries between crystalline facets provide more sulfate

adsorption sites, depending on the orientation of the neighboring grains, catalyzing the oxidation of Fe^{2+}. Alternatively, and contradictory to the bridging effect, sulfate is known to bind strongly to sites with a long range order, thus the activity on the grains may be largely suppressed due to the site blocking effect of the adsorbing anion. In this case, the grain boundaries, which presumable have a less ordered structure, show relatively enhanced activity as less or no sites are blocked. Unfortunately, we cannot distinguish between these two cases as EBSD cannot provide structural information on the grain boundaries due to the irregular nature. A further understanding of the structure of these boundaries and their role in surface reactivity would be beneficial, not only for Fe^{2+} oxidation, but for other surface dependent reactions as well.

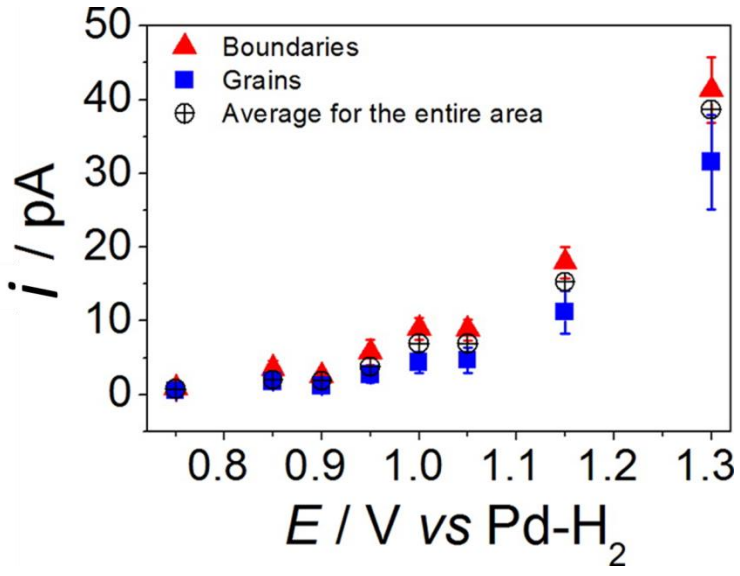

Figure 3.9 *i-E* curves for 1 mM $FeSO_4$ in 10 mM H_2SO_4. The current was obtained by averaging the current from regions of the SECCM images where grain boundaries (▲, red) and regions within the boundaries (■, blue) were identified. Similarly, an *i-E* curve for the average current over the entire scanned region (including all grains and boundaries) is also shown (⊕) for comparison.

An important feature of SECCM is that the facilitated migration current across the meniscus at the end of the tip, between the two QRCEs, also enhances mass transport of charged species to and from the substrate of investigation. The mass transport coefficient for an electrode in SECCM is estimated[45] to be about 10-20 times higher than in macroscale measurements at a scan rate of 10 mVs^{-1} and this leads to a much more drawn out current-voltage response in SECCM (Figure 3.9), enabling surface kinetic effects to be elucidated and visualized. The same effect can be seen for the perchlorate medium on the shape of the wave when inspecting the macroscale CV (Figure 3.2a) and the SECCM constructed *i-E* plot (Figure 3.5a), however the extent in which mass transport increases in the SECCM setup for the two electrolyte systems is not necessarily the same. In particular, the SECCM assisted mass transport rate depends on the charge of the species in solution and on the magnitude of the migration current. Thus, when comparing the SECCM results for perchlorate and sulfate media, variations in mass transport of the systems and Fe^{2+} concentration (1 mM and 2 mM for the sulfate and perchlorate, respectively) need to be taken into consideration. The average current in the mass transport limited regime in perchlorate is roughly four times higher than observed in sulfate medium (Figures 3.5a and 3.9, respectively), and half this difference is due to the concentration effect. The remaining difference can be accounted for differences in effective mass transport coefficients which depend on the magnitude of the charge on the species, and on the concentration of charged species, influenced by ion pairing, as well as the potential bias between the QRCEs. In the sulfate medium, the dominant species is of the type $FeHSO_4^+$ (with some Fe^{2+}, $FeSO_4$ and $FeH_2SO_4^-$) and hence reduces the magnitude of charged species in respect to the perchlorate medium.[61,62] Therefore, it is difficult to directly quantitatively compare the SECCM

results of the two electrolyte systems and when these factors are taken into consideration there might be little difference between the overall (average) activities for Fe^{2+} oxidation in the perchlorate and sulfate media. On the other hand, it is apparent that there are significant variations in local activity for the $Fe^{2+/3+}$ couple in the two media at polycrystalline platinum, that are readily revealed by SECCM. Unique reactivity patterns have been revealed that depend greatly on the type of anion in solution.

3.3.5 AFM images of a Pt foil

In order to exclude that surface currents observed in the SECCM images are due to changes in wettability of the scanning droplet across the grains, we have analyzed the surface roughness of the Pt foil, used in the study, with AFM. A typical AFM image of the platinum foil used in this study is shown in Figure 3.10. The average roughness across the surface (R_a) is 5.5 ± 0.5 nm (1 σ) with negligible difference of surface roughness among different grains. Further analysis of the image in yields an estimated grain boundary width of ~50 nm which was used to calculate the estimated percentage of contact area of the droplet with the surface.

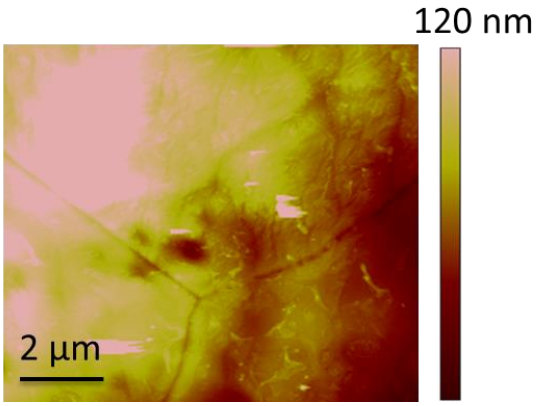

Figure 3.10 AFM image of a platinum foil containing three grains and grain boundaries average roughness across the surface (Ra) is 5.5 ± 0.5 nm (1 σ) with negligible difference of surface roughness among different grains

3.3.6 SECCM image of $FcTMA^+$ oxidation in sulfuric acid electrolyte

In order to further investigate the possibility of droplet size variance during the SECCM scan, a control image was recorded on the polycrystalline Pt foil for the outersphere redox mediator (ferrocenylmethyl)trimethylammonium ($FcTMA^+$) where we expected no electrochemical variation across the sample and therefore could distinguish clearly between variation attributed to droplet size effects and variations attributed to the electrochemical behavior.

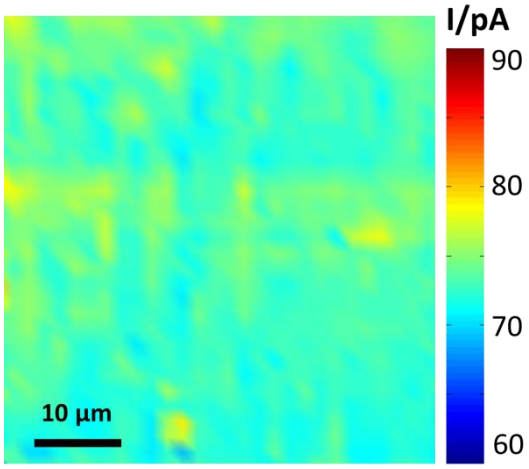

Figure 3.11 SECCM image of the oxidation of 1 mM $FcTMA^+$ in 10 mM H_2SO_4 held at a potential of + 0.8 V relative to Pd-H_2.

We consider the oxidation of 1 mM $FcTMA^+$ which is often used as a classical outer sphere electron transfer reaction in electrochemical studies. The potential for which the surface was held at, in respect to the scanning probe, in this SECCM control experiment was determined from CV measurements where the oxidation wave of $FcTMA^+$ was mass transport limited. Figure 3.8 shows a typical SECCM image of $FcTMA^+$ oxidation on a polycrystalline platinum foil with a scanning probe of the same dimensions used for the Fe^{2+} oxidation studies (~ 2µm

diameter). It can be seen that the surface is uniformly active (average of 75 pA), with small variations (< 3 pA, corresponding to 4% of the average current). Particularly, there are no structure dependent features, indicating little influence of the potential wetting variations even if a reaction is taking place on the surface.

3.4 Conclusions

Conventional macroscopic electrochemical measurements at polycrystalline metal electrodes, such as platinum, have tended to implicitly assume a uniformly active surface. The studies presented herein show that this is not a reasonable assumption for polycrystalline platinum, at least for the model $Fe^{2+/3+}$ system. Indeed, considering heterogeneous electron transfer (ET) rates to be uniform across a polycrystalline surface may not only lead to misinterpretation of kinetic data, but also ignores subtle electrode structure effects which are essential to gaining a deeper understanding of fundamental electrochemical processes. Such effects are readily revealed by SECCM, which provides a powerful approach for visualizing electrode activity.

By comparing the activity of individual grains, deduced by SECCM, to grain structure from EBSD images, we have found that the electrochemical oxidation of Fe^{2+} is sensitive to the platinum surface orientation, regardless of the supporting electrolyte. Moreover, we have established that grain boundaries can play an important role in this rather complex electrochemical process.

The main features of the SECCM technique in the present application are that: (i) it allows 'pseudo'-single-crystal experiments (in individual grains of a polycrystalline sample with high index facets and grain boundaries) owing to the spatial confinement of the electrochemical cell; (ii) it allows access to fast surface

kinetics owing to the higher mass transport rates generated; and (iii) it enhances the resolution of competing processes (such as surface oxidation) with the ability to fine-tune the time regime in which measurements are made. Thus, Fe^{2+} oxidation in perchlorate medium was found to exhibit variations in rate (current) depending on the crystallographic orientation of the microcrystalline grain, with a trend that could be rationalized based on cyclic voltammograms obtained on basal plane (low index) single-crystal electrodes. In contrast, in sulfate medium, boundaries between grains exhibited higher reactivity compared to the areas within grains. Similar electrochemical characteristics were seen within grains of different orientation, qualitatively consistent with cyclic voltammograms on basal plane single-crystal electrodes, which showed little variation in activity between basal planes (albeit at much lower mass transport rates).

The studies herein provide a platform for further investigation of polycrystalline electrode materials, particularly for those of electrocatalytic relevance. More generally, the data presented have major implications for the investigation and analysis of electrochemical processes by macroscopic techniques, which evidently average the reactivity over many different types of surface sites. SECCM provides a means of probing individual sites effectively and unambiguously.

3.5 References

(1) Bard, A. J. *J. Am. Chem. Soc.* **2010**, *132*, 7559.

(2) Somorjai, G. A. *Science* **1985**, *227*, 902.

(3) Marković, N. M.; Ross Jr, P. N. *Surf. Sci. Rep.* **2002**, *45*, 117.

(4) *Fuel Cell Catalysis: A Surface Science Approach*; Wiley: Hoboken, NJ, 2009.

(5) Kato, H.; Asakura, K.; Kudo, A. *J. Am. Chem. Soc.* **2003**, *125*, 3082.

(6) Arico, A. S.; Bruce, P.; Scrosati, B.; Tarascon, J.-M.; van Schalkwijk, W. *Nat. Mater.* **2005**, *4*, 366.

(7) Lee, S. W.; Chen, S.; Suntivich, J.; Sasaki, K.; Adzic, R. R.; Shao-Horn, Y. *J. Phys. Chem. Lett.* **2010**, *1*, 1316.

(8) Couper, A. M.; Pletcher, D.; Walsh, F. C. *Chem. Rev.* **1990**, *90*, 837.

(9) Lee, I.; Morales, R.; Albiter, M. A.; Zaera, F. *Proc. Natl. Acad. Sci. U. S. A.* **2008**, *105*, 15241.

(10) Sherigara, B. S.; Kutner, W.; D'Souza, F. *Electroanalysis* **2003**, *15*, 753.

(11) Rabis, A.; Rodriguez, P.; Schmidt, T. J. *ACS Catalysis* **2012**, *2*, 864.

(12) Antolini, E. *Energy Environ. Sci.* **2009**, *2*, 915.

(13) Climent, V.; Feliu, J. M. *J. Solid State Electrochem.* **2011**, *15*, 1297.

(14) Koper, M. T. M. *Nanoscale* **2011**, *3*, 2054.

(15) Cherstiouk, O. V.; Gavrilov, A. N.; Plyasova, L. M.; Molina, I. Y.; Tsirlina, G. A.; Savinova, E. R. *J. Solid State Electrochem.* **2008**, *12*, 497.

(16) Maillard, F.; Savinova, E. R.; Stimming, U. *J. Electroanal. Chem.* **2007**, *599*, 221.

(17) König, U.; Davepon, B. *Electrochim. Acta* **2001**, *47*, 149.

(18) Schultze, J. W.; Pilaski, M.; Lohrengel, M. M.; Konig, U. *Faraday Discuss.* **2002**, *121*, 211.

(19) Dudin, P. V.; Snowden, M. E.; Macpherson, J. V.; Unwin, P. R. *ACS Nano* **2011**, *5*, 10017.

(20) Heller, I.; Kong, J.; Heering, H. A.; Williams, K. A.; Lemay, S. G.; Dekker, C. *Nano Lett.* **2004**, *5*, 137.

(21) Patten, H. V.; Lai, S. C. S.; Macpherson, J. V.; Unwin, P. R. *Anal. Chem.* **2012**, *84*, 5427.

(22) Day, T. M.; Unwin, P. R.; Macpherson, J. V. *Nano Lett.* **2006**, *7*, 51.

(23) Williams, C. G.; Edwards, M. A.; Colley, A. L.; Macpherson, J. V.; Unwin, P. R. *Anal. Chem.* **2009**, *81*, 2486.

(24) Mirkin, M. V.; Nogala, W.; Velmurugan, J.; Wang, Y. *Phys. Chem. Chem. Phys.* **2011**, *13*, 21196.

(25) Wittstock, G.; Burchardt, M.; Pust, S. E.; Shen, Y.; Zhao, C. *Angew. Chem. Int. Ed.* **2007**, *46*, 1584.

(26) Patten, H. V.; Meadows, K. E.; Hutton, L. A.; Iacobini, J. G.; Battistel, D.; McKelvey, K.; Colburn, A. W.; Newton, M. E.; Macpherson, J. V.; Unwin, P. R. *Angew. Chem. Int. Ed.* **2012**, *51*, 7002.

(27) Amemiya, S.; Bard, A. J.; Fan, F.-R. F.; Mirkin, M. V.; Unwin, P. R. *Annu. Rev. Anal. Chem.* **2008**, *1*, 95.

(28) Basame, S. B.; White, H. S. *J. Phys. Chem.* **1995**, *99*, 16430.

(29) Bath, B. D.; Lee, R. D.; White, H. S.; Scott, E. R. *Anal. Chem.* **1998**, *70*, 1047.

(30) Albery, J. *Electrode Kinetics*; Oxford University Press, June 5, 1975.

(31) McCreery, R. L. *Chem. Rev.* **2008**, *108*, 2646.

(32) Chen, P.; Fryling, M. A.; McCreery, R. L. *Anal. Chem.* **1995**, *67*, 3115.

(33) Samec, Z. *J. Electrochem. Soc.* **1999**, *146*, 3349.

(34) Nagy, Z.; Curtiss, L. A.; Hung, N. C.; Zurawski, D. J.; Yonco, R. M. *J. Electroanal. Chem.* **1992**, *325*, 313.

(35) Fawcett, W. R. *Electrochim. Acta* **1997**, *42*, 833.

(36) Fawcett, W. R.; Fedurco, M.; Kováčová, Z. *J. Electrochem. Soc.* **1994**, *141*, L30.

(37) Hromadova, M.; Fawcett, W. R. *J. Phys. Chem. A* **2001**, *105*, 104.

(38) Bochmann, H. G.; Vielstich, W. *Electrochim. Acta* **1988**, *33*, 805.

(39) Rodriguez-Lopez, J.; Bard, A. J. *J. Am. Chem. Soc.* **2010**, *132*, 5121.

(40) Rodríguez-López, J.; Minguzzi, A.; Bard, A. J. *J. Phys. Chem. C* **2010**, *114*, 18645.

(41) Angerstein-Kozlowska, H.; Conway, B. E.; Sharp, W. B. A. *J. Electroanal. Chem.* **1973**, *43*, 9.

(42) Schouten, K. J. P.; van der Niet, M. J. T. C.; Koper, M. T. M. *Phys. Chem. Chem. Phys.* **2010**, *12*, 15217.

(43) Imai, H.; Izumi, K.; Matsumoto, M.; Kubo, Y.; Kato, K.; Imai, Y. *J. Am. Chem. Soc.* **2009**, *131*, 6293.

(44) Ebejer, N.; Schnippering, M.; Colburn, A. W.; Edwards, M. A.; Unwin, P. R. *Anal. Chem.* **2010**, *82*, 9141.

(45) Snowden, M. E.; Güell, A. G.; Lai, S. C. S.; McKelvey, K.; Ebejer, N.; O'Connell, M. A.; Colburn, A. W.; Unwin, P. R. *Anal. Chem.* **2012**, *84*, 2483.

(46) Lai, S. C. S.; Patel, A. N.; McKelvey, K.; Unwin, P. R. *Angew. Chem. Int. Ed.* **2012**, *51*, 5405.

(47) Miller, T. S.; Ebejer, N.; Güell, A. G.; Macpherson, J. V.; Unwin, P. R. *Chem. Commun.* **2012**, *48*, 7435.

(48) Güell, A. G.; Ebejer, N.; Snowden, M. E.; McKelvey, K.; Macpherson, J. V.; Unwin, P. R. *Proc. Natl. Acad. Sci. U. S. A.* **2012**, *109*, 11487.

(49) Lai, S. C. S.; Dudin, P. V.; Macpherson, J. V.; Unwin, P. R. *J. Am. Chem. Soc.* **2011**, *133*, 10744.

(50) Güell, A. G.; Ebejer, N.; Snowden, M. E.; Macpherson, J. V.; Unwin, P. R. *J. Am. Chem. Soc.* **2012**, *134*, 7258.

(51) Clavilier, J.; Armand, D.; Sun, S. G.; Petit, M. *J. Electroanal. Chem.* **1986**, *205*, 267.

(52) Vasile, M. J.; Enke, C. G. *J. Electrochem. Soc.* **1965**, *112*, 865.

(53) Inzelt, G.; Berkes, B. B.; Kriston, Á. *Pure Appl. Chem.* **2011**, *83*, 269.

(54) Garcia-Araez, N.; Climent, V.; Feliu, J. *J. Phys. Chem. C* **2009**, *113*, 9290.

(55) Bockris, J. O. M.; Mannan, R. J.; Damjanovic, A. *J. Chem. Phys.* **1968**, *48*, 1898.

(56) Łosiewicz, B.; Jurczakowski, R.; Lasia, A. *Electrochim. Acta* **2012**, *80*, 292.

(57) Kunimatsu, K.; Samant, M. G.; Seki, H. *J. Electroanal. Chem.* **1989**, *258*, 163.

(58) Johnson, D. C.; Resnick, E. W. *Anal. Chem.* **1977**, *49*, 1918.

(59) Nart, F. C.; Iwasita, T.; Weber, M. *Electrochim. Acta* **1994**, *39*, 2093.

(60) Mostany, J.; Herrero, E.; Feliu, J. M.; Lipkowski, J. *J. Phys. Chem. B* **2002**, *106*, 12787.

(61) Gil, A. F.; Salgado, L.; Galicia, L.; González, I. *Talanta* **1995**, *42*, 407.

(62) Sutton, J. *Nature* **1952**, *169*, 71.

Chapter 4 Spatially Resolved Electrochemistry in Ionic Liquids: Surface Structure Effects on Triiodide Reduction at Platinum Electrodes

Abstract

Understanding the relationship between electrochemical activity and electrode structure is vital for improving the efficiency of dye-sensitized solar cells. Here, the reduction of triiodide to iodide in 1-butyl-3-methylimidazolium tetrafluoroborate ([BMIm][BF_4]) room temperature ionic liquid (RTIL) is investigated on polycrystalline platinum using scanning electrochemical cell microscopy (SECCM) and correlated to the crystallographic orientation from electron backscatter diffraction (EBSD). Although the rate determining step in all grains was the first electron transfer, significant grain-dependent variations in activity were revealed, with grains with a dominant (110) crystallographic character exhibiting higher catalytic activity compared to those with a major (100) orientation. The SECCM technique is demonstrated to resolve heterogeneity in activity, highlighting that methods incorporating polycrystalline electrodes miss vital details for understanding and optimizing electrocatalysts. An additional advantage of the SECCM over single crystal techniques is its ability to probe high index facets.

4.1 Introduction

Dye sensitized solar cells (DSSCs) have attracted widespread attention as a low cost alternative to conventional solar cells since the seminal report by O'Regan and Grätzel in the early 90s.[1,2] Typically, a DSSC consists of a dye-sensitized TiO_2

photo-electrode and a platinum counter electrode (CE) that sandwich an organic electrolyte solution containing a redox shuttle. The processes at the sensitized electrode are photo-excitation and electron injection followed by oxidation of the dye. The oxidized form of the dye is then regenerated by the redox shuttle, which is reduced at the CE. Although alternatives to platinum as the CE material[3] and the triiodide (I_3^-) / iodide (I^-) redox couple[4] as the mediator have been suggested, these remain the most common components.[5] However, compared to other processes occurring in DSSCs, there are relatively few mechanistic studies of the reduction of I_3^- to I^- at platinum in various media.[6-9] In this chapter, the rate of this reaction in room temperature ionic liquids (RTILs) is shown to be strongly influenced by the local structure of the Pt electrodes and identify the optimal surface for electrocatalysis.

DSSCs typically employ acetonitrile[2] as the organic electrolyte, but there is now considerable interest in using RTILs[10,11] owing to their low vapor pressure, high stability, low toxicity and wide potential window. Although there have been previous macroscale studies on the I_3^-/I^- redox couple at polycrystalline Pt electrodes in RTILs,[8,12] such studies prevent an understanding of structural and dimensional effects that may significantly influence electrocatalytic activity.[13-17] This is particularly important for the process of I_3^- reduction at Pt, since strong dependences of the kinetics on the size and morphology of Pt particles have been reported in acetonitrile.[18-20] As photoelectrodes become more efficient, there will be a need to ensure that cell efficiencies do not become limited by CE processes.

Here we show how SECCM[21,22] can be used to image electrode reaction rates in RTILs that are correlated with local electrode structure (via EBSD). This represents a major new environment for SECCM which has, hitherto, been used only

for aqueous electrolyte/electrode interfaces, albeit with some success.[13,23] RTILs have generally proven challenging for probe imaging techniques, due to the high viscosity and (for electrochemical probe methods) low (and widely different) diffusion coefficients of redox species.[24-26] In contrast, we have found that RTILs can be used readily for SECCM.

4.2 Experimental

4.2.1 Solutions

The RTIL used, was 1-butyl-3-methylimidazolium tetrafluoroborate ([BMIm][BF_4]) and was used fresh without further treatment. The 10 mM I_3^- solution was prepared by dissolving equimolar amounts of I_2 and tetrabutylammonium iodide (TBAI) in the RTIL, leaving the solution in a sealed vial in an ultrasonic bath for 2 hrs. See Table 2.1 in section 2.1 for list of chemicals, purity and suppliers.

4.2.2 SECCM setup

A schematic of the SECCM setup for the work herein is shown in Figure 4.1. The SECCM tip and sample were deployed in a custom-built environmental chamber (section 2.2.2) in which dry nitrogen gas (N_2) was flowed to facilitate the removal of dissolved oxygen as well as to assist in drying of the droplet at the end of the probe.[27] The dual barrel glass capillary was pulled to 1.6 μm in diameter and filled with a solution of interest (10 mM triiodide solution in RTIL). Both barrels of the SECCM tip were filled quickly with the RTIL solution using a nonmetallic syringe needle (MicroFil). Ag wire, rinsed with water and then ethanol, followed by drying

under a nitrogen flow was used as QRCEs. An oscillation amplitude of ~ 200 nm peak to peak was applied to the probe in the *z* direction, leading to an alternating current component (i_{ac}) of the ionic conductance signal, i_{dc}, due to the periodical compression and expansion of the meniscus at the end of the pipette while in contact with the surface.

4.2.3 Working electrode

The substrate of interest, polycrystalline platinum foil, was flame-annealed prior to experiments and connected as a working electrode (WE) with an area defined by the size of the meniscus contact (roughly the size of the pipette, corresponding to ~ 2-3 × 10^{-8} cm^2).

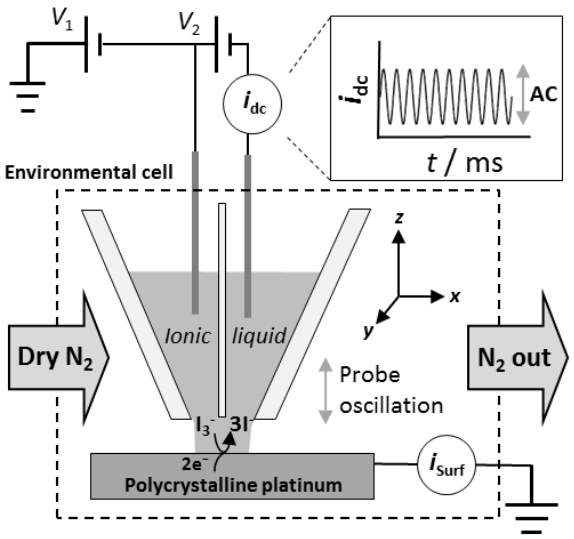

Figure 4.1 Schematic of the SECCM setup for RTIL, employing a dual barrel glass pipette pulled to a fine tip (1.6 μm diameter). A bias potential (V_2) of + 0.2 V was applied between two Ag QRCEs and the conductance current (i_{dc}) was monitored to provide positional feedback (normal to the surface). The working electrode potential ($V_{Surf} = -V_1 - V_2/2$)) was varied by changing V_1 and the resulting surface current (i_{Surf}) was recorded.

4.2.4 SECCM scanning parameters and data acquisition

The imaging process consisted of the pipette moving in a series of 20 bilateral line scans in the *xy* plane of the sample, while a sinusoidal oscillation (200 nm peak to peak amplitude, 122 Hz) was applied to the *z* position of the tip (normal to the platinum foil sample). Each line scan was collected by moving the probe meniscus 60 μm in the *x* axis while keeping the *y* position fixed and applying the desired working electrode potential. The probe meniscus then retraced the same line while applying a second (different) working electrode potential. At the end of each bilateral line scan the probe was moved 3 μm in the *y* direction to the start of the next bilateral line scan. In this way, two images at different electrode potentials were obtained. A bias potential of 0.2 V was applied between the QRCEs, leading to a constant migration current (i_{dc}) of *ca.* 3 nA. The oscillation of the tip in the *z* direction generates an AC modulation in the conductance current (i_{ac}, in section 1.2.2) due to the change of droplet geometry and hence a change in ohmic resistance at the end of the tip. The AC amplitude was used as a set-point to ensure a constant tip to substrate separation (meniscus thickness) during scanning. The pipette scan rate was 0.5 μm·s^{-1} and each data point represents an average of 512 acquisition samples of a 50 μs acquisition period per sample, corresponding to 4687 data points per line scan or a data point every 12 nm in the *x* direction. The scan rate corresponded to a residence time of 3 seconds per exposed area tip area (60 µm line scan at 0. 5 μm·s^{-1} with a 1.6 µm diameter probe), which allows sufficient time to develop a steady-state surface current.

The sequence of electrode potentials in the SECCM scan reported in the text was set to: 450 mV, 300 mV, 400 mV and finally 350 mV to ensure that the current

response between different images eliminated any possible time effects. The images presented are representative of several areas of the platinum surface investigated.

4.2.5 EBSD

For the EBSD setup see section 2.3. In the work herein, EBSD images were constructed from diffraction patterns recorded every 1 μm.

4.3 Results and discussion

At relatively low concentrations, triiodide (I_3^-) is formed through the equilibrium between iodine (I_2) and iodide (I^-), which lies to the right in organic solvents and ionic liquids. The redox reactions of interest herein are:[7]

$$3\ I_2 + 2\ e^- \leftrightarrows\ 2\ I_3^- \qquad (4.1)$$

$$I_3^- + 2\ e^- \leftrightarrows 3\ I^- \qquad (4.2)$$

Reaction 4.2 has been described to proceed via a complex mechanism in both acetonitrile[7] and in RTILs[28] but there is some consensus[13-15,29] that the reaction may proceed on platinum via:

$$I_{3(sol)}^- \leftrightarrows I_{2(sol)} + I^- \qquad (4.3)$$

$$I_{2(sol)} + 2\ * \leftrightarrows 2\ I^* \qquad (4.3)$$

$$2\ I^* + 2\ e^- \leftrightarrows 2\ I^- \qquad (4.5)$$

where * denotes the free site on the electrode surface, I* denotes an adsorbed I atom and sol denotes the solution phase.

4.3.1 SECCM cyclic voltammetry (CV)

CVs were recorded in the SECCM setup (meniscus contact) and a typical CV is shown in Figure 4.2. Starting at + 0.6 V *vs.* Ag QRCE and sweeping in the cathodic direction, the reduction of I_3^- is observed with an apparent onset potential of + 0.5 V. Changing sweep direction at - 0.1 V, I^- is oxidized back to I_3^- and starting at + 0.65 V , I_3^- is further oxidized to form I_2. The CV in the SECCM setup is characterized by relatively fast mass transport rates, such that interfacial kinetic effects are manifested in the CVs (*vide infra*).

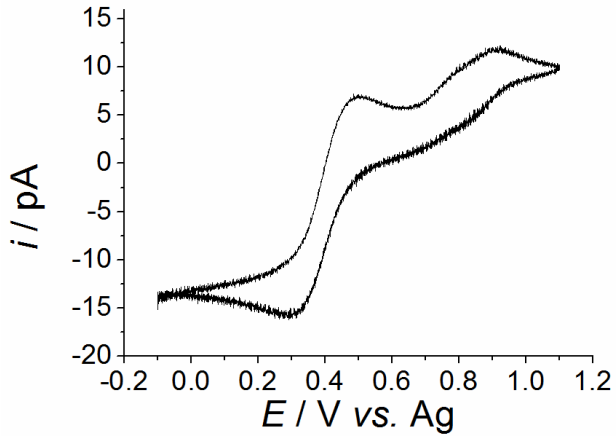

Figure 4.2 SECCM cyclic voltammogram of 10 mM I_3^- in [BMIm][PF_4] on polycrystalline platinum foil. Scan rate of 100 mV s^{-1}.

To estimate the formal potential for reaction 2 in [BMIm][BF_4], macroscale CVs were recorded, yielding an apparent formal potential of + 0.51 (± 0.03) V vs. AgQRE at low potential sweep rates, consistent with values in the literature.[9] This value was confirmed by open circuit potential measurements of equimolar concentrations of I_3^- and I^- in [BMIm][BF_4]

4.3.2 Macroscale measurements

In order to determine the formal potential for the reduction of I_3^-, macroscale CVs were recorded at increasing scan rates on the same platinum foil sample used in the SECCM study. Solutions of 10 mM I_3^- were prepared by dissolving $TBAI_3$ (Sigma Aldrich, ≥ 98 % purity) in [BMIm][BF_4]. The solutions were placed in an ultrasonic bath for 1 hr and alumina base (aluminium oxide, Fischer Scietific) was inserted in the solution vessel to adsorb remaining water. A fresh droplet for each CV scan (to minimize adsorption of water from the atmosphere) of 6 μL was placed on the WE (platinum foil) creating a contact area of 0.22 cm^2 (measured accurately with a Vernier caliper). Finally, an Ag wire as a quasi-reference electrode and a platinum wire as a counter electrode were inserted into the droplet to complete the electrochemical cell. CVs were recorded over the potential range of I_3^- reduction at scan rates of: 0.5, 2, 3, 5, 10, 20, 40, 60 and 80 $mV \cdot s^{-1}$ and are shown in Figure 4.3.

The formal potential, $E^{0'}$ for the reaction was estimated as the average peak potential for the reduction and oxidation waves from the voltammograms at scan rates of 0.5 to 3 $mV \cdot s^{-1}$, taking in account the differences in diffusion coefficients ($E^{0'}$ = + 0.51 ± 0.02 V vs. Ag QRE). The formal potential was further verified by directly measuring the open circuit voltage of a solution containing equimolar concentrations (10 mM) of I_3^- and I^- in [BMIm][BF_4] vs. Ag ($E^{0'}$ = 0.51 ± 0.01 V vs. Ag QRE).

The peak to peak separation increases from about 60 mV, at a scan rate of 0.5 $mV \cdot s^{-1}$ to 140 mV at a scan rate of 80 $mV \cdot s^{-1}$, showing quasi-reversible behavior starting from scan rates faster than 3 $mV \cdot s^{-1}$, in agreement with similar studies in [BMIm][NTf_2][8] and [BMIm][BF_4].[9] However, extracting fundamental kinetic

parameters, such as HET constants are complicated by issues like ohmic drop due to limited electrolyte conductivity and limited knowledge of the complex reaction mechanism.[8,28,30,31] Such problems do not occur for SECCM measurements as mentioned above.

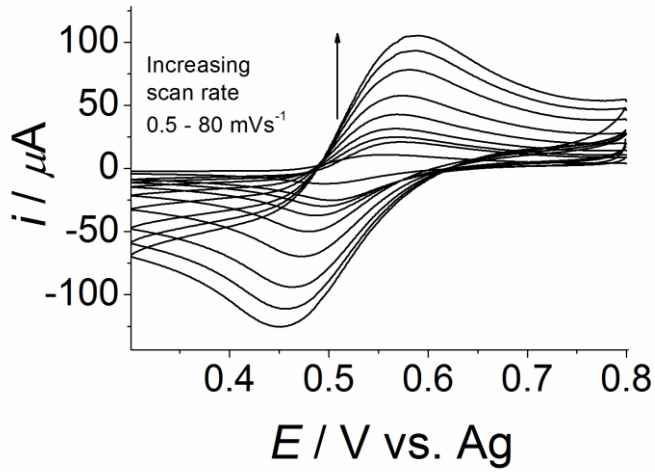

Figure 4.3 – Macroscale CVs of 10 mM $TBAI_3^-$ in [BMIm][BF_4] on polycrystalline platinum foil at scan rates of: 0.5, 2, 3, 5, 10, 20, 40, 60, and 80 $mV \cdot s^{-1}$. The working electrode area is 0.22 cm^2.

4.3.3 SECCM imaging of triiodide reduction on platinum foil

SECCM images (Figure 4.4) were acquired at different electrode potentials for the I^-/I_3^- process, ranging between + 0.45 V and + 0.30 V. The pipette scan rate was set so that a characteristic residence time (meniscus diameter/pipette scan rate) of 3 seconds was achieved, ensuring that a steady-state response was established (see section 4.2.3). As depicted in Figures 4.4a – 4.4d, the average (steady-state)

reduction current increases from *ca.* 1.5 pA at + 0.45 V to *ca.* 12 pA at + 0.30 V, in good agreement with the reduction wave in the CV in Figure 4.2 (taking in account its transient nature). Notably, significant variations in surface current are observed across the SECCM images, with the current changing by more than a factor of two between well-defined regions of low and high activity. A crystallographic orientation map of the same area, obtained with EBSD (Figure 4.4e), reveals a strong correlation between individual crystallographic grains and the variations in the SECCM surface current maps, highlighting significant electrode structural dependency of the kinetics of the I^-/I_3^- process.

SECCM acquires other maps simultaneously with the surface current image: topography, direct current (DC) conductance and the AC component of the conductance current between the barrels in the probe (Figure 4.1),[21] used as a feedback parameter to maintain a constant tip-substrate separation (meniscus height) throughout a scan.[22] The DC and AC components of the conductance current are highly sensitive to changes in wetting and droplet shape.[21,22,32] A typical AC amplitude map (set-point value of 20 pA), shown in Figure 4.4f, verifies the stability of the RTIL meniscus droplet during the SECCM scan. Most importantly, this stability indicates that the electrochemical variations seen in Figures 4.4a – 4.4d are not due to a change in droplet size and are essentially due to variations in inherent activity. However, in proximity to grain boundaries there appear to be some small perturbation of the droplet, leading to a change in the AC value that can be used to highlight the granular structure of the sample (Figure 4.4f and Figure 4.4a). This effect verifies the spatial correlation found between the SECCM images and EBSD map, as grain boundaries are highlighted by both imaging techniques and can be used as a means of self-referencing between images as well as to provide a precise

estimate for the meniscus size (Figure 4.4b). In addition, we have previously shown, using atomic force microscopy (AFM) that there is similar roughness of individual grains on such polycrystalline platinum foils[13] excluding the possibility of significant differences in wetting between individual grains.

A key feature of SECCM is that we can estimate the magnitude of any ohmic drop via the conductance current between the two QRCEs. This is gained from analysis of the DC conductance current maps, such as the example shown in Figure 4.5a. The DC conductance maps, exhibited a steady DC of *ca.* 3 nA (corresponding to a resistance at the tip of *ca.* 66 MΩ for a bias potential of +0.2 V) throughout the scan with minute (but detectable) variations at grain boundaries. The ohmic drop (*i*R) associated with the tip resistance during scanning is negligible and accounts for less than a 1 mV when calculated for the highest currents observed (~ - 14 pA in Figure 4.4d), highlighting the strength of the SECCM technique over macroscopic measurements.

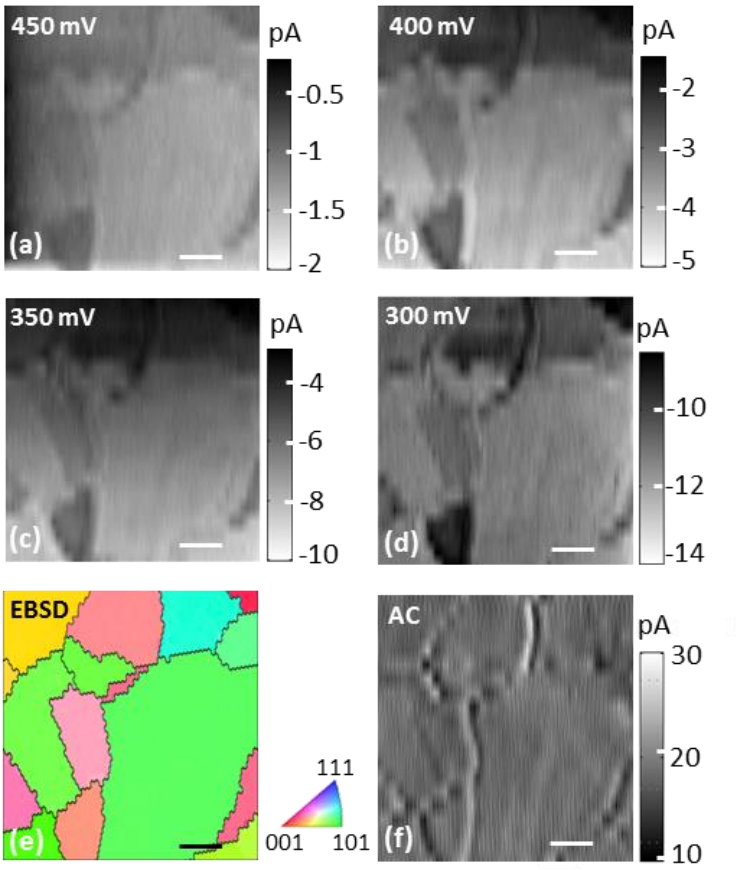

Figure 4.4 SECCM and EBSD maps of a Pt electrode for the reduction of I_3^- in [BMIm][BF_4]. (a) – (d) Spatially resolved surface currents for the reduction of 10 mM I_3^- in [BMIm][BF_4] at 450, 400, 350 and 300 mV *vs.* Ag QRCE, respectively. (e) EBSD image of the scanned area, black lines between grains are to guide the eye. (f) Typical AC amplitude ion conductance map during the scan at 400 mV (illustrating the general uniformity of the AC feedback over grains, while highlighting grain boundaries). Scale bar in all images is 10 μm.

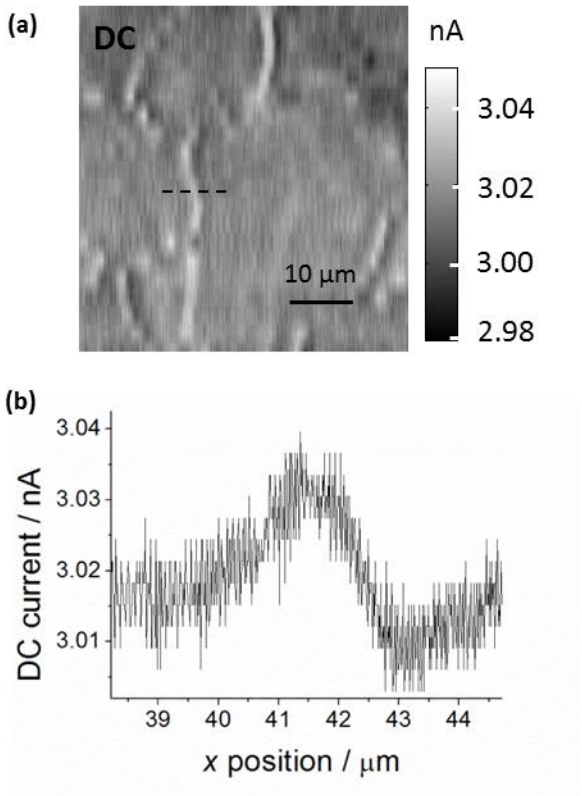

Figure 4.5 – SECCM DC conductance map at an electrode potential of + 0.4 V**.** (a) Typical DC conductance map in the SECCM setup exhibiting highly stable values around 3 nA. The bias voltage between the QRCEs was + 0.2 V. (b) Cross section of the dotted line in (a) where the meniscus contact area was estimated as < 3 µm in diameter (*i.e.* of the order of the probe size) where the DC was perturbed the most (at grain boundaries, shown in Figure 3(e)).

Inspection of the EBSD image (Figure 4.4e) and surface electrochemical images (Figures 4.4a – 4.4d) indicates that individual grains with a high contribution of the (110) orientation correlate to higher reduction currents at all potentials, whereas grains with a high contribution of the (100) orientation lead to lower reduction currents. The latter observation is in agreement with recent studies of hydrogen oxidation on basal plane Pt electrodes in RTILs,[33] where the surface adsorption of the anion ($[BF_4^-]$) was considered to possibly impede electrocatalysis.

The decreased activity for less compact surfaces (Pt (100)) was related to the stronger anion adsorption compared to more densely packed crystalline planes, Pt (110) and Pt (111). Similar trends in activity have been observed in preferentially-shaped nanoparticles in acetonitrile.[19]

4.3.4 Tafel analysis of SECCM images

To give a qualitative comparison of the variations in activity between grains, effective exchange current densities (j^0) were calculated. A Tafel analysis of the four SECCM images in Figure 4.4 was performed yielding values of spatially-resolved j^0 values and apparent Tafel slopes for the scanned area of the Pt foil.

In proximity to the half-wave potential, the currents measured through the working electrode (WE) are affected by both mass transport and electrode kinetics. In order to extract kinetics from the SECCM images, the kinetic component must be separated from that due to mass transport. Since the mass transport component of the total measured current density is independent of applied electrode potential, the current density due to electrode kinetics alone can be expressed as:

$$\frac{1}{j_T(E)} = \frac{1}{j_k(E)} + \frac{1}{j_{MT}} \qquad (4.6)$$

$$j_k(E) = \frac{j_T(E)\, j_{MT}}{j_{MT} - j_T(E)} \qquad (4.7)$$

where E is the applied potential V, j_T is the total measured current density, calculated as the measured current at each point in an SECCM electrochemical image, divided by the droplet contact area, as estimated by FE-SEM images of the probe (2.3×10^{-8} cm^2) and confirmed from the DC maps shown in Figure 4.5 (in the grain boundary region), j_k is the potential-dependent kinetic current density and j_{MT} is the potential-

independent current density due to mass transport which is obtained from the limiting current density, in Figure 4.2 (-6.0×10^{-4} $A \cdot cm^{-2}$) for the reduction wave in CV experiments.

The SECCM images recorded at the four different potentials were used to extract kinetics for each data point in a set of images using the relationship:

$$\log(j_K(\eta)) = \log j_0 + \frac{1}{s}(\eta) \qquad (4.8)$$

where η ($\eta = E - E^{0'}$) is the overpotential in V, where the effective $E^{0'}$ ($E^{0'} = +0.512$ V vs. Ag) was obtained from low scan rate macroscopic CVs (see Figure 4.3) and s is the Tafel slope in V per decade.[34]

A linear regression method was used to fit the four potential-dependent data points at each spatial point in the *xy* plane of the SECCM image (comprising 4687 points) to a linear curve as postulated in Equation 4.6 and the intercept ($\log(j^0)$) and Tafel slope (s) were extracted. Spatially resolved goodness of fit (R^2 value) and the standard errors in Tafel slopes are shown in Figures 4.6a and 4.6b, respectively. A typical plot of $\log(j_K)$ versus the overpotential η is shown in Figure 4.6c (in this case, a random point at the center of the image).

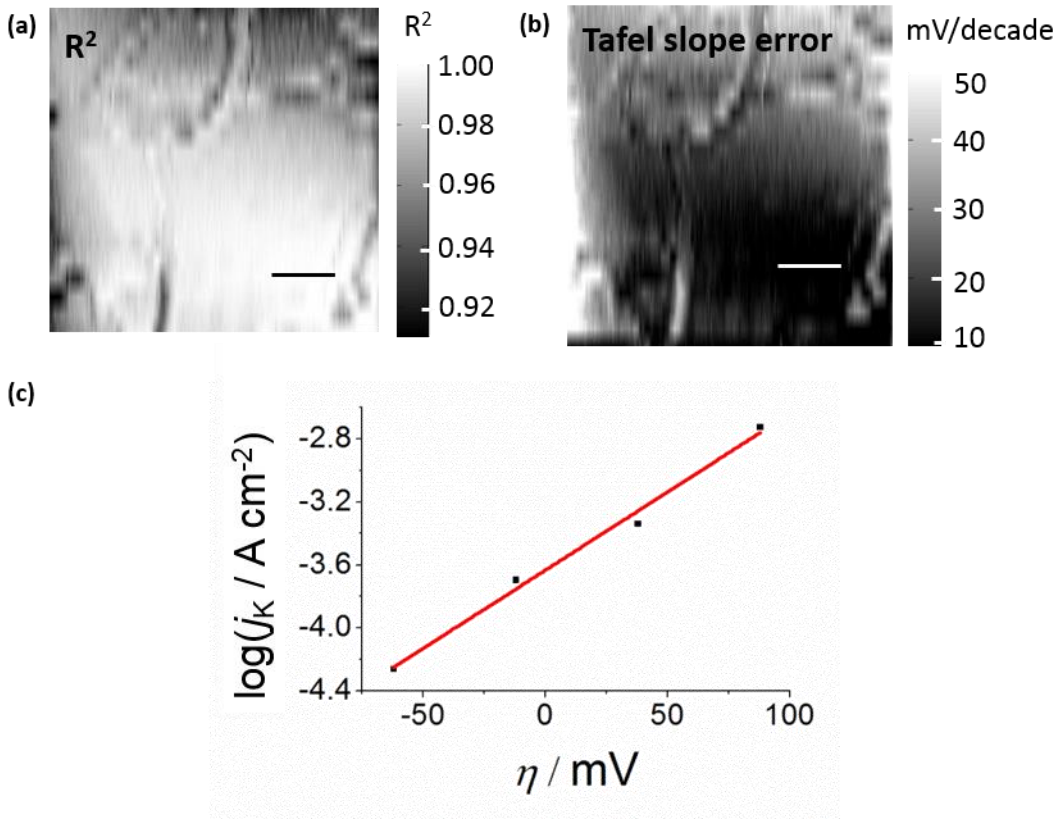

Figure 4.6 –Goodness of fit and errors for Tafel analysis. (a) Spatially resolved R^2 values. (b) Standard deviation of Tafel slope in mV/decade derived from linear fit. (c) Example of a Tafel analysis plot at a random point in the center of the image with four potential-dependent kinetic current densities (black squares) and a linear curve fit (red line) from which the Tafel slope (reciprocal of the obtained slope) and apparent j^0 value (the intercept) was extracted. The slope is 0.009 decade per mV (corresponding to a Tafel slope of 100 mV per decade) and the intercept 8.39 ± 0.03. R^2 is 0.99.

Owing to the complexity of the triiodide reduction reaction, effective heterogeneous electron transfer rate constants (k^0) cannot be directly calculated without a deeper understanding of the mechanism or without making many

misleading assumptions. We have therefore used the current exchange densities to qualitatively compare between the activities of the grains composing the electrode surface. These are shown as images in Figure 4.7a and 4.7b, respectively.

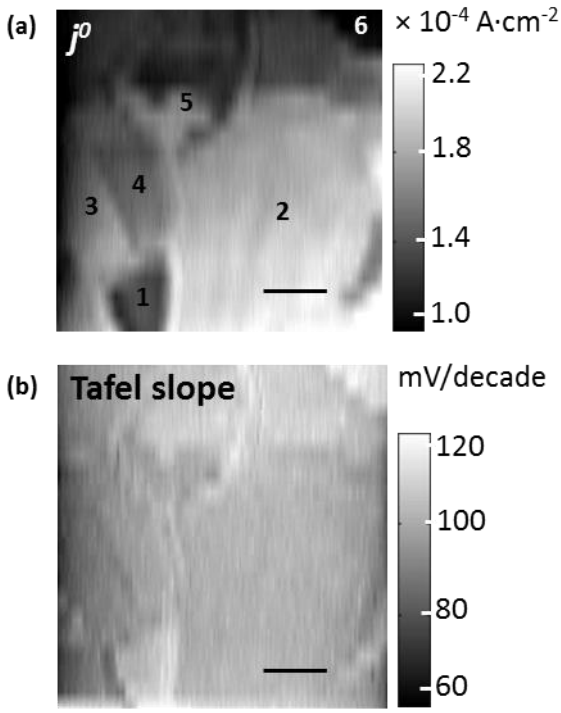

Figure 4.7 Tafel analysis of SECCM images. (a) Spatially resolved exchange current densities (j^0) values for the reduction of I_3^- from the analysis of SECCM images. Several well-defined grains are numbered. (b) Spatially resolved Tafel slope analysis of the area in (a). Scale bar in (a) and (b) is 10 μm.

The variation in effective j^0 is between (1.8 ± 0.3) × 10^{-4} A·cm^{-2}, for the more active grains (e.g. 2, 3 and 5 in Figure 4.7a) and (0.9 ± 0.1) × 10^{-4} A·cm^{-2} for the less active grains (e.g. 1 and 6 in Figure 5(a)). Figures 4.4 and 4.7 highlight key information from SECCM on spatially resolved ET kinetics that is lost in macroscale measurements involving polycrystalline platinum electrodes. Figure 4.7b shows that the apparent Tafel slopes display little variation across the surface (see also Figure

4.6), with all grains between 100 and 120 mV per decade, suggesting that the rate determining step[6,8,29] in the mechanism in all grains is the first electron transfer (nominally 120 mV per decade).

4.4 Conclusions

In the context of DSSCs, this study reveals that the rate of the I_3^- reduction process at the (polycrystalline) CE is structure-dependent and is influenced by the subtle variations in crystallographic orientation of the electrode. Pt CEs with more (110) character will improve the activity of the process. The unique advantage of SECCM over single crystal measurements is the ability to investigate high index facets which are difficult to obtain through controlled synthesis but are ubiquitous in practical applications.

This study has also opened up spatially resolved measurements of fundamental electrochemical and electrocatalytic processes in RTILs, which are of considerable (and growing) interest for many important applications in energy technologies, electrosynthesis and sensing. As shown in this chapter, SECCM is able to resolve variations in surface activity that are missed in conventional macro-scale techniques and, furthermore, through the use of complementary microscopy and structural techniques, is able to readily identify the best surfaces for optimal (electro)catalysis with the advantage of being able to probe high index facets.

4.5 References

(1) O'Regan, B.; Grätzel, M. *Nature* **1991**, *353*, 737.

(2) Hagfeldt, A.; Boschloo, G.; Sun, L. C.; Kloo, L.; Pettersson, H. *Chem. Rev.* **2010**, *110*, 6595.

(3) Wu, M.; Lin, X.; Wang, Y.; Wang, L.; Guo, W.; Qi, D.; Peng, X.; Hagfeldt, A.; Grätzel, M.; Ma, T. *J. Am. Chem. Soc.* **2012**, *134*, 3419.

(4) Nusbaumer, H.; Moser, J.-E.; Zakeeruddin, S. M.; Nazeeruddin, M. K.; Grätzel, M. *J. Phys. Chem. B* **2001**, *105*, 10461.

(5) Boschloo, G.; Hagfeldt, A. *Acc. Chem. Res.* **2009**, *42*, 1819.

(6) Nakata, R.; Okazaki, S.; Fujinaga, T. *J. Electroanal. Chem.* **1981**, *125*, 413.

(7) Macagno, V. A.; Giordano, M. C.; Arvía, A. J. *Electrochim. Acta* **1969**, *14*, 335.

(8) Rogers, E. I.; Silvester, D. S.; Aldous, L.; Hardacre, C.; Compton, R. G. *J. Phys. Chem. C* **2008**, *112*, 6551.

(9) Zhang, Y.; Zheng, J. B. *Electrochim. Acta* **2007**, *52*, 4082.

(10) Hapiot, P.; Lagrost, C. *Chem. Rev.* **2008**, *108*, 2238.

(11) Quinn, B. M.; Ding, Z.; Moulton, R.; Bard, A. J. *Langmuir* **2002**, *18*, 1734.

(12) Ejigu, A.; Lovelock, K. R. J.; Licence, P.; Walsh, D. A. *Electrochim. Acta* **2011**, *56*, 10313.

(13) Aaronson, B. D. B.; Chen, C.-H.; Li, H.; Koper, M. T. M.; Lai, S. C. S.; Unwin, P. R. *J. Am. Chem. Soc.* **2013**, *135*, 3873.

(14) Narayanan, R.; El-Sayed, M. A. *Nano Lett.* **2004**, *4*, 1343.

(15) Koper, M. T. M. *Nanoscale* **2011**, *3*, 2054.

(16) Tian, N.; Zhou, Z.-Y.; Sun, S.-G.; Ding, Y.; Wang, Z. L. *Science* **2007**, *316*, 732.

(17) Oja, S. M.; Wood, M.; Zhang, B. *Anal. Chem.* **2012**, *85*, 473.

(18) Bönnemann, H.; Khelashvili, G.; Behrens, S.; Hinsch, A.; Skupien, K.; Dinjus, E. *J. Cluster Sci.* **2007**, *18*, 141.

(19) Zhang, B.; Wang, D.; Hou, Y.; Yang, S.; Yang, X. H.; Zhong, J. H.; Liu, J.; Wang, H. F.; Hu, P.; Zhao, H. J.; Yang, H. G. *Sci. Rep.* **2013**, *3*.

(20) Somik, M.; Balavinayagam, R.; Griggs, L.; Hamm, S.; Baker, G. A.; Fraundorf, P.; Sengupta, S.; Shubhra, G. *Nanotechnology* **2012**, *23*, 485405.

(21) Ebejer, N.; Güell, A. G.; Lai, S. C. S.; McKelvey, K.; Snowden, M. E.; Unwin, P. R. *Annu. Rev. Anal. Chem.* **2013**, *6*, 329.

(22) Snowden, M. E.; Güell, A. G.; Lai, S. C. S.; McKelvey, K.; Ebejer, N.; O'Connell, M. A.; Colburn, A. W.; Unwin, P. R. *Anal. Chem.* **2012**, *84*, 2483.

(23) Lai, S. C. S.; Patel, A. N.; McKelvey, K.; Unwin, P. R. *Angew. Chem. Int. Ed.* **2012**, *51*, 5405.

(24) Ghilane, J.; Lagrost, C.; Hapiot, P. *Anal. Chem.* **2007**, *79*, 7383.

(25) Walsh, D. A.; Lovelock, K. R. J.; Licence, P. *Chem. Soc. Rev.* **2010**, *39*, 4185.

(26) Carano, M.; Bond, A. M. *Aust. J. Chem.* **2007**, *60*, 29.

(27) Zhao, C.; Bond, A. M.; Compton, R. G.; O'Mahony, A. M.; Rogers, E. I. *Anal. Chem.* **2010**, *82*, 3856.

(28) Bentley, C. L.; Bond, A. M.; Hollenkamp, A. F.; Mahon, P. J.; Zhang, J. *Electrochim. Acta* **2013**, *109*, 554.

(29) Hauch, A.; Georg, A. *Electrochim. Acta* **2001**, *46*, 3457.

(30) Allen, G. D.; Buzzeo, M. C.; Villagrán, C.; Hardacre, C.; Compton, R. G. *J. Electroanal. Chem.* **2005**, *575*, 311.

(31) Rogers, E. I.; Streeter, I.; Aldous, L.; Hardacre, C.; Compton, R. G. *J. Phys. Chem. C* **2008**, *112*, 10976.

(32) Lai, S. C. S.; Dudin, P. V.; Macpherson, J. V.; Unwin, P. R. *J. Am. Chem. Soc.* **2011**, *133*, 10744.

(33) Navarro-Suárez, A. M.; Hidalgo-Acosta, J. C.; Fadini, L.; Feliu, J. M.; Suárez-Herrera, M. F. *J. Phys. Chem. C* **2011**, *115*, 11147.

(34) Fletcher, S. *J. Solid State Electrochem.* **2009**, *13*, 537.

Chapter 5 Scanning Electrochemical Cell Microscopy Platform for Ultrasensitive Photoelectrochemical Imaging

Abstract

Developing nanoscale structure-activity correlations is of major importance for the fundamental understanding and rational development of (photo)electrocatalysts. However, the low conversion efficiency of characteristic materials generates photoelectrochemical currents in the fA range, at the submicron to nanoscale, which are challenging to detect and measure accurately. Here we report the coupling of SECCM with photo-illumination, to create a sub-micron spatial resolution cell that allows high resolution structure-(photo)activity measurements. We demonstrate the capabilities of the technique as a tool for: (i) high spatial resolution (photo)activity mapping using an ionic liquid electrolyte at a thin film of TiO_2 aggregates, commonly used as a photo-anode in dye sensitized solar cells (DSSCs); and (ii) in-situ (photo)activity measurements of an electropolymerized conjugated polymer on a transparent Au substrate in a controlled atmospheric environment. Quantitative data, including localized (photo)electrochemical transients and external quantum efficiency (EQE) are extracted, and prospects for further technique development and enhancement are outlined.

5.1 Introduction

Photo-electrodes for energy conversion devices typically consist of nanostructured electrodes based on nanoparticles and molecular materials. Not only does this provide substrates with high specific surface area and enhanced light absorbance characteristics, but it also opens up the possibility of fine tuning (photo)electrocatalytic properties including crystallographic orientation, size, film thickness and absorption spectrum.[1] On the other hand, correlating the structure of these materials with their local (photo)activity requires localized (photo)electrochemical measurements capable of sub-micron (nanoscale) spatial resolution where feature sizes of tens to hundreds of nanometers are typical. Furthermore, the small feature sizes as well as the low conversion efficiencies of many (photo)electrochemical systems requires high sensitivity current measurements. As a result, there have been few reports of scanning probe (photo)electrochemical measurements. In fact, these have mainly focused on scanning electrochemical microscopy (SECM) based techniques,[2-11] often as a tool for catalyst screening[4,7] on a fairly large length scale and for thick deposits of photoelectrocatalytic materials.[4,7,12,13]

Here, we use a scanning droplet cell platform that confines the electrochemical measurement to a small contact area[14,15] ensuring high spatial resolution and excellent signal-to-noise,[16] as responses from features outside the probe area are excluded. Although scanning droplet cells have found some recent application for localized photovoltaic measurements on organic materials,[17] the droplet cell in these studies (3.5 mm in diameter)[17] operates with an aerial footprint five orders of magnitude larger than herein. As a member of the scanning droplet

technique family,[18] scanning electrochemical cell microscopy (SECCM)[14,18-23] has emerged in recent years as a powerful technique to visualize electrochemistry at the nanoscale as well as to functionalize surfaces.[24,25] Key capabilities of SECCM are mainly due to: (i) a nanoscopic droplet size at the tip of the scanning probe (down to < 200 nm in diameter in published studies[15] and < 100 nm in work in progress in our group) and (ii) an independent feedback mechanism that provides constant tip-substrate separation, unambiguously allowing surface reactivity to be separated from topography.

In this chapter a description is given for an experimental setup in which photocurrent measurements are incorporated into SECCM, enabling mapping and interrogation of photoelectrochemistry at nanostructured films with high spatial resolution and signal-to-noise ratio. Using a hopping mode technique,[26] localized measurements were performed at multiple locations across heterogeneous substrate surfaces, providing individual photocurrent transient measurements at the micro to nanoscale. As light intensity modulation techniques such as intensity modulated photocurrent spectroscopy (IMPS) are useful in extracting information on the charge transport and recombination processes in photoelectrochemical systems,[27] we also show herein, as a proof of concept, the simultaneous use of a second lock-in amplifier to modulate the light intensity and measure the ac photocurrent at the same frequency.

In order to demonstrate the capabilities of SECCM coupled with illumination, we have selected two energy-related photosystems and developed two different configurations. In the first approach, related to DSSCs, (photo)electrochemical imaging of dye sensitized TiO_2 aggregates on a highly oriented pyrolitic graphite (HOPG) substrate was carried out to show the high spatial

resolution and high sensitivity of current measurements that is possible using SECCM. In a second approach, electropolymerization of a conjugated polymer poly(3-hexylthiophene) (P3HT) was carried out followed by in-situ (photo)electrochemical characterization, demonstrating the potential for materials fabrication[24,25,28] and in-situ characterization under a controlled environment.

5.2 Experimental

5.2.1 Solutions

The solution used for investigating sensitized TiO_2 films on HOPG was 13 mM of TBAI in [BMIm][BF_4], used fresh without further treatment. For the growth and in-situ characterization of P3HT on transparent Au substrates, the solution was 100 mM 3-hexylthiophene (3HT) in a 1:1 (v/v) mixture of [BMIm][BF_4] and dried acetonitrile. (see table 2.1 in section 2.1 for chemical grade and suppliers).

5.2.2 Thin film aggregates of dye sensitized TiO_2 on HOPG

A 0.24 mg/mL TiO_2 nanoparticle suspension solution was prepared in deionized water and sonicated for 15 minutes immediately before application. A small droplet (15 µL) of the resulting suspension was drop-cast on a freshly cleaved HOPG substrate (ZYB grade, SPI supplies, Aztech Trading, UK, www.2spi.com) and was dried in air. As sensitizer, we have used the bench mark dye, *cis*-diisothiocyanato-bis(2,2'-bipyridyl-4,4'-dicarboxylato) ruthenium(II)

bis(tetrabutylammonium) (N719)[29] and adopted a room temperature ionic liquid electrolyte, which is emerging as an alternative to organic based electrolytes.[22,30,31] For the sensitization of the drop-casted TiO_2 film, 30 µL of 0.3 mM solution of N719 in ethanol was applied on the dried droplet several times (4 to 5) to ensure maximum absorption of dye on the film and dried in air. Finally, the sample was thoroughly rinsed in ethanol to wash away excess dye and dried under a flow of N_2.

5.2.3 Photo-SECCM setup

A schematic description of the photo-SECCM setup is shown in Figure 5.1. In brief, dual channel glass (theta) capillaries were pulled to create a tapered end of 2-3 µm and 450 nm in diameter for the linear sweep voltammogram of sensitized TiO_2 film on HOPG (section 5.3.1) and the hopping mode scanning of sensitized TiO_2 films on HOPG (section 5.3.2), respectively. In the study of P3HT deposition on transparent Au substrates (section 5.3.4), an elliptically shaped SECCM tip (4.6 µm major axis and 2.2 µm minor axis) was used. The resulting SECCM probes were filled with the solution of interest (see section 5.2.1) to form a small meniscus at the end of the tip. Ag wire, was inserted in each 'barrel' to act as a quasi-reference counter electrode (QRCE), and a bias potential (V_2) was applied between the two QRCEs to induce a conductance current (i_{dc}) through the meniscus which was continuously monitored, providing the basis for the tip-substrate separation feedback mechanism (section 1.2).[18-20] The potential of the substrate was controlled via V_1 (Figure 5.1), where the potential of the surface (V_{Surf}) is expressed as: $V_{Surf} = -V_1 - V_2/2$.[20] The current through the substrate (i_{Surf}) was continuously recorded with a home-built four decade autoranging current follower, optimized for ultra-low current

low noise measurement. A specialized electrometer and an eighth-order brick wall filter allowed the measurement of currents in the range of only tens of fA (see further details in section 5.2.3.1). Positional feedback (height of the probe with respect to the surface) was achieved by modulating the probe position with a small amplitude in the direction perpendicular to the surface and a lock-in amplifier to detect the conductance current (i_{ac}) across the droplet at the end of the tip of the scanning probe (essentially independent of surface reactivity).[19,20] For the study of P3HT, the tip and sample were placed in a N_2 purged environmental cell to assist in drying of the meniscus at the end of the tip.[22]

The light source was a cool-white 5,000 – 10,000 K CCT light emitting diode (LED) (Cree XLamp XR-E Series, Cree, USA). The LED intensity could either be set to a fixed dc value or modulated via an additional external lock-in amplifier giving rise to a measurable ac photocurrent for photoactive surfaces. Unless otherwise stated, the light intensity was modulated. In the case a fixed light intensity illumination was used, the LED intensity was set to the maximum intensity (33 mW cm^{-2}, measured using a laser power meter (Newport, model 407A, USA)). The light was passed through a 1.00 ± 0.02 mm diameter UV-Vis optical fibre (Ocean Optics, USA) with a SMA 90 connector which was placed at a distance of 2 cm from the sample either from the bottom or the top of the substrate, creating a spot size of ca. 5 mm diameter.

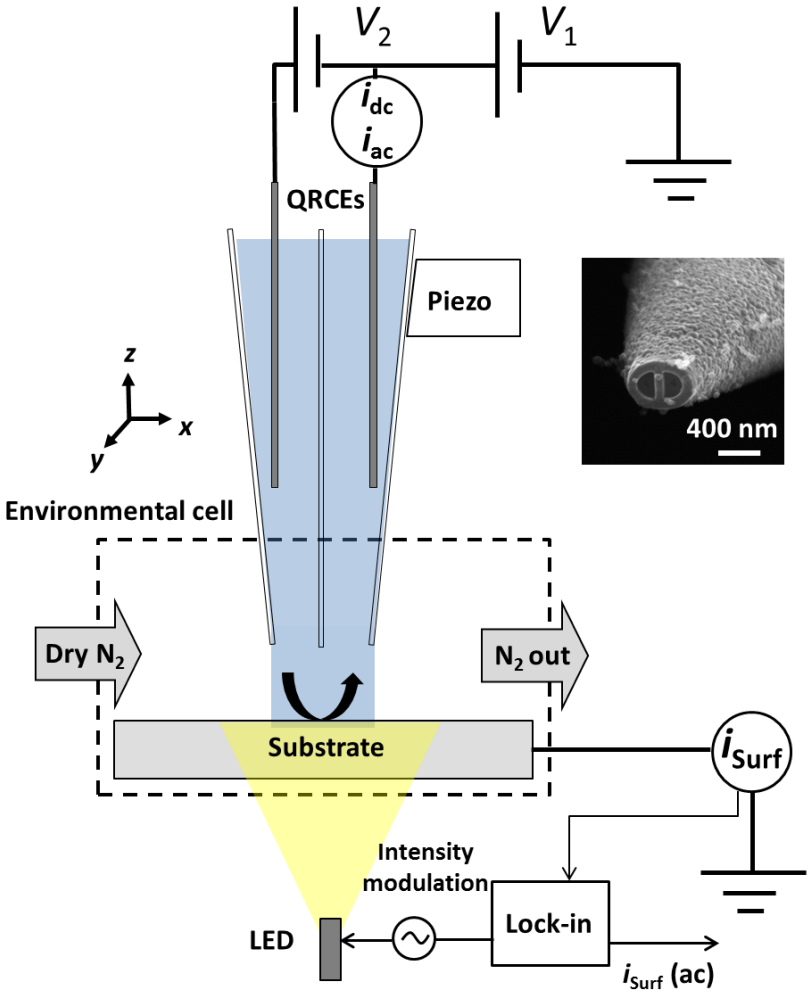

Figure 5.1 Schematic of SECCM with illumination. A dual barrel glass pipette pulled to a fine point serves as a local probe. A field emission scanning electron microscope (FE-SEM) image of a typical probe (450 nm diameter, corresponding to an aerial footprint of 1.6×10^{-9} cm^2) is shown in the inset. The working electrode potential ($V_{Surf} = -V_1 - V_2/2$)) was varied by changing V_1 and the resulting surface current (i_{Surf}) was recorded. An LED was used in either a bottom (as shown) or top illumination configuration. A bias potential (V_2) of +0.15 V was applied between two Ag quasi-reference counter electrodes (QRCEs) resulting in a conductance current (i_{dc}). An external lock-in amplifier was used for light intensity modulation and to measure the resulting photocurrent at the same frequency (i_{Surf} (ac)).

5.2.3.1 Electronics setup for photo-SECCM

A schematic of the electronic components is shown in Figure 5.2. A small modulation to the tip height (*z* coordinate), with a magnitude corresponding to a 40 nm peak to peak oscillation (~ 10% of the tip diameter) and at a frequency of 123.7 Hz, was employed using a lock-in amplifier (SR810, Stanford Research Systems, USA) giving rise to a clear alternating current (i_{ac}) component in i_{dc} response upon meniscus contact with the surface, as the geometry of the meniscus changed periodically and altered the resistance.[20] i_{ac} was measured at the same frequency as the applied modulation (lock-in amplifier 1 in Figure 5.2).

In order to achieve fidelity of the surface current measurement (i_{Surf}, in Figure 5.2 and in Figure 5.1), especially at the tens of fA level, i_{Surf} was measured by a locally positioned electrometer head unit along conductors insulated from surrounding parts on polytetrafluoroethylene (PTFE) stand-offs. The response time and noise performance of the electrometer were controlled by a variable frequency eighth-order brick wall filter unit. The entire setup was placed in a Faraday cage to minimize electronic noise.

A second lock-in amplifier (SR830, Stanford Research Systems, USA) was employed to generate a sinusoidal wave applied to the LED module at a frequency of 9 Hz between 0.0 V and + 2.5 V, corresponding to 0 intensity and maximum intensity (33 mW cm^{-2}), respectively. A time constant was selected for the second lock-in amplifier (1 second) that was sufficiently longer than the modulating frequency (9 Hz). The ON/OFF trigger for the LED was operated electronically (TTL) via the light module communication port where signals were managed through the LabVIEW interface.

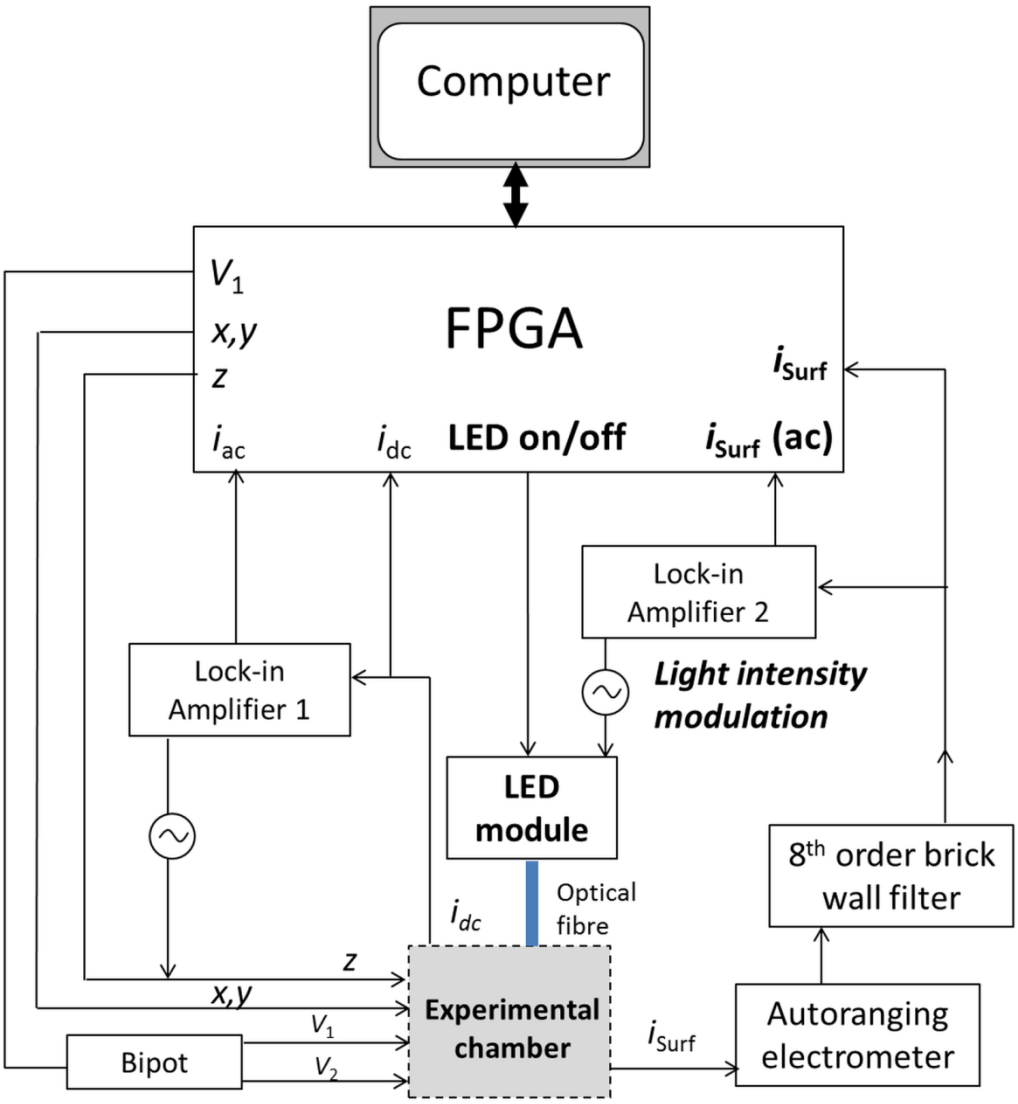

Figure 5.2 Schematic of the electronic components for photo-SECCM: a lock-in amplifier (lock-in amplifier 1) was used to modulate the tip height (*z*) and measure i_{dc} at the same frequency (i_{ac}) to provide positional feedback of the probe (normal to the surface). The (photo)electrochemical current, i_{Surf}, was recorded with an autoranging electrometer and filtered using an eighth-order brick wall filter. A second external lock-in amplifier (lock-in amplifier 2) was used to modulate the light

intensity and measure i_{Surf} at the same frequency (i_{Surf} (ac)). A home-built bi-potentiostat controlled V_1 and V_2. All data were recorded on an FPGA card and accessed via a LabVIEW interface.

5.2.4 SECCM scanning parameters and data acquisition

Data points were the average of 1024 acquisition periods of 4 µs per data point (corresponding to an acquisition time of ca. 4 ms per data point). In the hopping scan, the piezoelectric positioner movement was fixed to a speed of 1 µm s^{-1}. The hopping distance was set to 1 µm in both *x* and *y* coordinates and a retraction distance of 6 µm in the *z* axis (height) set after each hop measurement. The scan area was a 9 × 4 µm corresponding to 50 hop measurements (10 hops in the *x* direction for each of the 5 rows in the *y* direction).

5.3 Results and discussion

5.3.1 SECCM control experiments - dye sensitized TiO_2 films on HOPG

In order to identify an appropriate potential for the (photo)electrochemical measurements, an SECCM linear sweep voltammogram (LSV) was recorded on a dense area of a drop-casted N719 sensitized TiO_2 film on HOPG using a 2-3 µm diameter SECCM tip containing 13 mM TBAI in [BMIm][BF_4]. A top illumination configuration was adopted due to the opaqueness of the HOPG substrate. Constant light intensity (dc) was used and switched on and off manually for the LSV shown in Figure 5.3. Starting at 0.0 V vs Ag QRCE and sweeping in the anodic direction, the

film is photosensitive in the entire potential range, with the maximum increase in anodic current, upon illumination, of about 8 pA at + 0.8 V vs Ag.

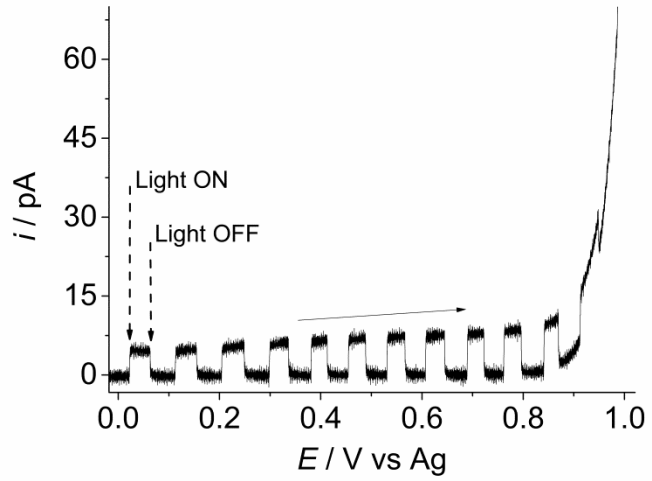

Figure 5.3 SECCM linear sweep voltammogram of 13 mM TBAI in [BMIm][BF_4] recorded with a tip of 2-3 µm inner diameter in meniscus contact with a sensitized TiO_2 film on HOPG. Sweep rate was 0.1 V s^{-1}. Black arrow indicates the direction of the linear sweep. A top illumination cool-white LED (6500 K CCT) was manually switched ON and OFF during the measurement.

In order to verify that the source of photo-current, observed in Figure 5.3, was solely due to the sensitized TiO_2 film, control experiments were conducted using a 2-3 µm SECCM tip containing 13 mM TBAI in [BMIm][BF_4] on the various components under dark and illumination conditions. LSVs in the range performed on the sensitized sample were carried out on: HOPG, HOPG with N719 dye applied (but without the presence of TiO_2) and HOPG with TiO_2 drop-casted but un-sensitized under dark and illumination conditions. The LSVs (Figure 5.4) show no significant photo-response, ruling out their contribution to the measured response in the SECCM scanning of N719 TiO_2 sensitized films presented in Figure 5.3.

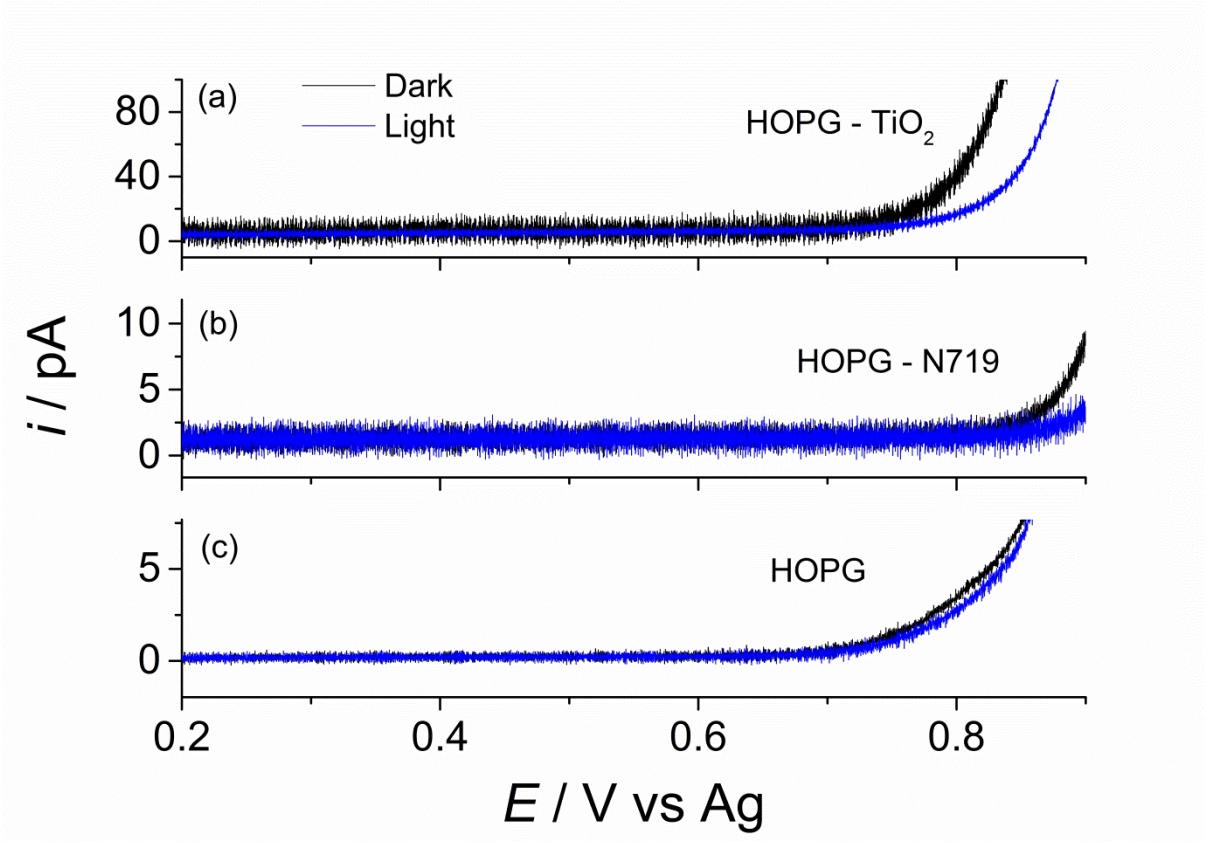

Figure 5.4 Linear sweep voltammograms of 13 mM TBAI in [BMIm][BF_4] on components of the DSSC in the dark (black line) and under illumination (blue line) for: TiO_2 drop-casted on HOPG (a), HOPG with N719 dye (b) and bare HOPG (c). Sweep rate is 0.1 Vs^{-1}. For each set, the LSV in the dark was taken before the LSV under illumination.

5.3.2 Photo-SECCM hopping scans on dye sensitized TiO_2 films

A 9 × 4 µm SECCM scan was performed on a drop-casted sensitized TiO_2 film on HOPG with a tip containing I^- (13 mM tetrabutylammonium iodide) in an ionic liquid (1-butyl-3-methylimidazolium tetrafluoroborate [BMIm][BF_4]). During scanning, the substrate potential was held at a fixed value of + 0.4 V vs Ag QRCE as determined by linear sweep voltammetry (LSV) under illumination (section 5.3.1).

To facilitate localized transient measurements, a hopping mode scan was adopted as illustrated in Figure 5.5a. Hopping mode scans consisted of a series of approach/retract measurements arranged in a rectangular array at predefined locations in the xy plane of the sample. Each approach/retract measurement is referred to as a 'hop'. The hopping scans were performed with a separation of 1 µm between each point in the *xy* plane, using a probe with a tip diameter (450 nm) that was smaller than the hopping distance to avoid overlap of hop measurements. A bias of + 0.16 V was applied between the QRCEs[18,20,22] resulting in a stable i_{dc} of circa 0.2 nA across the meniscus. Once the surface was detected using i_{ac} as feedback (step 1 in Figure 5.5a), the tip movement in the *z* direction was halted and a hold time of 4 seconds was maintained (step 2 in Figure 5.5a). The initial hold time on the surface provided the substrate background measurement under dark conditions. After the initial dark hold time, the LED was turned on for photocurrent measurements for 4 seconds, which was long enough to reach quasi steady-state (step 3 in Figure 5.5a). An ac photocurrent was simultaneously generated by modulating the light intensity and measuring the response at the same frequency using a lock-in amplifier. Finally, the tip was retracted from the surface and moved to the next measurement position in the *xy* plane (steps 4 and 5 in Figure 5.5a).

Typical transients (surface current vs time) of hop measurements on a bare HOPG substrate and on photoactive (HOPG with sensitized TiO_2 film) areas are shown in Figure 5.5b and 5.5c, respectively. The detection of the surface by the meniscus (at time, *t*, ($t = 0$)) is seen, in both cases, as a sharp spike in i_{Surf}. In both cases (bare HOPG and sensitized TiO_2 areas), the initial 4 seconds hold time under dark conditions, yields a low background current (around 50 fA (peak to peak)), highlighting that extremely low current signals can be measured. No change in

surface current is observed for the HOPG region when the light is switched on (Figure 5.5b), whereas the sensitized TiO_2 (Figure 5.5c) shows an increase in the surface current upon illumination, reaching a quasi-steady-state of ~ 300 fA, with a rise time of ~ 1.5 second. The rise time of the electrometer was 1 ms (with a sensitivity of 1 pA/V as here), therefore the rise time of the (photo)transient is due to the slow charge transport through the mesoporous TiO_2 thin film, which is much longer than the time constant of the filter (1 ms) and in agreement with bulk measurements.[32,33] The periodic modulation of the dc surface current seen in Figure 5.5c during illumination corresponds to the 9 Hz ac modulation in light intensity. The ability to clearly follow the periodic modulation in the dc photocurrent, without a lock-in amplifier, highlights the combined high sensitivity and reasonable bandwidth of the electrometer used herein. Finally, at t = 8 s the tip is retracted from the surface at a rate of 1 μm s^{-1}.

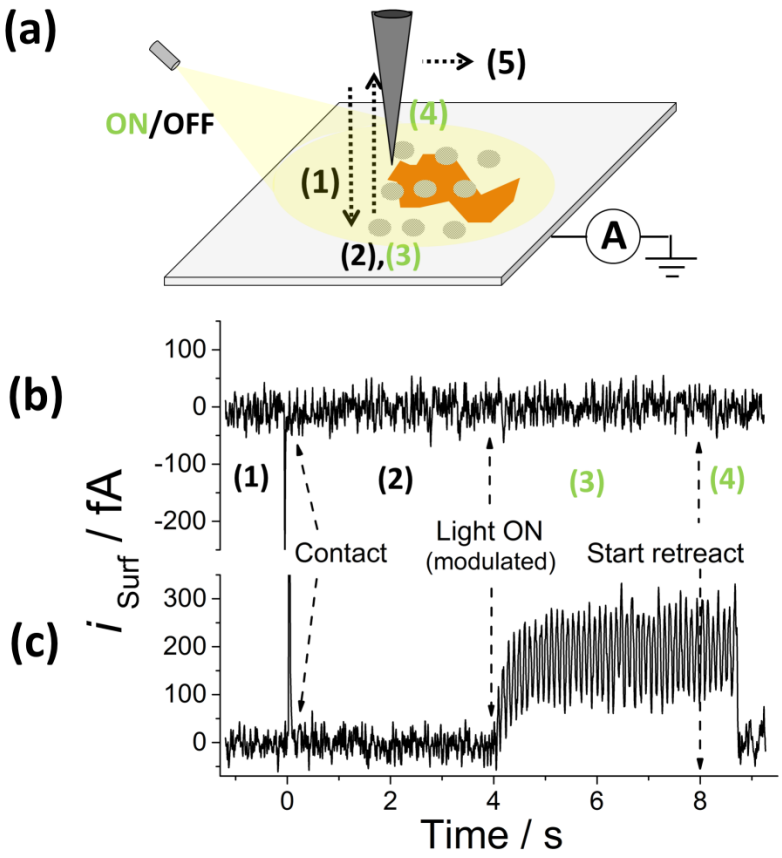

Figure 5.5 Schematic of photo-SECCM hopping scan (a): approach to surface with light OFF (1), hold time, of 4 s, on the surface with the LED OFF (2), hold time, of 4 s, on the surface with the LED ON (3), retract from surface (4), and move to new hop (5). Typical SECCM transients (surface current (i_{Surf}) vs time) of hop measurements with a tip containing 13 mM tetrabutylammonium iodide in 1-butyl-3-methylimidazolium tetrafluoroborate [BMIm][BF_4] on: nonphotoactive HOPG substrate (b) and photoactive drop casted N719 sensitized TiO_2 films (c). The surface was held at a potential of +0.4 V vs Ag QRCE, and the light intensity was modulated at 9 Hz using a lock-in amplifier.

A FE-SEM image of the SECCM scan area is shown in Figure 5.6a where residues from the SECCM hops can be seen on the surface, and assist in precisely identifying the SECCM scan area. The topography of the scanned area, obtained by SECCM (Figure 5.5b) correlates well with the FE-SEM image (Figure 5.6a), and indicate that the film aggregate is ~ 1 µm in height.

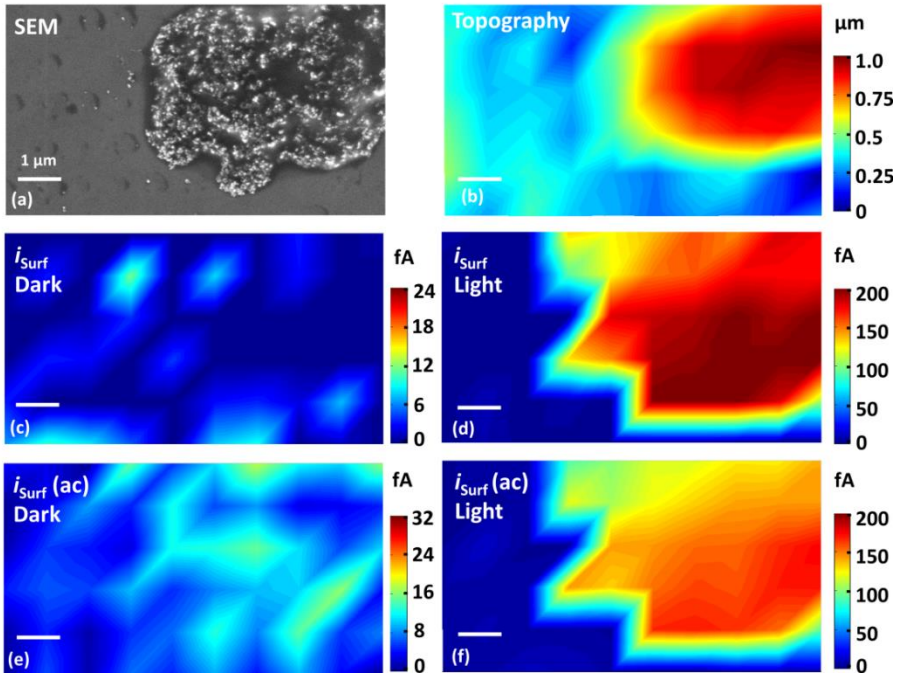

Figure 5.6 SECCM hopping mode scan of N719 sensitized TiO_2 film on HOPG: FE-SEM image of the scanned area (a), SECCM topography map (b). Surface DC SECCM maps: in the dark (~20 fA noise level) (c) and under ac illumination (d) and ac component of surface current in the dark (i_{Surf} (ac)) (e) and under ac magnitude modulated illumination (f). The tip contained 13 mM tetrabutylammonium iodide in 1-butyl-3-methylimidazolium tetrafluoroborate. The surface was held at +0.4 V vs Ag, and the light intensity was modulated at 9 Hz from 0 to 33 mW cm^{-2}. All scale bars are 1 µm.

In order to produce spatially resolved SECCM images of the surface photo-electrochemical activity (i_{Surf}) under dark conditions and under illumination, the last 100 ms (see section 5.2.5) of each segment of the localized transient (LED on and off) was averaged for each hop. Four complementary images can be produced from data that are recorded simultaneously: two maps from the dc components of i_{Surf} under dark conditions (Figure 5.6c) and under illumination (Figure 5.6d), and another two from the ac components of i_{Surf} (ac) (due to the ac modulation of the LED intensity), detected with the lock-in amplifier, in the dark (Figure 5.6e) and under illumination (Figure 5.6f).

The images under dark conditions (Figures 5.6c and 5.6e) highlight the low noise level of the setup (note the difference in dark and illuminated current scales). A strong spatial correlation appears between the SEM image in Figure 5.6a and the (photo)activity maps in Figure 5.6d and 5.6f. As we aimed to increase the signal-to-noise for the i_{Surf} (ac) amplitude measurements, a time constant of 1 second for the lock-in amplifier was chosen (sufficiently longer than the intensity modulation frequency). In future work, on other systems, optimization of the frequency of light modulation and time constant settings may allow a full analysis of the ac amplitude and phase components so that IMPS techniques could be implemented. It is important to point out that photocurrents produced from films with a thickness of less than a micron, are detectable in the setup herein, providing a significant improvement compared to the sensitivity of previous local measurements.[34-36] The external quantum efficiency (EQE) can be calculated for each hop, providing valuable localized information. The EQE calculated for the highest photo-electrochemical current recorded (~ 200 fA) in the scanned area corresponds to 0.8 % (see section 5.3.3), suggesting that even thin sensitized films (< 2 μm) can yield

relatively high conversion efficiencies, in agreement with previous macroscopic studies.[37]

5.3.3 External quantum efficiency (EQE) of sensitized TiO_2

The EQE is defined as the number of electrons collected divided by the number of incident photons hitting the sample. In order to calculate the EQE of the sensitized TiO_2 aggregate films for a single spot measurement, a precise estimate of the incident photons at the confined (photo)electrochemical area (the contact area of the SECCM meniscus with the substrate) is required.

Since the relative intensity of the emission spectrum of the LED is known, a precise energy distribution can be obtained from a single total intensity measurement (33 mW cm^{-2}). From the normalised energy distribution the number of photons hitting the sample per unit area was then calculated, shown in Figure 5.7. Integrating the photon distribution yields the total number of photons arriving at the sample per unit area per second. Assuming the (photo)electrochemical area is confined at a tip diameter of 450 nm (area = 1.59×10^{-9} cm^2), the light flux is 1.44×10^8 photons s^{-1} in the area under the SECCM probe. The highest current measured under illumination (~ 200 fA) corresponds to 1.25×10^6 electrons s^{-1} and the EQE is thus, 0.8 %.

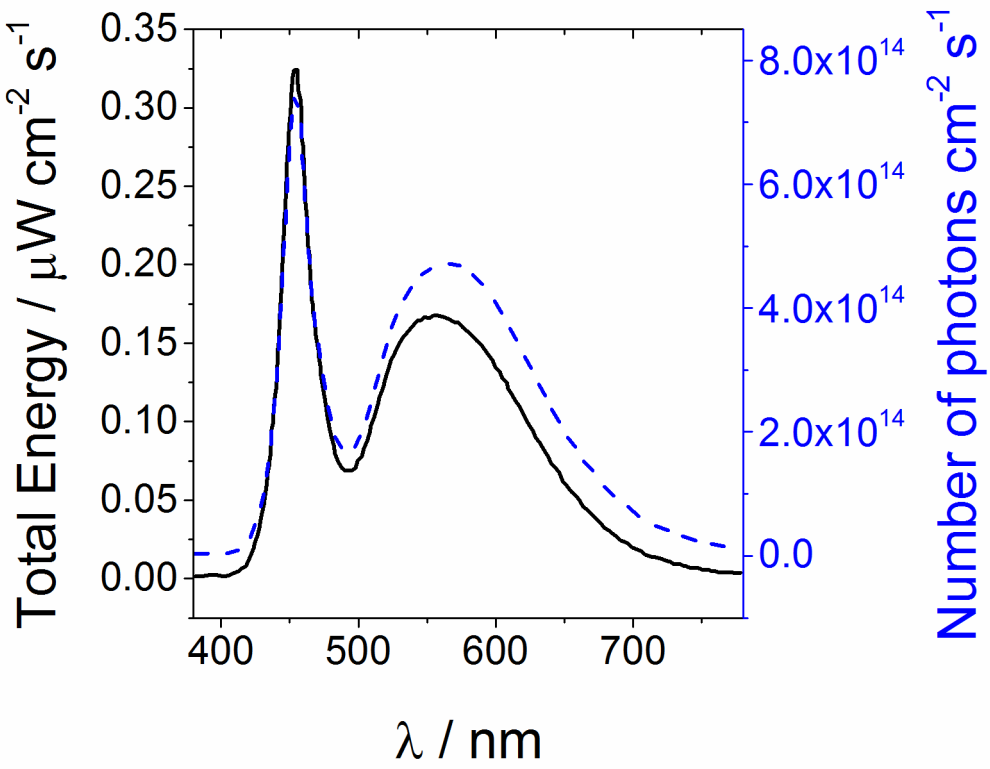

Figure 5.7 LED light intensity distribution: energy per unit area (continuous black line) and the corresponding number of photons (blue dotted line).

5.3.4 P3HT deposition using SECCM

To demonstrate the capability of in-situ photo-electrochemical characterization of minimal organic material, we grew P3HT electrochemically[38,39] on a transparent Au substrate,[40] using cyclic voltammetry in a SECCM setup. In order to provide in-situ measurements of the freshly deposited P3HT film, the photocurrents were measured with the same tip used for deposition (i.e. a tip containing the 3HT monomer). Since the polymerization of P3HT is known to suffer from the presence of water,[41] the experiments were performed using an environmental cell with N_2 gas flowed in to assist in the drying of the meniscus. Depositions performed without N_2 flow produced poor quality films (as reflected in

their voltammograms). The SECCM tip contained a solution of 0.1 M 3HT in a 1:1 (v/v) mixture of [BMIm][BF_4] and dried acetonitrile and was approached to the surface using i_{ac} as feedback with an applied bias potential (V_2) of 0.15 V between the two Ag QRCEs. Tip movement towards the substrate was halted automatically. The bias potential (V_2) was then set to 0 V since positional feedback was not necessary during the deposition and photo-characterization. One voltammetric cycle was performed between 0.0 V and + 1.45 V vs Ag QRCE (promoting the polymerization of 3HT)[38,39] and is shown in Figure 5.8a. On the return sweep (cathodic), a clear un-doping peak is observed at around +0.6 V vs Ag, indicating that P3HT was deposited. To further confirm that the deposited P3HT film was adhered to the surface, a single cycle characterization CV (limited to the potential range for the onset of monomer oxidation) was recorded and is shown in Figure 5.8b. The CV shows two characteristic peaks of doping/un-doping of a P3HT film.[38,42] In order to ensure that the as-prepared film was in a reduced (un-doped) state[38,42] the potential was held at a reducing potential (0.0 V vs Ag QRCE) for another 60 seconds before in-situ photo-characterization. This was long enough to obtain a steady-state background current that was not changing with time due to polymer reduction.

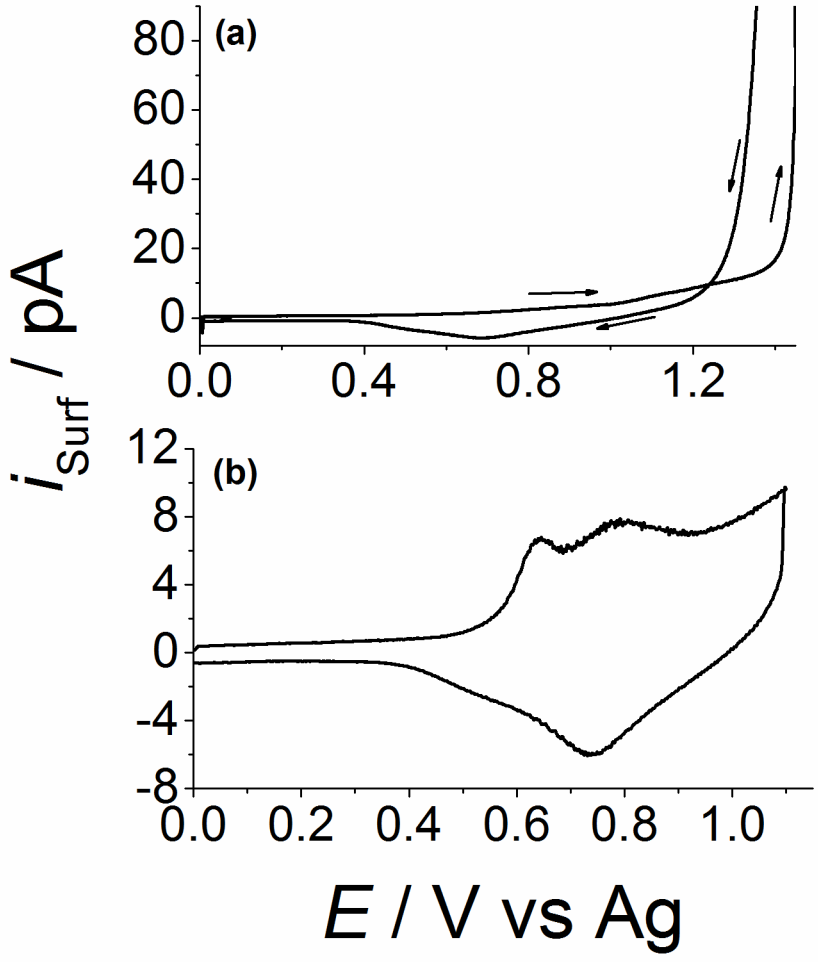

Figure 5.8 SECCM CV growth and characterization of P3HT on a transparent Au substrate. A deposition CV of P3HT (a), the initial potential applied to the surface was 0.0 V and swept to + 1.45 V vs Ag QRCE at a scan rate of 0.15 V s^{-1}. Black arrows indicate the sweep direction. Characterization CV of the freshly deposited film (b), between 0.0 V and + 1.1 V vs Ag QRCE. The starting potential was 0.0 V and the scan rate was 0.1 V s^{-1}. The SECCM tip in (a) and (b) contained 0.1 M 3-hexyl thiophene in a 1:1 (v/v) mixture of [BMIm][BF_4] and dried acetonitrile.

5.3.5 In-situ photoelectrochemical characterization of P3HT films on transparent Au substrates

For photocurrent characterization, a bottom illumination configuration was adopted and the LED intensity was set to a fixed value (without intensity modulation). The (photo)electrochemical response and corresponding FE-SEM image of the deposited film are shown in Figure 5.9. During the photocurrent measurement the surface was held at 0 V vs Ag (a potential range where the polymer is known to be un-doped).[39] A cathodic photocurrent transient was observed due to minority carrier generation (electrons) upon illumination ($3 \leq t \leq 7$ s), which led to the reduction of dissolved oxygen in the tip solution. Importantly the noise level during the photocurrent measurement is only ~ 6 fA, which permits the (photo)electrochemical response (~ 30 fA) to be clearly resolved during illumination. The FE-SEM image reveals a small amount of film on the Au substrate, roughly the size of the SECCM tip footprint (4.6 µm and 2.2 µm major and minor axis, respectively). The capability of measuring such low (photo)responses from minimal amounts of material further highlights the use of photo-SECCM for studying thin molecular or organic materials at the micron to nanoscale.

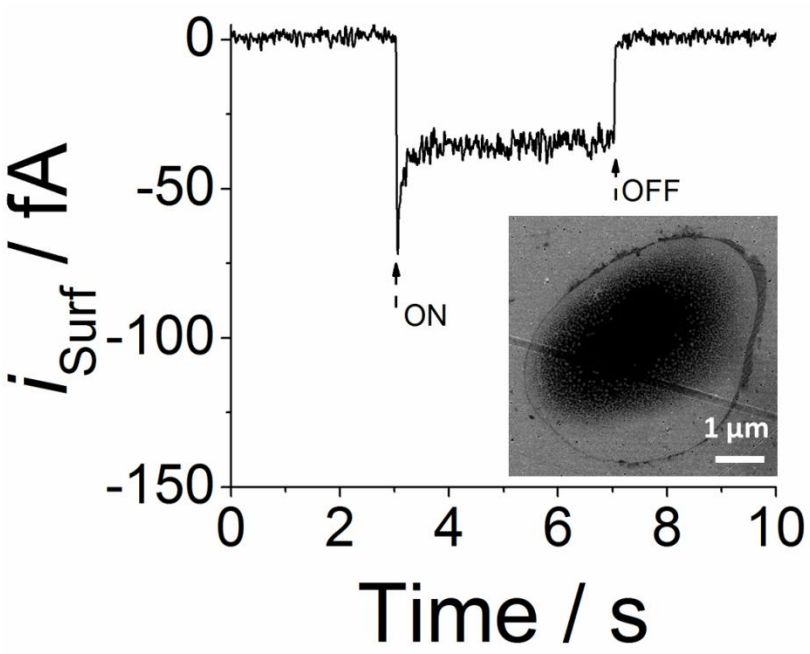

Figure 5.9 SECCM surface (photo)current–time transients on a P3HT film deposited on a transparent Au substrate. The surface was held at 0.0 V vs Ag QRCE during the measurements. The light source was switched ON at t = 3 s and then OFF at t = 7 s. The SECCM tip (4.6 and 2.2 µm major and minor axis, respectively) contained 0.1 M 3-hexyl thiophene in a 1:1 (v/v) mixture of [BMIm][BF_4] and dried acetonitrile. A FE-SEM image of the P3HT film is shown in the inset.

5.4 Conclusions

An SECCM platform has been described that enables the investigation of (photo)electrochemical systems at the micro to nanoscale with high sensitivity. The high spatial resolution achieved with SECCM (photo)electrochemical imaging has been coupled with ultrasensitive measurements at the tens of fA range, opening up prospects for accessing a wide range of (photo)electrochemical phenomena, with

future applications, such as assessing materials for solar energy conversion, water treatment, bio-sensing and photosynthesis.

A variety of substrates can be investigated with top and bottom illumination and the LED could be easily replaced to access different spectral regions (for example, UV illumination for semiconductors with a wide band gap) as well as infra-red. SECCM coupled with photo-illumination should be useful as a rapid in-situ screening technique. All of these features offer significant opportunity in nanoscale (photo)electrochemistry, and can be employed together with complementary microscopy techniques in a multi-microscopy approach on the same region of a sample. Furthermore, ac photocurrent techniques such as IMPS methods could be implemented at the nanoscale, in the future.

5.5 References

(1) Rodríguez, J. A.; Fernández-Garcia, M. *Synthesis, Properties, and Applications of Oxide Nanomaterials*; John Wiley & Sons: New Jersey, 2007.

(2) Lai, S. C. S.; Macpherson, J. V.; Unwin, P. R. *MRS Bulletin* **2012**, *37*, 668.

(3) Wang, Z.-S.; Sayama, K.; Sugihara, H. *J. Phys. Chem. B* **2005**, *109*, 22449.

(4) Lee, J.; Ye, H.; Pan, S.; Bard, A. J. *Anal. Chem.* **2008**, *80*, 7445.

(5) Amemiya, S.; Bard, A. J.; Fan, F.-R. F.; Mirkin, M. V.; Unwin, P. R. *Annu. Rev. Anal. Chem.* **2008**, *1*, 95.

(6) Wittstock, G.; Burchardt, M.; Pust, S. E.; Shen, Y.; Zhao, C. *Angew. Chem. Int. Ed.* **2007**, *46*, 1584.

(7) Zhang, F.; Roznyatovskiy, V.; Fan, F.-R. F.; Lynch, V.; Sessler, J. L.; Bard, A. J. *J. Phys. Chem. C* **2011**, *115*, 2592.

(8) Yuan, D.; Xiao, L.; Jia, J.; Zhang, J.; Han, L.; Li, P.; Mao, B.-W.; Zhan, D. *Anal. Chem.* **2014**, *86*, 11972.

(9) Fernando, A.; Parajuli, S.; Alpuche-Aviles, M. A. *J. Am. Chem. Soc.* **2013**, *135*, 10894.

(10) Haram, S. K.; Bard, A. J. *J. Phys. Chem. B* **2001**, *105*, 8192.

(11) Park, H. S.; Leonard, K. C.; Bard, A. J. *J. Phys. Chem. C* **2013**, *117*, 12093.

(12) Kylberg, W.; Wain, A. J.; Castro, F. A. *J. Phys. Chem. C* **2012**, *116*, 17384.

(13) Martin, C. J.; Bozic-Weber, B.; Constable, E. C.; Glatzel, T.; Housecroft, C. E.; Wright, I. A. *Electrochim. Acta* **2014**, *119*, 86.

(14) Güell, A. G.; Meadows, K. E.; Dudin, P. V.; Ebejer, N.; Macpherson, J. V.; Unwin, P. R. *Nano Lett.* **2014**, 220.

(15) Güell, A. G.; Ebejer, N.; Snowden, M. E.; McKelvey, K.; Macpherson, J. V.; Unwin, P. R. *Proc. Natl. Acad. Sci. U. S. A.* **2012**, *109*, 11487.

(16) Kleijn, S. E. F.; Lai, S. C. S.; Miller, T. S.; Yanson, A. I.; Koper, M. T. M.; Unwin, P. R. *J. Am. Chem. Soc.* **2012**, *134*, 18558.

(17) Kollender, J. P.; Gasiorowski, J.; Sariciftci, N. S.; Mardare, A. I.; Hassel, A. W. *J. Phys. Chem. C* **2014**, *118*, 16919.

(18) Ebejer, N.; Güell, A. G.; Lai, S. C. S.; McKelvey, K.; Snowden, M. E.; Unwin, P. R. *Annu. Rev. Anal. Chem.* **2013**, *6*, 329.

(19) Ebejer, N.; Schnippering, M.; Colburn, A. W.; Edwards, M. A.; Unwin, P. R. *Anal. Chem.* **2010**, *82*, 9141.

(20) Snowden, M. E.; Güell, A. G.; Lai, S. C. S.; McKelvey, K.; Ebejer, N.; O'Connell, M. A.; Colburn, A. W.; Unwin, P. R. *Anal. Chem.* **2012**, *84*, 2483.

(21) Aaronson, B. D. B.; Chen, C.-H.; Li, H.; Koper, M. T. M.; Lai, S. C. S.; Unwin, P. R. *J. Am. Chem. Soc.* **2013**, *135*, 3873.

(22) Aaronson, B. D. B.; Lai, S. C. S.; Unwin, P. R. *Langmuir* **2014**, *30*, 1915.

(23) Güell, A. G.; Ebejer, N.; Snowden, M. E.; Macpherson, J. V.; Unwin, P. R. *J. Am. Chem. Soc.* **2012**, *134*, 7258.

(24) Kirkman, P. M.; Güell, A. G.; Cuharuc, A. S.; Unwin, P. R. *J. Am. Chem. Soc.* **2013**, *136*, 36.

(25) McKelvey, K.; O'Connell, M. A.; Unwin, P. R. *Chem. Commun.* **2013**, 2986.

(26) Williams, C. G.; Edwards, M. A.; Colley, A. L.; Macpherson, J. V.; Unwin, P. R. *Anal. Chem.* **2009**, *81*, 2486.

(27) Peter, L. M. *J. Phys. Chem. C* **2007**, *111*, 6601.

(28) Laslau, C.; Williams, D. E.; Kannan, B.; Travas-Sejdic, J. *Adv. Funct. Mater.* **2011**, *21*, 4607.

(29) Hagfeldt, A.; Boschloo, G.; Sun, L. C.; Kloo, L.; Pettersson, H. *Chem. Rev.* **2010**, *110*, 6595.

(30) Hapiot, P.; Lagrost, C. *Chem. Rev.* **2008**, *108*, 2238.

(31) Quinn, B. M.; Ding, Z.; Moulton, R.; Bard, A. J. *Langmuir* **2002**, *18*, 1734.

(32) Dloczik, L. *J. Phys. Chem. B* **1997**, *101*, 10281.

(33) Walker, A. B.; Peter, L. M.; Lobato, K. *Chimia* **2007**, *61*, 792.

(34) Jiu, J.; Isoda, S.; Wang, F.; Adachi, M. *J. Phys. Chem. B* **2006**, *110*, 2087.

(35) Kang, M. G.; Ryu, K. S.; Chang, S. H.; Nam Gyu Park; Hong, J. S.; Kim, K.-J. *Bull. Korean Chem. Soc.* **2004**, *25*, 742.

(36) Kao, M. C.; Chen, H. Z.; Young, S. L.; Kung, C. Y.; Lin, C. C. *Thin Solid Films* **2009**, *517*, 5096.

(37) Ahn, S. H.; Park, J. T.; Koh, J. K.; Roh, D. K.; Kim, J. H. *Chem. Commun.* **2011**, *47*, 5882.

(38) Hillman, A. R.; Mallen, E. F. *J. Electroanal. Chem.* **1987**, *220*, 351.

(39) Ratcliff, E. L.; Jenkins, J. L.; Nebesny, K.; Armstrong, N. R. *Chem. Mater.* **2008**, *20*, 5796.

(40) Stec, H. M.; Hatton, R. A. *Adv. Energy Mater.* **2013**, *3*, 193.

(41) Heinze, J.; Frontana-Uribe, B. A.; Ludwigs, S. *Chem. Rev.* **2010**, *110*, 4724.

(42) Li, F.; Albery, W. J. *J. Chem. Soc., Faraday Trans.* **1991**, *87*, 2949.

Chapter 6 Electrodeposition and Screening of (Photo)electrochemical Activity in Conjugated Polymers Using Scanning Electrochemical Cell Microscopy

Abstract

A number of renewable energy systems, requires an understanding and correlation of material properties and (photo)electrochemical activity on the micro to nanoscale. Among these, conducting polymer electrodes continue to be important materials. In this chapter, an ultrasensitive scanning electrochemical cell microscopy (SECCM) platform is used to electrodeposit microscale thin films of poly(3-hexylthiophene) (P3HT) on an optically transparent gold electrode and to correlate the morphology (film thickness and structural order) with photo-activity. The electrochemical growth of P3HT begins with a thin ordered film up to 10 nm thick, after which a second more disordered film is deposited, as revealed by micro-Raman spectroscopy. A decrease in photo-activity for the thicker films, measured in-situ immediately following film deposition, is attributed to an increase in bulk film disorder that limits charge transport. Higher resolution ex-situ SECCM photo-transient measurements, using a smaller diameter probe, show local variations in photo-activity within a given deposit. Even after aging, thinner, more ordered regions within a deposit exhibit sustained enhanced photocurrent densities compared to areas where the film is thicker and more disordered. The platform opens up new possibilities for high-throughput combinatorial correlation studies, by allowing materials fabrication and high spatial resolution probing of processes in photoelectrochemical materials.

6.1 Introduction

A major avenue in the search for renewable energy system is the development of efficient photoelectrochemical cells for the conversion of sunlight to fuel. Prominent for photoelectrocatalysis are metal oxides,[1] which have been the choice of material for fuel production,[2] although many are limited by a wide band-gap and the mismatch of energy levels for the hydrogen evolution reaction (HER) and oxygen evolution reaction (OER) in solar water splitting devices.[3,4] In the arena of low band-gap semiconductors, organic solar cells[5-8] have been explored, mainly as alternatives for solid state inorganic p-n junction photovoltaic cells, to directly convert light to a flux of charge carriers. However, organic photoelectrochemical cells have more recently been considered for solar fuel applications.[9-12]

Screening of the photoelectrochemical properties of materials has been successfully accomplished using scanning electrochemical microscopy (SECM)[13-17] and scanning droplet (meniscus-contact) electrochemical techniques.[18-21] Meniscus contact cells, which can be constructed from simple glass micropipettes or nanopipettes, are particularly useful as they can be used to (electro)deposit materials and assess the electrochemical properties, via voltammetry in which several parameters can be controlled and changed over a wide range.[22-24] However, electropolymerized films can exhibit variations in thickness on the nano- and microscale,[22] and can thus have significant consequence on charge transport and photoelectrochemical conversion efficiency.[6,25]

In Chapter 5, the platform for the investigation of photoelectrochemical systems at the microscale to nanoscale[26] using SECCM[27-30] was described. In this chapter the platform is used to screen the photoelectrochemical properties of poly(3-hexylthiophene) (P3HT), a benchmark in polymer electronics,[31,32] and recently shown to exhibit high photoelectrochemical conversion efficiencies when used in a bulk heterojunction architecture for the hydrogen evolution reaction.[9] In this work (illustrated in Figure 6.1), we have used a droplet based approach to prepare a series of P3HT thin films from ~5 nm to ~475 nm in thickness in a sequential manner using electropolymerization. Multiple local characterization techniques were used to screen the influence of growth conditions on film morphology and photocurrent generation. Films were grown using a microscale single barrel pipette (approximately 15 μm in diameter) and characterized immediately following growth with the same pipette (Figure 6.1a). Subsequently, high resolution ex-situ photo-SECCM using smaller dual-barrelled pipettes (~ 3 μm) was used for measurements that could access local features within the larger electrodeposited films (Figure 6.1b). Structural characterization was obtained with Raman spectroscopy (Figure 6.1c) which has proven powerful for morphology indication,[33,34] polymer identification[35] and assessing the order of organic films.[36] Atomic force microscopy (AFM), Figure 6.1d, was further used to precisely correlate local thickness where photo-SECCM measurements were performed.

Using Raman spectroscopy we show that more ordered films are produced up to a thickness of 10 nm, after which a second layer of disordered film grows, and that these variations in film structure influence photocurrent generation. Thus, SECCM measurements reveal that thinner, more ordered film regions, exhibit sustained photocurrent densities even after some film aging. Overall, the work herein highlights an approach for the production, screening and analysis of materials that should be widely appreciated in the future.

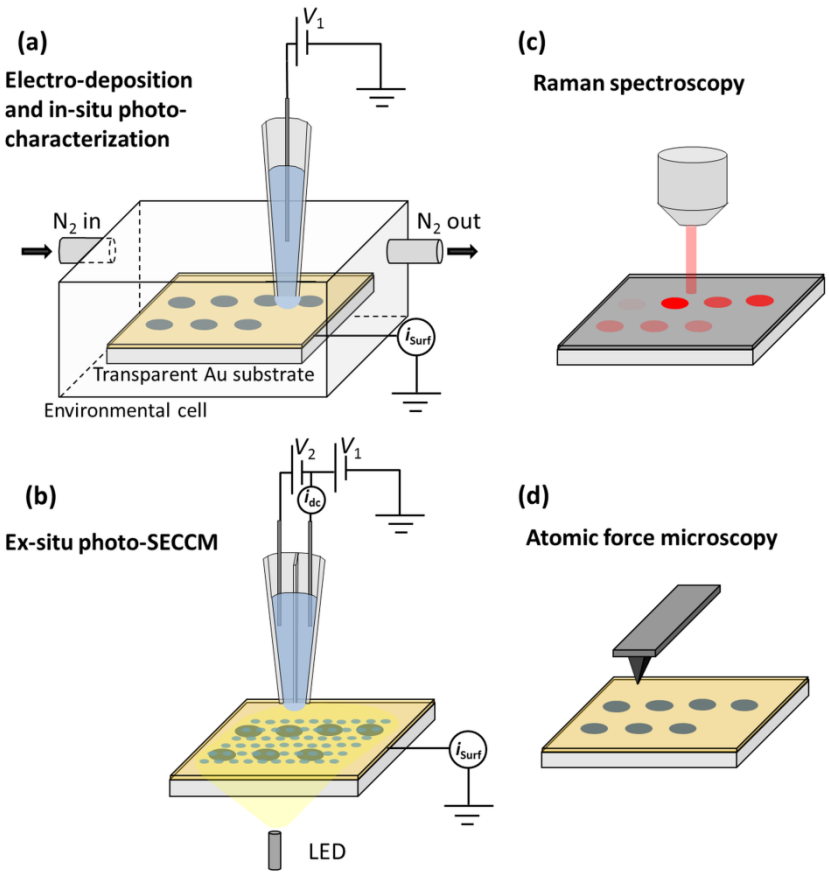

Figure 6.1 Schematic of the combinatorial multimicroscopy approach to the study of electrodeposited P3HT thin films. Single barrel scanning-droplet setup for the deposition of P3HT on a transparent gold electrode by cyclic voltammetry (a). The single barrel probe (cross section shown herein) was moved relative to the sample using a piezo-electric positioning system. Ag wire was used as a quasi-reference/counter electrode (QRCE). Scanning electrochemical cell microscopy (SECCM) set up for the ex-situ photo-electrochemical characterization of the deposited P3HT (b). Two Ag QRCEs were used in the SECCM setup. A bias (V_2) was applied between the QRCEs and the resulting conductance current across the meniscus (i_{dc}) provided the basis for positional feedback. V_1 was altered to control the potential of the substrate (V_{surf}) with the relation: $V_{Surf} = -V_1 - V_2/2$. Raman

spectroscopy (c) and atomic force microscopy (AFM) (d) were used to investigate the morphology and thickness of the deposited films.

6.2 Experimental

6.2.1 Preparation of transparent gold electrodes

Optically transparent gold electrodes on glass were prepared using a previously published method.[37] In brief, microscope glass slides (1.2 mm thick, Thermo scientific, UK) were cut to a dimension of ca. 1 cm^2 and rinsed thoroughly with ultrapure water (Milli-Q, 18.2 MΩ·cm resistivity) and isopropanol followed by washing with hot acetone vapor. The glass samples were then treated with UV-ozone for 15 minutes and, immediately after, transferred to a desiccator in which they were exposed to the vapor of a 1:1 (v/v) mixture of (3- aminopropyl)trimethoxysilane (≥ 97 % purity, Sigma Aldrich) and (3-mercaptopropyl)trimethoxysilane (≥ 95 % purity, Sigma Aldrich) at a pressure of 150 mbar for 4 hours. Gold was then evaporated on the substrates at a rate of 0.1 nm s^{-1} to form a 40 nm thick layer. Finally, the fabricated transparent gold electrodes were rinsed with isopropanol (VWR) and dried under N_2 before being used.

6.2.2 Solutions

All solutions were prepared in a supporting electrolyte consisting of a 5:1 (v/v) mixture of the room temperature ionic liquid, 1-butyl-3-methylimidazolium tetrafluoroborate ([BMIm][BF_4]), and dried acetonitrile, respectively. [BMIm][BF_4] (≥ 98.5 % purity, Sigma Aldrich) was used fresh without further treatment and

acetonitrile (≥ 99.0 % purity, Fluka) was dried overnight over molecular sieves (4 nm pore size, Fisher Scientific, UK). For the electrodeposition and in-situ photo-characterization of P3HT, the SECCM tip contained 0.1 M 3-hexylthiophene (3HT) (≥99 % purity, Sigma Aldrich) in the supporting electrolyte. For ex-situ photo-SECCM measurements, the tip contained only supporting electrolyte. All solutions were sonicated for ten minutes in an ultrasonic bath before being used to fill the probe.

6.2.3 P3HT deposition

The probes used for P3HT deposition were prepared by pulling borosilicate capillaries (Harvard Apparatus, UK) to an oval end with dimensions of 15 µm and 10 µm across on the major and minor axis (with a measured aerial footprint of 7.5×10^{-7} cm^2). After filling with electrolyte solution, an Ag wire acting as a QRCE was inserted into the capillary and the transparent gold surface was connected as the working electrode. The potential of the transparent gold surface (V_{Surf}) was controlled by altering V_1 (Figure 6.1a), i.e. $V_{Surf} = - V_1$. Deposition and in-situ characterization of the films were performed in an environmental chamber (Figure 6.1a) under continuous flow of N_2 gas to assist in drying the meniscus at the end of the probe (as the presence of water during growth produces low quality films).[26] Nitrogen gas was flowed into one side of the environmental chamber (Figure 6.1a) and out through an exit at the opposite wall. SECCM experiments were performed with a continuous nitrogen flow after being de-aerated for at least one hour.

6.2.4 Procedures and equipment for localized depositions and measurements

Initially, P3HT was locally electrodeposited by potentiodynamic methods (i.e. cyclic voltammetry) on optically transparent gold electrodes[37] using a single 'barrel' droplet probe ('tip') in a controlled environment[26,38] (see above and Figure 6.1a). Deposition of P3HT was performed by CV with a tip containing the monomer 3HT in supporting electrolyte, ensuring that the resulting film was in its un-doped form.[32] In-situ photo-electrochemical characterization was performed immediately after deposition, using the same probe (containing the 3HT monomer) and with a bottom illumination configuration (as in Figure 6.1a). Higher resolution ex-situ photo-SECCM (Figure 6.1b), employed a smaller dual-channel tip with a diameter of ~ 3 µm. Full details of the photo-SECCM setup, including tip manufacture, can be found elsewhere[26] and in Chapter 5, section 5.2.3. In essence, a series of pre-defined localized photocurrent transient spot measurements in the *xy* plane were performed (referred to as a 'hopping' scan).

6.2.5 Atomic force microscopy (AFM)

AFM measurements were carried out in tapping mode on a Veeco Enviroscope AFM with a Nanoscope IV controller.

6.2.6 Raman microscopy

Raman spectra were recorded with an excitation wavelength of 633 nm using a HeNe laser microRaman (Renishaw inVia, UK) with an output power of 17 mW. The spot size of the Raman laser was ~ 5 µm in diameter. Acquisition was performed at 5 % power with an integration time of 5 seconds and 5 accumulations

per spot measurement. A Si single crystal sample was used for calibration prior to measurements.

6.2.7 Photo-SECCM scan parameters and data acquisition

Hopping mode scans consisted of a series of approach/retract measurements arranged in a rectangular array at predefined locations in the *xy* plane of the sample. Each approach/retract measurement is referred to as a 'hop'. In order to avoid overlapping of hop measurements, the hopping scans were performed with a separation of 6 µm between each point in the *xy* plane, using a probe with a tip diameter (2.4 µm) that was smaller than the hopping distance. A bias of + 0.15 V was applied between the QRCEs. The surface was detected with a rapid change in the alternating component of i_{dc} due to the droplet formation and tip height modulation. The tip movement in the *z* direction was then halted and a hold time of 5 seconds was maintained. After the initial dark hold time, the LED was turned on for photocurrent measurements for 5 seconds. The tip was then retracted and moved to the next hop.

Data points were the average of 1024 acquisition periods of 4 µs per data point (corresponding to an acquisition time of ca. 4 ms per data point). In the ex-situ photo-SECCM hopping scan, the piezoelectric positioner movement was set to a speed of 1 µm s^{-1}. The hopping distance was fixed at 6 µm in both *x* and *y* coordinates and a retraction distance of 7 µm in the *z* axis (height) set after each hop measurement. The scan area was a 60 × 90 µm corresponding to 176 hop measurements (16 hops in the *x* direction for each of the 11 rows in the *y* direction).

6.3 Results and discussion

6.3.1 Electrodeposition and thickness of P3HT on transparent gold electrodes

P3HT films were grown on a transparent gold electrode using a CV deposition method, where increasing the number of CV cycles increased the amount of film deposited on the electrode. Initially, the tip was positioned just above the transparent gold surface with the aid of an optical camera. The tip was then approached to the surface utilizing the piezoelectric positioning block and using the initial surface charging current (i_{Surf}, in Figure 6.1b) as feedback to make initial meniscus contact, without the tip physically contacting the surface. Following meniscus contact with the substrate, films were produced by electropolymerization of 3HT on the working electrode surface by sweeping the working electrode potential in the anodic direction from 0. 00 V up to + 1.35 V vs Ag QRCE (scan rate: 0.1 V s^{-1}). An anodic potential limit of + 1.35 V was used to minimize film degradation at higher overpotentials.[32] Sweeping back in the cathodic direction, the potential cycle ended at 0.00 V vs Ag QRCE to ensure the film was in an un-doped state at the end of the deposition procedure.[32] A typical CV (for a film produced with 4 deposition cycles) is shown in Figure 6.2.

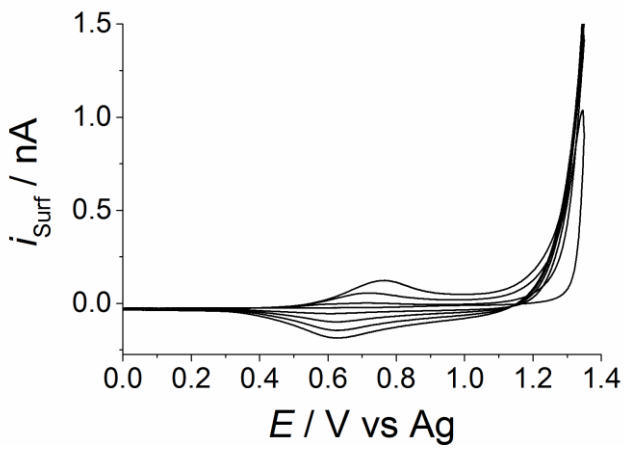

Figure 6.2 Cyclic voltammogram for the deposition of P3HT using a microcapillary. The initial applied potential was 0.00 V *vs.* Ag QRCE and the sweep rate was 0.1 V s^{-1}. Maximum anodic potential was 1.35 V vs Ag QRCE and the cathodic sweep finished at 0.00 V *vs.* Ag QRCE. 4 cycles are shown. The tip contained 0.1 M 3HT in a 5:1 mixture of [BMIm][BF_4] and dried acetonitrile, respectively.

7 types of film (individually referred here to as 'deposition spots') were produced for the study herein. The typical deposition sequence used was: 3, 2, 5, 4, 8, 10, and 6 voltammetric deposition cycles for each type of spot, to eliminate any possible time dependence of the deposition process. At the end of each deposition the tip meniscus remained on the surface, with the substrate electrode potential at 0.00 V vs Ag QRCE for 60 seconds and then in-situ photo-characterization was performed on the fresh film immediately before moving to the next deposition spot.

In order to verify that the photocurrent response in in-situ measurements was not affected by the presence of the monomer 3HT, blank photocurrent response measurements were performed on the gold substrate where no film was electrodeposited (Figure 6.3). No contribution from the monomer is exhibited.

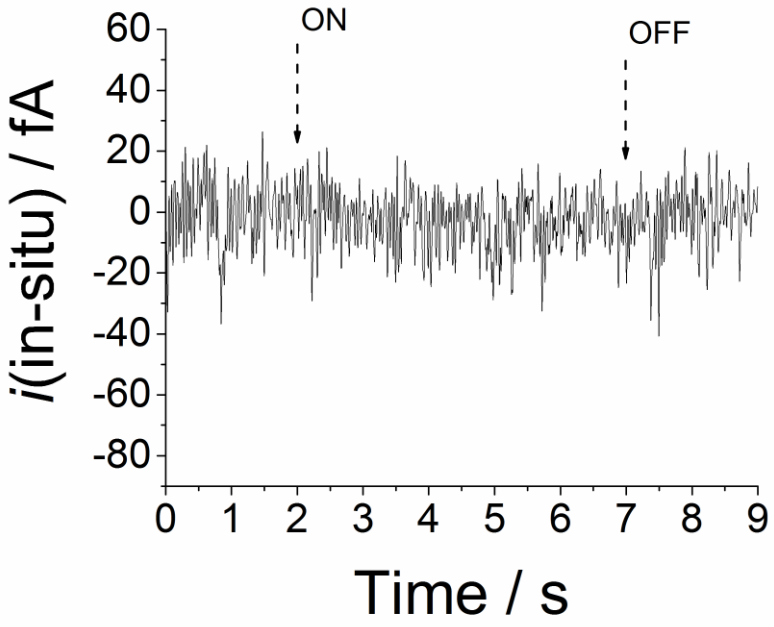

Figure 6.3 Control in-situ photocurrent transients on a gold substrate where no P3HT film was deposited. Only the last 2 seconds in the dark, before the 5 s illumination period and the first 2 seconds after illumination was switched off are shown. The probe contained 0.1 M 3HT in a 5:1 (v/v) mixture of [BMIm][BF_4] and dried acetonitrile, respectively and the surface was held at 0.00 V vs Ag QRCE.

Thus no photocurrent was observed for pipettes containing monomer unless a film was deposited onto the working electrode substrate, and so the photo-responses reported can be assigned to the polymer.

6.3.2 In-situ photo-characterization

As mentioned above, in order to characterize the pristine deposited films (in-situ) the same tip used for deposition was used for photo-characterization without losing meniscus contact with the freshly deposited film. For in-situ photocurrent measurements, the substrate electrode was held at a potential of 0.00 V vs Ag QRCE. The LED intensity was fixed to a value of 33 mW cm^{-2} and was switched on and off periodically for a duration of 5 seconds for each of the light and dark segments. This process was repeated for a period of 300 seconds (corresponding to 30 photocurrent transients).

Upon illumination a photocurrent was observed, due to the reduction of dissolved oxygen[26,39,40] and a typical experiment with all 30 transients (for a film produced with 4 deposition cycles) is shown in Figure 6.4a. The photocurrent response in Figure 6.4a exhibits a decrease of approximately 20% in intensity from the first transients to the last, highlighting that the films suffer from significant photo-degradation. However, the last 10 photocurrent transients were reproducible and thus for the quantitative comparison between films (vide infra), average values over multiple transients were used.

Typical in-situ photocurrent transients for the different electrodeposited films (3^{rd} transient of a sequence in each case, with other transients showing similar effects) are shown in Figure 6.4b. The (photo)reduction current density, *j*(in-situ), increases with an increasing number of deposition cycles reaching a maximum at

about 4-5 deposition cycles. Further deposition cycles did not result in an increase of photo-response as seen from the transients for P3HT films deposited with more than 6 deposition cycles in Figure 6.4c.

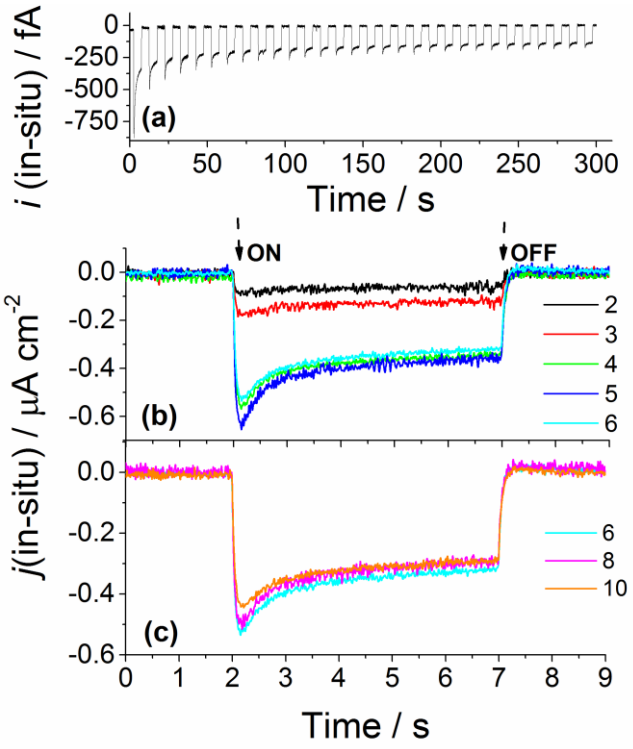

Figure 6.4 – In-situ photocurrent transients. (a) Typical series of 30 photocurrent transients for an electrodeposited P3HT film (produced by4 deposition cycles). (b) Overlay of typical in-situ photocurrent transients (3rd transient of a series in each case) for electrodeposited P3HT films produced between 2 and 6 deposition cycles. (c) Overlay of in-situ photocurrent transients (3rd transient of a series in each case) for films produced by 6,8 and 10 CV cycles. The last 2 seconds in the dark, before the 5 s illumination period and the first 2 seconds after illumination was switched off are shown in (b) and (c). The key in (b) and (c) shows the number of deposition cycles employed for film formation. The probe in all experiments contained 0.1 M

3HT in a 5:1 (v/v) mixture of [BMIm][BF_4] and dried acetonitrile, respectively, and the substrate electrode potential was 0.00 V vs Ag QRCE.

6.3.3 Correlation of film thickness and in-situ photo-response

Following growth, and in-situ photoelectrochemical measurements, the sample was rinsed thoroughly with dried acetonitrile and AFM images were recorded for each deposit. The deposits had an aerial footprint matching those of the tip dimension used for electrodeposition (7.5×10^{-7} cm^2). The thickness of the deposits reached a maximum value, roughly at the center of the deposit and the average thickness of the deposits is plotted against the number of CV deposition cycles in Figure 6.5. The average film thickness and standard deviation of the elliptical deposited P3HT films for the correlation of in-situ photocurrent response measurements was calculated by averaging the AFM line sections across the major and minor axes of each deposit (passing through the center). For each deposit the same section length was used. An increase in the average film thickness, as well as film roughness (evident from the increase in standard deviation in film thickness), was observed with increasing number of deposition cycles, verifying that the CV method is suitable for varying the film thickness.

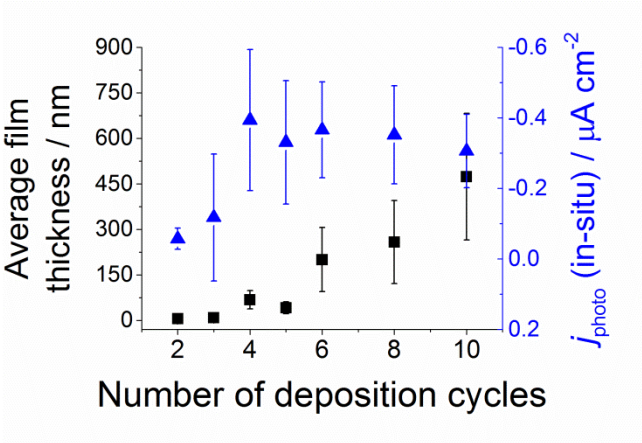

Figure 6.5 Average P3HT film thickness (black ■) and in-situ photocurrent density (blue ▲) as function of number of CV deposition cycles. The error bars represent one standard deviation.

In order to identify any relationship between the average film thickness and photo-activity, the in-situ photocurrent density, j_{photo} (in-situ), (defined as the average difference between the maximum photocurrent density and the background dark current of all 30 transients for each film, described above) was overlaid with average film thickness as a function of the number of deposition cycles in Figure 6.5. It can be seen that as the film thickness increased up to about 70 nm, j_{photo} (in-situ) also increased to a maximum value of - 0.39 µA cm^{-2}, after which, j_{photo} (in-situ) appeared to slightly decrease with increasing film thickness (number of deposition cycles).

In order to establish the factors limiting the photocurrent response, we consider the various steps leading to charge transport through the film.[41] Starting with the absorption of light, an estimation of the penetration depth through the film, *d*, (defined as $1/\alpha$, where α is the absorption coefficient for P3HT) provides the optimum film thickness for the maximum photocurrent (if absorption was the

limiting factor). α is typically in the order of 10^5 to 10^4 cm^{-1}, corresponding to a penetration depth, *d*, in the range of several 100's of nm.[42,43] Thus, the decrease and plateauing of photocurrent response after about 40 nm film thickness (Figure 6.5) cannot be attributed to attenuation of the light intensity by absorption in thicker films alone. This may suggest that the photocurrent response is limited by exciton diffusion within individual P3HT grains to the nearest solid-liquid interface which is estimated in the literature to be ≤ 10 nm.[44] However, for the in-situ measurements, the electrolyte is in contact with all grains (from the supporting gold electrode to the top surface of the film) which are reported to be < 20 nm in the case of electrochemically grown polymers[32] (taken herein, as an upper case limit) and can readily travel to an interface where charge separation occurs. Thus, the most probable limitation is transport of charge carriers (hole mobility) through the P3HT film. Raman spectroscopy was utilized to examine the structural order of the deposited films, which is known to correlate with charge mobility.[41,45]

6.3.4 Raman spectroscopy of P3HT deposits

Raman intensities of conjugated carbon bonds are usually high,[46] which is an advantage for characterizing small amounts of organic materials. Raman spectra for the electrodeposited films were recorded and a typical spectrum (for the ca. 40 nm thick film) is shown in Figure 6.6a. P3HT exhibits six bands in this spectral region, with some of them overlapping. The most intense band at 1446 cm^{-1} is related to the symmetric stretching of the $C_\alpha=C_\beta$ bond of the thiophene ring[47] and the band at 1379 cm^{-1} is characteristic of the skeletal symmetric stretching related to the intraring $C_\beta-C_{\beta'}$ bond. In addition, two bands ascribed to interring deformations are observed

around 1200 cm^{-1}: (i) the C_{α}–$C_{\alpha'}$ symmetric stretching combined with C_{β}–H bending, assigned to 1205 cm^{-1}, and (ii) the 1180 cm^{-1}, related to C_{α}–$C_{\alpha'}$ antisymmetric stretching and $C_{\beta+}$–H bending. Finally, the small band at 1089 cm^{-1} appears due to the C_{β}–H bending.[48,49] The C_{α}=C_{β} mode has been used previously to quantify the degree of molecular order of P3HT by studying the superposition of both ordered and disordered P3HT phase peaks. [47,50,51] In addition, the C_{α}=C_{β} Raman band is sensitive to the extent of π-electron delocalization and P3HT morphology and order. It shows narrow full width half maximum (FWHM) for crystalline P3HT (where rings are closely stacked and ordered).[52]

The Raman spectral regions around ~1446 cm^{-1} (C_{α}=C_{β} band) for the entire set of electrodeposited films are compared in Figure 6.6b, with the average film thickness assigned. A clear broadening of the C_{α}=C_{β} band, together with a shifting from ~1446 cm^{-1} towards 1452 cm^{-1}, is observed for films thicker than 68 nm. The FWHM shows a significant change from ~30 cm^{-1} for films < 68 nm in thickness to ~60 cm^{-1} for films > 200 nm. The broadening of the C_{α}=C_{β} band indicates a decrease in the crystallinity of the P3HT films.[53] Further evidence for film disorder is seen in the blue shift of the C_{α}=C_{β} Raman band, which could be due to: shorter conjugation lengths,[47] less planarity,[54] and a non-optimal π-stacking of adjacent polymer chains.[55] Thus, broadly speaking, two types of films can be formed by electrodeposition: (i) ordered films with narrow Raman bands centered at 1446 cm^{-1} and (ii) films exhibiting a level of disorder indicated by the broadening of the FWHM and the blue shifting of the band center from 1446 cm^{-1} to 1452 cm^{-1}.

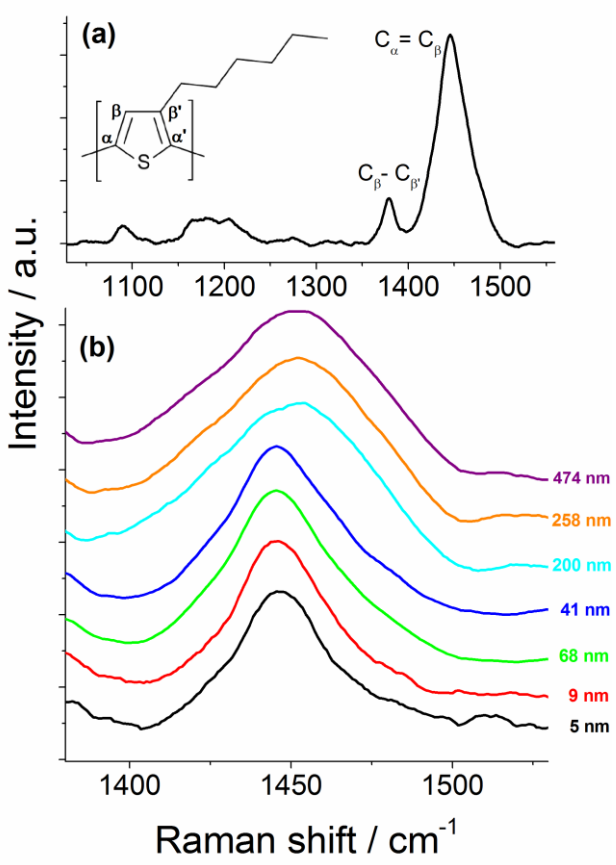

Figure 6.6 Raman spectra of electrodeposited P3HT films on a transparent gold electrode. Spectrum of a P3HT film deposited with 5 electrodeposition cycles (a). The chemical structure of P3HT is shown in the inset and the main bands are assigned to the symmetric $C_\alpha=C_\beta$ stretching of the thiophene ring and to intraring $C_\beta-C_{\beta'}$ skeletal symmetric stretching at 1446 cm^{-1} and 1379 cm^{-1}, respectively. Normalized Raman spectra around the $C_\alpha=C_\beta$ stretching for all the deposited films (b). The average thickness of the corresponding films is shown on the right hand side of each spectrum.

To summarize and allow direct comparison of the in-situ photo-response and Raman trends, j_{photo} (in-situ) and the FWHM of the $C_\alpha=C_\beta$ Raman band are plotted as a function of average film thickness in Figure 6.7. The photo-activity trend is clearly

correlated to the shifting of the C_α=C_β Raman band and the broadening of the FWHM, corresponding to the two types of P3HT film identified above. Thus, films thinner than 9 nm exhibited a higher degree of structural order across the entire film whereas thicker films (> 200 nm) exhibited a blue-shifting and broadening of the C_α=C_β Raman peak indicating a greater degree of disorder. An intermediate case was seen for the films with an average thickness of 41 and 68 nm where the FWHM is suggested to broaden due to the initial growth of disordered film on top of the thin layer of ordered film. This is consistent with previous AFM studies of electrodeposited polythiophene thin films where it was observed that initially a thin ordered film was created up to 5 nm,[56] with continued growth leading to the formation of a more amorphous material for increasing film thickness.

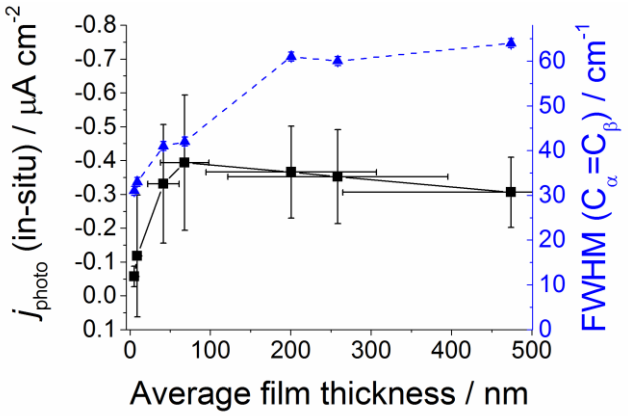

Figure 6.7 In-situ photo-activity (black ■) and FWHM of the C_α = C_β Raman band (blue ▲) of deposited P3HT films as function of average film thickness. Error bars represent the standard deviation of the measured properties.

6.3.5 Local ex-situ SECCM photo-characterization

To access local differences within electrodeposited spots, ex-situ photo-SECCM measurements were carried out and photo-transients at different locations of single P3HT film deposits were recorded. For this purpose, after deposition and in-situ characterization, P3HT films were rinsed thoroughly with acetonitrile and a series of photo-SECCM approach/retract measurements were performed with a ~ 3 µm diameter probe (see below) containing only supporting electrolyte over an area of 60 µm × 90 µm.

The hopping distance between adjacent approach/retract measurements was set to 6 µm (larger than the tip diameter) in both, the *x* and *y* direction of the scan (corresponding to 176 measurements). This distance avoided spatial overlap between hops, and for the probe meniscus to contact a single deposited film at multiple locations. For each position, a dark measurement of 5 seconds followed by 5 seconds under LED illumination was recorded upon contact with the surface. SECCM feedback[27,28,30] was used for surface detection, ensuring a comparable meniscus contact area for each hop measurement. The meniscus contact area was further verified by analysis of field emission scanning electron microscopy (FE-SEM) images (vide infra). Three ex-situ photo-SECCM scans were performed on the same area on different days with probes of slightly different sizes (2.4, 3.1 and 3.5 µm in diameter, see AFM below) and showed reproducible current densities indicating minimal changes in activity that might have occurred due to further degradation and film aging.

A FE-SEM of the scan area with all film deposits is shown in Figure 6.8a where the number of deposition cycles employed for the electrodeposition of P3HT is marked in white font. A trace of ionic liquid from the scanning probe was left after each hop and the overlapping of the traces from the three scans can be clearly seen on the gold substrate, assisting in directly identifying the specific location of any given meniscus. Moreover, the aerial footprint of the probe was determined from analysis of the images of these residues for the three ex-situ hopping scans.

From the FE-SEM images of individual P3HT deposits (Figure 6.8a) it is evident that the ex-situ SECCM probe had at least one point of full contact with all deposits (except for that produced with 2 deposition cycles). In order to perform quantitative analysis, only data that corresponded to a full contact with the film were considered (taking into account the precise aerial footprint of the SECCM probe). For most of the P3HT films, 2 full contact spots with the ex-situ photo-SECCM probe were observed.

AFM images of each of the individual deposited films were also recorded (before FE-SEM imaging) and an example for the film produced from 4 deposition cycles (highlighted in a dashed white box in Figure 6.8a) is shown in Figure 6.8b. The two ex-situ SECCM contact spots used for analysis are marked (to guide the eye) and the corresponding line profiles are shown in Figure 6.8c, exhibiting clearly the marks of residual electrolyte from the SECCM probe, which is thin (and barely

changes the local film height) but detectable. The position of meniscus contact with the film for the measurement marked ‘i’ is roughly at the top of the film corresponding to a thickness of ~ 80 nm (measured with respect to the substrate), whereas, the position of the measurement marked ‘ii’ is on a slope at the foot of the film corresponding to an average of ~ 40 nm. In the cases where the SECCM probe landed on a sloped film, the film height was taken as the average of the maximum and minimum height, measured at the base of the residue footprint. The impact of these subtle localized differences in film thickness were readily detected by ex-situ photo SECCM measurements (Figure 6.8d), where the corresponding photo-transients of positions ‘i’ and ‘ii’ are marked. The largest photo-response recorded in the hopping scan was roughly - 0.25 µA cm^{-2}, corresponding to a 7 nm height (film produced with 3 deposition cycles), and the photo-transient is shown in black line in Figure 6.8d.

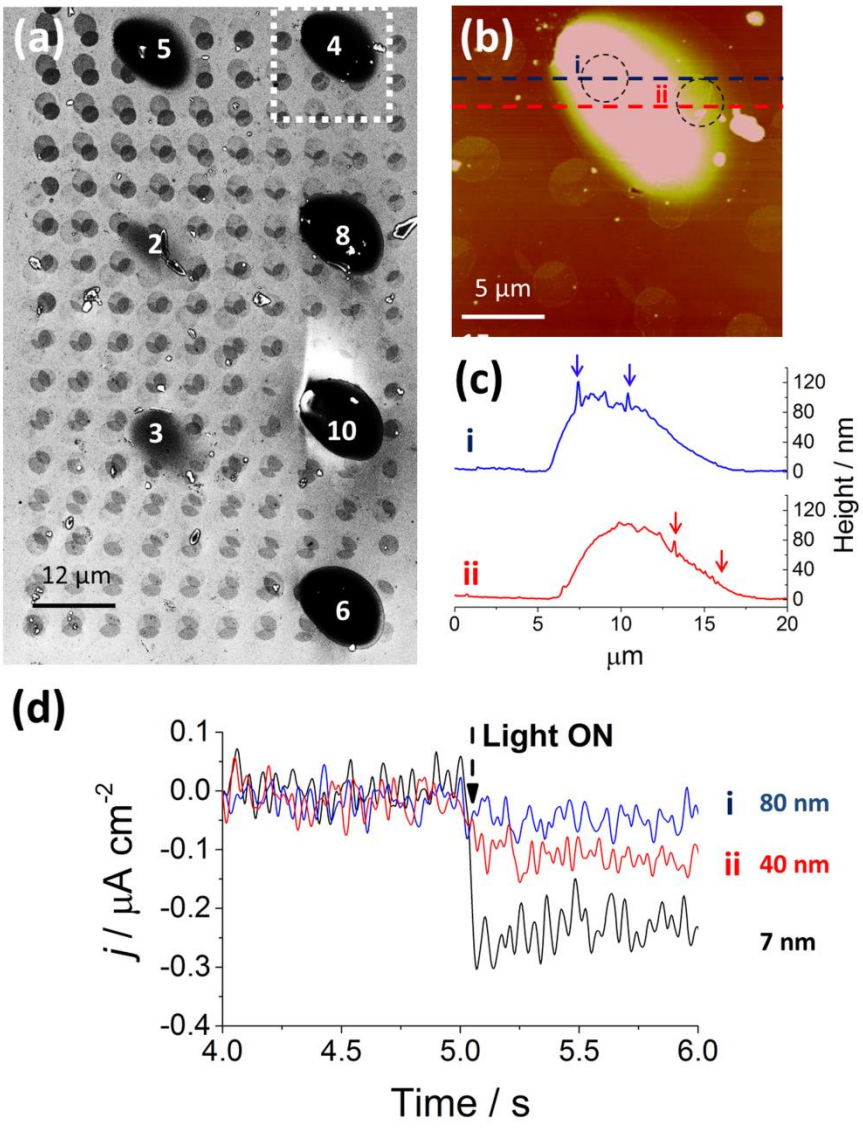

Figure 6.8 – FE-SEM, AFM and ex-situ SECCM photo-transients of electrodeposited P3HT films. FE-SEM image of the deposited P3HT films after three ex-situ photo-SECCM scans (a), where the numbers in white font correspond to the number of cycles employed for P3HT deposition. The traces of the scanning probes are clearly seen and assist in locating the spatial position of the photo-measurements. AFM image of the boxed area shown in (a), corresponding to a P3HT film produced by 4 deposition cycles (b). The traces of electrolyte from ex-situ SECCM measurements on the P3HT film are marked with dashed black circles to

guide the eye. The blue (i) and red (ii) dotted AFM line profiles are shown in (c) with arrows indicating the rims of the SECCM probe contact area. Photo-transients (last second in the dark and first second under illumination) of the spots shown in (b) and (c), including the thinnest film measured (d).

To examine the general trend displayed by the ex-situ photo-SECCM measurements, the photocurrent response was plotted as a function of film thickness for films produced up to 100 nm thick from all three ex-situ hopping scans (shown in Figure 6.9). The entire set of data for the ex-situ photo-SECCM experiments, with the minimum and maximum film heights for each spot is available in Table 6.1. j_{photo}(ex-situ), was defined as the difference in the average j_{Surf} during the entire illumination period (5 s) and that of the last 40 ms under dark conditions. Two significant observations can be made: (i) the measured ex-situ photocurrent densities are generally lower than those measured in-situ for film deposits greater than 40 nm, and (ii) there is a significant decrease in photo-activity with film thickness for films thicker than ~ 10 nm.

Table 6.1 Full range of data used for quantitative analysis of ex-situ photo SECCM measurements.

Average thickness /nm	minimum	maximum	j_{photo} (ex-situ) / µA cm^{-2}
5.5	5	6	-0.081
5.5	4	7	-0.188
7	6	8	-0.111
7.5	7	8	-0.236
46	37	55	-0.045
49	44	54	-0.020
62.5	53	72	-0.068
82	76	88	-0.047
88.5	82	95	-0.054
154.5	67	242	-0.052
207.5	190	225	-0.073
232.5	185	280	-0.088
276.5	233	320	-0.072
315.5	284	347	-0.061
370	319	421	-0.022
487	453	521	-0.047
497.5	453	542	-0.054
560.5	500	621	-0.050
650	600	700	-0.044

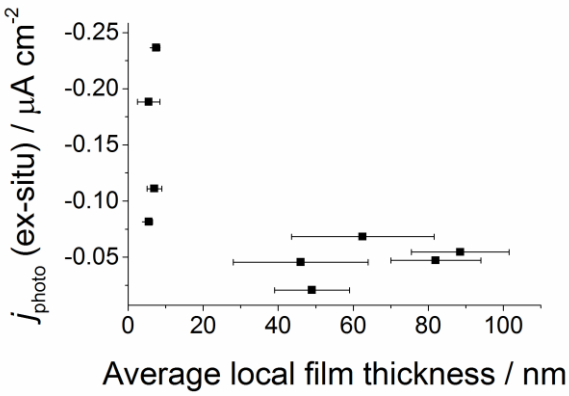

Figure 6.9 Ex-situ photo-SECCM photocurrent densities as a function of P3HT average local film thickness. Error bars are constructed from the minimum and maximum thickness measured at the location of the ex-situ photo-SECCM spot measurement.

A plausible reason for the lower current densities in some of the ex-situ measurements is photo-degradation of P3HT films over time.[57,58] Ex-situ experiments were typically performed three days after electrodeposition and in-situ characterization experiments. Interestingly, however, for films with a thickness < 10 nm, the difference between photocurrent densities from in-situ and ex-situ measurements was negligible, suggesting that the more ordered thin films are less prone to degradation, compared to the more disordered thicker films. This is consistent with a recent report showing that chemically prepared regiorandom P3HT, which exhibits decreased film order, also showed much more rapid degradation than the more ordered regioregular P3HT.[58] It is further important to point out that the photocurrent density from all three ex-situ SECCM scans (typically performed with a two day period between each) were very similar; therefore degradation between SECCM ex-situ scans can be assumed to be negligible.

The striking difference in observed trends of photocurrent densities versus film thickness between in-situ and ex-situ measurements (Figure 6.7 and Figure 6.9, respectively) is suggested to stem from the nature of the meniscus contact, illustrated in Figure 6.10. For in-situ measurements (Figure 6.10a), the solution is in contact with the entire bulk of the film giving rise to contributions from both ordered and disordered portions of the film. Because the electrolyte is inherently in contact with grains throughout the bulk of the film the photocurrent is not limited by the exciton diffusion length but, instead, depends on the hole mobility through the film. In contrast, for ex-situ measurements (Figure 6.10b) the probe only contacts the top of the P3HT film surface, becoming limited by the diffusion of excitons to the polymer film/solution interface for films greater than 10 nm in thickness. This is evident from the drop off in ex-situ photocurrent response for films greater than 8 nm in Figure 6.9. That ex-situ measurements probe only the top surface is further supported by analysis of the AFM images of the probes footprint on the deposits (Figure 6.8b) where negligible spreading is exhibited, suggesting minimal penetration into the P3HT film.

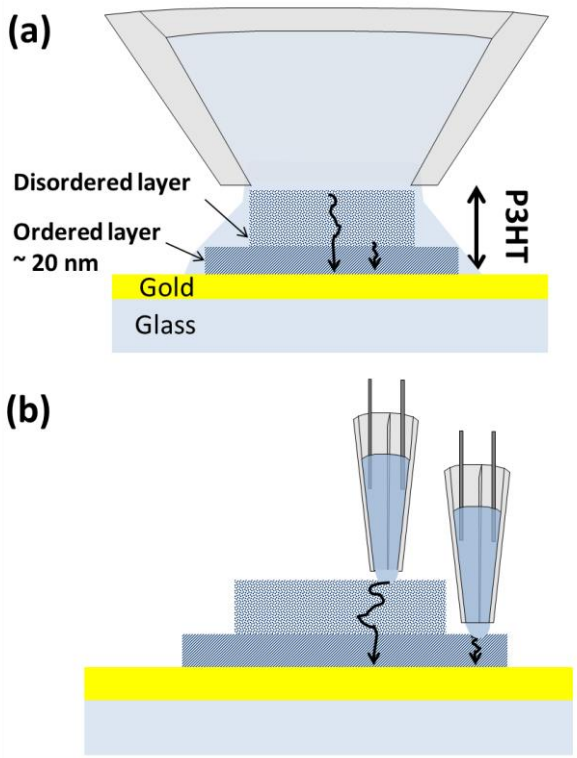

Figure 6.10 Schematics (not to scale) of meniscus contact for in-situ (a) and ex-situ (b) photo-SECCM measurements. In ex-situ measurements the film is accessed from the top layer and is therefore, for thicker films, limited by charge transport through the disordered film.

6.4 Conclusions

A correlation of film morphology and photo-activity for the reduction of dissolved oxygen in an organic photoelectrochemical cell configuration was obtained for electrodeposited P3HT films on a transparent gold electrode using a multimicroscopy photo-SECCM platform. The platform allows both the electrochemical deposition of material and photo-characterization (in-situ and ex-situ) in the same configuration. For the illustrative case of P3HT, ordered thin films (identified by Raman peak centers and FWHM of the C_α=C_β Raman band at 1446

cm^{-1}) exhibited the highest photo-activity. However, ex-situ measurements highlighted that subtle variations in film thickness and morphology contribute to a significant change in photo-activity of the films, especially after some aging. The platform opens access to the screening of electrodeposited thin films prepared in-situ, combined with sensitive localized (photo)-activity measurements, as highlighted by the ex-situ photo-SECCM experiment where it was possible to map variations in activity across, (within) a deposit. Finally, it has been illustrated that the platform is able to extract valuable information on growth and degradation processes for which improved knowledge is needed in the search for optimized materials.

6.5 References

(1) Hoffmann, M. R.; Martin, S. T.; Choi, W.; Bahnemann, D. W. *Chem. Rev.* **1995**, *95*, 69.

(2) Sivula, K. *J. Phys. Chem. Lett.* **2013**, *4*, 1624.

(3) Yu, Z.; Li, F.; Sun, L. *Energy Environ. Sci.* **2015**, *8*, 760.

(4) Alibabaei, L.; Brennaman, M. K.; Norris, M. R.; Kalanyan, B.; Song, W.; Losego, M. D.; Concepcion, J. J.; Binstead, R. A.; Parsons, G. N.; Meyer, T. J. *Proceedings of the National Academy of Sciences* **2013**, *110*, 20008.

(5) Wang, Y.; Sun, T.; Yang, D.; Liu, H.; Zhang, H.; Yao, X.; Zhao, H. *Phys. Chem. Chem. Phys.* **2012**, *14*, 2333.

(6) Sirringhaus, H.; Brown, P. J.; Friend, R. H.; Nielsen, M. M.; Bechgaard, K.; Langeveld-Voss, B. M. W.; Spiering, A. J. H.; Janssen, R. A. J.; Meijer, E. W.; Herwig, P.; de Leeuw, D. M. *Nature* **1999**, *401*, 685.

(7) Kline, R. J.; McGehee, M. D.; Kadnikova, E. N.; Liu, J.; Fréchet, J. M. J.; Toney, M. F. *Macromolecules* **2005**, *38*, 3312.

(8) Roncali, J.; Yassar, A.; Garnier, F. *Synth. Met.* **1989**, *28*, 275.

(9) Guerrero, A.; Haro, M.; Bellani, S.; Antognazza, M. R.; Meda, L.; Gimenez, S.; Bisquert, J. *Energy Environ. Sci.* **2014**, *7*, 3666.

(10) Haro, M.; Solis, C.; Molina, G.; Otero, L.; Bisquert, J.; Gimenez, S.; Guerrero, A. *J. Phys. Chem. C* **2015**, *119*, 6488.

(11) Gazotti, W. A.; Girotto, E. M.; Nogueira, A. F.; De Paoli, M. A. *Sol. Energy Mater. Sol. Cells* **2001**, *69*, 315.

(12) Zhang, Y.; Mao, F.; Yan, H.; Liu, K.; Cao, H.; Wu, J.; Xiao, D. *J. Mater. Chem. A* **2015**, *3*, 109.

(13) Bard, A.; Lee, H. C.; Leonard, K.; Park, H. S.; Wang, S. In *Photoelectrochemical Water Splitting: Materials, Processes and Architectures*; The Royal Society of Chemistry: 2013, p 132.

(14) Haram, S. K.; Bard, A. J. *J. Phys. Chem. B* **2001**, *105*, 8192.

(15) Yuan, D.; Xiao, L.; Jia, J.; Zhang, J.; Han, L.; Li, P.; Mao, B.-W.; Zhan, D. *Anal. Chem.* **2014**, *86*, 11972.

(16) Park, H. S.; Leonard, K. C.; Bard, A. J. *J. Phys. Chem. C* **2013**, *117*, 12093.

(17) Lee, J.; Ye, H.; Pan, S.; Bard, A. J. *Anal. Chem.* **2008**, *80*, 7445.

(18) Kollender, J. P.; Mardare, A. I.; Hassel, A. W. *ACS Combinatorial Science* **2013**, *15*, 601.

(19) Kollender, J. P.; Gasiorowski, J.; Sariciftci, N. S.; Mardare, A. I.; Hassel, A. W. *J. Phys. Chem. C* **2014**, *118*, 16919.

(20) Gasiorowski, J.; Kollender, J. P.; Hingerl, K.; Sariciftci, N. S.; Mardare, A. I.; Hassel, A. W. *Phys. Chem. Chem. Phys.* **2014**, *16*, 3739.

(21) Kollender, J. P.; Mardare, A. I.; Hassel, A. W. *ChemPhysChem* **2013**, *14*, 560.

(22) Aydemir, N.; Parcell, J.; Laslau, C.; Nieuwoudt, M.; Williams, D. E.; Travas-Sejdic, J. *Macromol. Rapid Commun.* **2013**, *34*, 1296.

(23) Laslau, C.; Williams, D. E.; Travas-Sejdic, J. *Prog. Polym. Sci.* **2012**, *37*, 1177.

(24) Laslau, C.; Williams, D. E.; Kannan, B.; Travas-Sejdic, J. *Adv. Funct. Mater.* **2011**, *21*, 4607.

(25) Zhang, J.; Barker, A. L.; Mandler, D.; Unwin, P. R. *J. Am. Chem. Soc.* **2003**, *125*, 9312.

(26) Aaronson, B. D. B.; Byers, J. C.; Colburn, A. W.; McKelvey, K.; Unwin, P. R. *Anal. Chem.* **2015**, *87*, 4129.

(27) Ebejer, N.; Güell, A. G.; Lai, S. C. S.; McKelvey, K.; Snowden, M. E.; Unwin, P. R. *Annu. Rev. Anal. Chem.* **2013**, *6*, 329.

(28) Snowden, M. E.; Güell, A. G.; Lai, S. C. S.; McKelvey, K.; Ebejer, N.; O'Connell, M. A.; Colburn, A. W.; Unwin, P. R. *Anal. Chem.* **2012**, *84*, 2483.

(29) Ebejer, N.; Schnippering, M.; Colburn, A. W.; Edwards, M. A.; Unwin, P. R. *Anal. Chem.* **2010**, *82*, 9141.

(30) Aaronson, B. D. B.; Güell, A. G.; McKelvey, K.; Momotenko, D.; Unwin, P. R. In *Nanoelectrochemistry*; Mirkin, M. V., Amemiya, S., Eds.; CRC Press: 2015, p 655.

(31) Dang, M. T.; Hirsch, L.; Wantz, G. *Adv. Mater.* **2011**, *23*, 3597.

(32) Ratcliff, E. L.; Jenkins, J. L.; Nebesny, K.; Armstrong, N. R. *Chem. Mater.* **2008**, *20*, 5796.

(33) Ballantyne, A. M.; Ferenczi, T. A. M.; Campoy-Quiles, M.; Clarke, T. M.; Maurano, A.; Wong, K. H.; Zhang, W.; Stingelin-Stutzmann, N.; Kim, J.-S.; Bradley, D. D. C.; Durrant, J. R.; McCulloch, I.; Heeney, M.; Nelson, J.; Tierney, S.; Duffy, W.; Mueller, C.; Smith, P. *Macromolecules* **2010**, *43*, 1169.

(34) Gao, J.; Thomas, A. K.; Johnson, R.; Guo, H.; Grey, J. K. *Chem. Mater.* **2014**, *26*, 4395.

(35) Xue, L.; Li, W.; Hoffmann, G. G.; Goossens, J. G. P.; Loos, J.; de With, G. *Macromolecules* **2011**, *44*, 2852.

(36) Stuart, B. H. *Vib. Spectrosc.* **1996**, *10*, 79.

(37) Stec, H. M.; Hatton, R. A. *Adv. Energy Mater.* **2013**, *3*, 193.

(38) Aaronson, B. D. B.; Lai, S. C. S.; Unwin, P. R. *Langmuir* **2014**, *30*, 1915.

(39) Byers, J. C.; Ballantyne, S.; Rodionov, K.; Mann, A.; Semenikhin, O. A. *ACS Appl. Mater. Interfaces* **2011**, *3*, 392.

(40) Byers, J. C.; DiCarmine, P. M.; Moustafa, M. M. A. R.; Wang, X.; Pagenkopf, B. L.; Semenikhin, O. A. *J. Phys. Chem. B* **2009**, *113*, 15715.

(41) Liu, C.-Y.; Chen, S.-A. *Macromol. Rapid Commun.* **2007**, *28*, 1743.

(42) Kim, Y.; Cook, S.; Tuladhar, S. M.; Choulis, S. A.; Nelson, J.; Durrant, J. R.; Bradley, D. D. C.; Giles, M.; McCulloch, I.; Ha, C.-S.; Ree, M. *Nat Mater* **2006**, *5*, 197.

(43) Erb, T.; Zhokhavets, U.; Gobsch, G.; Raleva, S.; Stühn, B.; Schilinsky, P.; Waldauf, C.; Brabec, C. J. *Adv. Funct. Mater.* **2005**, *15*, 1193.

(44) Shaw, P. E.; Ruseckas, A.; Samuel, I. D. W. *Adv. Mater.* **2008**, *20*, 3516.

(45) Joshi, S.; Grigorian, S.; Pietsch, U.; Pingel, P.; Zen, A.; Neher, D.; Scherf, U. *Macromolecules* **2008**, *41*, 6800.

(46) Chunder, A.; Liu, J.; Zhai, L. *Macromol. Rapid Commun.* **2010**, *31*, 380.

(47) Carach, C.; Gordon, M. J. *J. Phys. Chem. B* **2013**, *117*, 1950.

(48) Baibarac, M.; Lapkowski, M.; Pron, A.; Lefrant, S.; Baltog, I. *J. Raman Spectrosc.* **1998**, *29*, 825.

(49) Trznadel, M.; Zagorska, M.; Lapkowski, M.; Louarn, G.; Lefrant, S.; Pron, A. *J. Chem. Soc., Faraday Trans.* **1996**, *92*, 1387.

(50) Li, Z.; Sun, S.; Li, X.; Schlaf, R. *Appl. Phys. Lett.* **2014**, *104*.

(51) Tsoi, W. C.; James, D. T.; Kim, J. S.; Nicholson, P. G.; Murphy, C. E.; Bradley, D. D. C.; Nelson, J.; Kim, J.-S. *J. Am. Chem. Soc.* **2011**, *133*, 9834.

(52) Meyer, M. W.; Larson, K. L.; Mahadevapuram, R. C.; Lesoine, M. D.; Carr, J. A.; Chaudhary, S.; Smith, E. A. *ACS Appl. Mater. Interfaces* **2013**, *5*, 8686.

(53) Wang, X.; Zhang, D.; Braun, K.; Egelhaaf, H.-J.; Brabec, C. J.; Meixner, A. J. *Adv. Funct. Mater.* **2010**, *20*, 492.

(54) Gao, J.; Roehling, J. D.; Li, Y.; Guo, H.; Moule, A. J.; Grey, J. K. *Journal of Materials Chemistry C* **2013**, *1*, 5638.

(55) Carach, C.; Riisness, I.; Gordon, M. J. *Appl. Phys. Lett.* **2012**, *101*, 083302.

(56) O'Nei, K. D.; Semenikhin, O. A. *J. Phys. Chem. C* **2007**, *111*, 14823.

(57) Jørgensen, M.; Norrman, K.; Krebs, F. C. *Sol. Energy Mater. Sol. Cells* **2008**, *92*, 686.

(58) Hintz, H.; Egelhaaf, H. J.; Lüer, L.; Hauch, J.; Peisert, H.; Chassé, T. *Chem. Mater.* **2011**, *23*, 145.

Chapter 7 Conclusions

The aims of this thesis were to utilize the SECCM technique to find correlations between electrochemical (as well as (photo)electrochemical) activity and structural properties of electrode surfaces at the sub-micron to nanoscale with a focus on systems related to energy storage and conversion. These aims have been realized and demonstrated for electrocatalytic processes on platinum surfaces as well as been demonstrated in (photo)electrochemical systems as a proof of concept. Importantly, the SECCM technique can be adapted to a variety of systems (including photo-electrochemical measurements) and the work herein contributes to the efforts in improving energy storage and conversion research.

7.1 Electrocatalysis at metal electrodes

The SECCM studies presented on polycrystalline platinum foil (Chapters 3 and 4) highlight that subtle variations in localized electrode structure may lead to misinterpretation of kinetic data, especially if the measurements are performed using conventional electrochemical measurements at polycrystalline metal UMEs which may include only a small number of grains and grain boundaries.

In Chapter 3, it is shown that there are significant variations in electron transfer (of the $Fe^{2+/3+}$ redox couple) on polycrystalline platinum using SECCM and that these variations are strongly correlated to the local crystallographic orientation. The findings were compared with single-crystal measurements and found to be consistent, demonstrating the capability of performing pseudo-single crystal experiments. In addition, the SECCM based approach was shown to be capable of

probing facets with high crystallographic indices and boundaries between crystal grains, something which is very challenging to study on single-crystals.

In Chapter 4, these capabilities have been extended to systems employing RTILs, highlighting further advantages over classical methods which are limited due to the high viscosity (and slow diffusion of the redox species). The major counter electrode reaction of DSSCs, was analysed and rationalized, showing the process (I^-/I_3^- on Pt) to be strongly sensitive to surface structure. Importantly, subtle electrode structure effects were readily picked up by SECCM and shown to contribute to an increase of up to two folds in apparent kinetics. Thus, SECCM was also shown to allow spatial measurements of electrocatalytic processes in RTILs, which are of considerable (and growing) interest for many important applications in energy technologies, electrosynthesis and sensing.

7.2 Photoelectrochemical systems

The platform can also be utilized to study (photo)electrochemical systems at the micro to nanoscale with high sensitivity (as shown in Chapters 5 and 6). High resolution electrochemical imaging techniques are extremely powerful for identifying (electro)catalytic sites and optimal (electro)catalysts, but – hitherto - such methods have proved very difficult to implement in photo-electrochemical systems due to the inherently low currents that prevail. In Chapter 5, an approach for addressing these limitations in (photo)electrocatalysis, by coupling high resolution electrochemical scanning droplet cell measurements with photo-illumination was presented. The approach was exemplified by investigating the photoanode of a

DSSC and high resolution spatial images of the photo-sensitive areas were readily produced. Thus, SECCM is also demonstrated as an effective tool for local surface modification and in-situ (photo)characterization.

The demonstrated high spatial resolution is achieved with SECCM (photo)electrochemical imaging coupled with ultrasensitive measurements at the tens of fA range, and thus opening up prospects for accessing a wide range of (photo)electrochemical phenomena. This may include future applications, such as assessing materials for solar energy conversion, water treatment, bio-sensing and photosynthesis. The ability to perform ac photocurrent techniques such as IMPS methods were only briefly demonstrated and could be implemented at the nanoscale, in the future, pushing the technique further.

Furthermore, in Chapter 6, a correlation of film morphology and photo-activity for the reduction of dissolved oxygen in an organic photoelectrochemical cell configuration was obtained for electrodeposited P3HT films on a transparent gold electrode using the multimicroscopy photo-SECCM platform. For the illustrative case of P3HT, ordered thin films (identified by Raman peak centers and FWHM of the $C_{\alpha}=C_{\beta}$ Raman band at 1446 cm^{-1}) exhibited the highest photo-activity. However, ex-situ measurements highlighted that subtle variations in film thickness and morphology contribute to a significant change in photo-activity of the films, especially after some aging. The platform opens access to the screening of electrodeposited thin films prepared in-situ, combined with sensitive localized (photo)-activity measurements, as highlighted by the ex-situ photo-SECCM experiment where it was possible to map variations in activity across, (within) a deposit. Finally, it has been illustrated that the platform is able to extract valuable

information on growth and degradation processes for which improved knowledge is needed in the search for optimized materials.

7.3 Future prospects

Future prospects and identified limitations in SECCM for studying energy materials is discussed below, partitioned to two parts: (i) non-photoelectrochemical systems and (ii) (photo)electrochemical systems.

Starting with the study of materials for electrocatalytic systems, a wealth of electrocatalytic materials related to energy and storage can be studied for optimization in the future at the submicron and nanoscale. With SECCM probes going down to dimensions below 100 nm,[1] spatially resolved imaging of features with similar dimensions is now feasible, including the possibility to fine-resolve grain boundaries in metal surfaces. This ultimately opens up the possibility to investigate catalyst materials with nanometer size features which were too small to resolve when the work herein was carried. Electrode materials incorporating nanoscale features such as metal nanoparticles (Pt, Au) and metal oxides such as TiO_2, ZnO and hematite can be investigated and screened for activity. Further downscaling of SECCM probes can be achieved and may allow access to a wider range of materials with only several nanometer features. Downscaling of the current sensitivity to the sub fA range will have to proceed with the downscaling of probe size in order not to be the limiting factor. Moreover, SECCM can now produce video images[2] (produced from localized CV measurements) as well as real-time fast scan imaging,[3] pushing even further the range of information that can be accessed which can lead to future exploration of kinetical data extraction from nano feature

materials. Thus, with the increase in spatial resolution of SECCM (by decreasing probe size and increasing current sensitivity) and allowing higher time resolution, time resolved electrochemical imaging of processes such as oxygen reduction will be able to be accessed at the nanoscale.

The use of RTILs as electrolytes in SECCM opens up the possibility to investigate systems relevant to Li-ion batteries technologies. In such systems residual amounts of: oxygen, water and air may dramatically affect the reaction mechanism and thus, environmental control becomes of paramount importance. In the future, better environmental control may be achieved by incorporating the SECCM in a glove-box setup, allowing oxygen and air sensitive systems to be investigated.

For (photo)electrochemical systems this thesis provides advancements in spatial resolution and photocurrent sensitivity. This has been demonstrated with benchmark systems, providing a proof of concept. Localized IMPS studies are still to be explored and may prove particularly insightful. Systems in interest to photoelectrochemical conversion may be studied in the future including metal oxide surfaces.

However, limitations in spatial resolution in photo-SECCM measurements are currently attributed to: (i) the low currents required to be measured at the nanoscale and (ii) the wetting behavior of the SECCM meniscus at the interface of metal oxides as well as porous materials, which are interesting materials commonly used as photoelectrodes (e.g. systems such as nanoporous ZnO, WO_3 and Fe_2O_3 surfaces have been experimented with, but exhibited excessive wetting).

As mentioned above, advancement in both noise reduction and increased sensitivity is important in order to access low current measurements. Only several fA are expected to be measured using SECCM probes of a few 100s nm in diameter for photoelectrochemical responses of systems in the range of 1 $mA \cdot cm^{-2}$. As for the wetting of the SECCM meniscus on oxide surfaces and porous materials, such limitations may be proven impossible to overcome, however, some leverage is achieved by the choice of solvent (RTILs and viscous solvents) to control the spreading of the SECCM meniscus on the surface investigated. In addition, hopping mode can be utilized where the contact time with the surface can be limited to minimize the initial spreading of the meniscus on the surface. Alternatively, measurements of nanoparticle collisions,[4] if the current sensitivity allows, may circumvent the need for spatial imaging.

Lastly, as shown for the coupling of photo-illumination, in the future, SECCM can be coupled to other in-situ techniques such as Raman microscopy and fluorescence microscopy. The combination of such techniques to the nanoscale electrochemical imaging technique may bring additional insight to the study of complex systems.

7.4 References

(1) Güell, A. G.; Cuharuc, A. S.; Kim, Y.-R.; Zhang, G.; Tan, S.-y.; Ebejer, N.; Unwin, P. R. *ACS Nano* **2015**, *9*, 3558.

(2) Chen, C.-H.; Jacobse, L.; McKelvey, K.; Lai, S. C. S.; Koper, M. T. M.; Unwin, P. R. *Anal. Chem.* **2015**, *87*, 5782.

(3) Momotenko, D.; Byers, J. C.; McKelvey, K.; Kang, M.; Unwin, P. R. *ACS Nano* **2015**.

(4) Kleijn, S. E. F.; Lai, S. C. S.; Miller, T. S.; Yanson, A. I.; Koper, M. T. M.; Unwin, P. R. *J. Am. Chem. Soc.* **2012**, *134*, 18558.